

AFRL-AFOSR-UK-TR-2010-0006



Multifunctional Ceramic Nanostructured Coatings

**Anatolij Tarasovich Pugachov
National Technical University 'Kharkov Polytechnical Institute'
Metals and Semiconductors
Frunze Str 21
Kharkiv, Ukraine 61002**

EOARD STCU 068013

December 2010

Final Report for 12 June 2007 to 12 June 2010

Distribution Statement A: Approved for public release distribution is unlimited.

**Air Force Research Laboratory
Air Force Office of Scientific Research
European Office of Aerospace Research and Development
Unit 4515 Box 14, APO AE 09421**

REPORT DOCUMENTATION PAGE				Form Approved OMB No. 0704-0188	
Public reporting burden for this collection of information is estimated to average 1 hour per response, including the time for reviewing instructions, searching existing data sources, gathering and maintaining the data needed, and completing and reviewing the collection of information. Send comments regarding this burden estimate or any other aspect of this collection of information, including suggestions for reducing the burden, to Department of Defense, Washington Headquarters Services, Directorate for Information Operations and Reports (0704-0188), 1215 Jefferson Davis Highway, Suite 1204, Arlington, VA 22202-4302. Respondents should be aware that notwithstanding any other provision of law, no person shall be subject to any penalty for failing to comply with a collection of information if it does not display a currently valid OMB control number. PLEASE DO NOT RETURN YOUR FORM TO THE ABOVE ADDRESS.					
1. REPORT DATE (DD-MM-YYYY) 15-12-2010		2. REPORT TYPE Final Report		3. DATES COVERED (From – To) 12-Jun-07 - 12-Jun-10	
4. TITLE AND SUBTITLE Multifunctional Ceramic Nanostructured Coatings			5a. CONTRACT NUMBER STCU Registration No: P-253		
			5b. GRANT NUMBER		
			5c. PROGRAM ELEMENT NUMBER		
6. AUTHOR(S) Dr. Anatolij Tarasovich Pugachov			5d. PROJECT NUMBER		
			5d. TASK NUMBER		
			5e. WORK UNIT NUMBER		
7. PERFORMING ORGANIZATION NAME(S) AND ADDRESS(ES) National Technical University 'Kharkov Polytechnical Institute' Frunze Str 21 Kharkiv 61002 Ukraine				8. PERFORMING ORGANIZATION REPORT NUMBER STCU 06-8013	
9. SPONSORING/MONITORING AGENCY NAME(S) AND ADDRESS(ES) EOARD Unit 4515 BOX 14 APO AE 09421				10. SPONSOR/MONITOR'S ACRONYM(S)	
				11. SPONSOR/MONITOR'S REPORT NUMBER(S) AFRL-AFOSR-UK-TR-2010-0006	
12. DISTRIBUTION/AVAILABILITY STATEMENT Approved for public release; distribution is unlimited.					
13. SUPPLEMENTARY NOTES					
14. ABSTRACT This report results from a contract tasking National Technical University 'Kharkov Polytechnical Institute' as follows: The project is devoted to creating the new class of high-efficiency wear-resistant ion-plasma coatings based on transition metal borides for application under extreme conditions. The main idea of the project: providing the necessary properties of the materials due to controlling the phase composition, structure and stress state during their formation from ion-plasma fluxes.					
15. SUBJECT TERMS EOARD, Materials, Materials					
16. SECURITY CLASSIFICATION OF:			17. LIMITATION OF ABSTRACT UL	18. NUMBER OF PAGES 67	19a. NAME OF RESPONSIBLE PERSON Stephanie Masoni, Maj, USAF
a. REPORT UNCLAS	b. ABSTRACT UNCLAS	c. THIS PAGE UNCLAS			19b. TELEPHONE NUMBER (Include area code) +44 (0)1895 616420

Multifunctional ceramic nanostructured coatings

project 068013

STCU number P253
Final report

Contents

	Page
Summary	4
Introduction	4
1. Test Subject and Methods of Research	5
1.1 The Methods of Preparing Samples	5
1.1.1 Methods, Used for Fabricating the Targets to Produce the Ion-Plasma Coatings by Sputtering	5
1.1.1.1 W-Ti-B Quasi-Binary Target Fabrication and Certification	5
1.1.1.2 W-Ti-C Quasi-Binary Target Fabrication and Certification	6
1.1.1.3 Preparing Films and Coatings of Ti-B System	7
1.1.1.4 Preparing Films and Coatings of W-B System	7
1.1.1.5 Preparing Films and Coatings of TiB ₂ – WB ₂ Quasi-Binary System	8
1.1.1.6 Preparing Films and Coatings of W-C System	8
1.1.1.7 Producing Films and Coatings of Quasi-Binary TiC – WC System	9
1.2 Studying the Structure and Elemental Composition Condensates	9
1.3 Using the Updated “New Profile” Software Package to Analyze Structure and Substructure Characteristics of Nanocrystalline Condensed Materials	10
1.4 The Methods of Mechanical Tests	15
1.5 The Method of Nanoindentation	16
1.6 The Method of Simulating Tests	16
2. Results and Discussion	17
2.1 Results of Structure Research	17
2.1.1 Film Structure of the Ti-B System	17
2.1.1.1 The Electron –Microscopic Data	17
2.1.1.2 Data the Structure Research of Thick Films	18
2.1.2 Film Structure of the W-B System	20
2.1.2.1 The Electron –Microscopic Data	20
2.1.2.2 Structure of Coatings on a Basis of Tungsten Boride	20
2.1.3 Coating Structure of the Quasi-Binary TiB ₂ -WB ₂ System	22
2.1.3.1 Macrostrengthened Condition of Quasi-Binary Coatings of TiB ₂ -WB ₂ System	30
2.1.3.2 Fractal Studying of Surface	30
2.1.4 Phase Composition, Structure and Macrostrengthened Condition of Coatings Obtained Using the Method of Triode Sputtering of WC Target	32
2.1.5 Phase Composition, Structure and Macrostrengthened Condition of Quasi-Binary Coatings of TiC-WC System	34
2.1.6 Modeling of the Open Space Factors for the Simulating Tests	38
2.1.6.1 Impact Produced by the Open Space Factors on a Structure and Substructure of Quasi-Binary Coatings of TiC-WC System	40
2.1.6.2 Impact Produced by the Open Space Factors on a Structure and Substructure of Quasi-Binary Coatings of TiB ₂ – WB ₂ System	42
2.2 Stresses, Physical and Mechanical Properties of Films and Coatings that Was Determined Using Tests of Flexure Console and Tension	43
2.2.1 Determination of the Modulus of Elasticity Using the Dependence of Flexure Console	43
2.2.2 Defining the Condensates Strength While Studying Tension	48
2.2.2.1 Defining the WC Coatings Strength While Studying the Samples Tension	48
2.2.2.2 Defining the W-B Coatings Strength While Studying the Samples Tension	50
2.2.2.3 Defining the Systems W-Ti-B Coatings Strength While Studying the Samples Tension	51

2.2.3 Determination of the Modulus of Elasticity and Hardness Using the Method of Nanoindentation	52
2.2.3.1 Hardness and Modulus of Elasticity for W-B Coatings	52
2.2.3.2 Hardness and Modulus of Elasticity for Ti-B Coatings	54
2.2.3.3 Quasi-Binary TiB_2 - WB_2 System	56
2.2.4. Coatings Adhesion	57
2.2.5. Determining the Coefficient of Thermal Expansion of Boride Films	58
Conclusions	59
References	62
List of Symbols, Abbreviations, and Acronyms	65

Summary

This paper delves into integrated analysis of a structure, substructure, stressed state and some mechanical and physical properties of the films formed by the titanium and tungsten borides and carbides. The analysis was done using the X-ray and electron-optical methods. This information expands our knowledge of the mechanisms that are involved in the formation of condensates using the ion –plasma methods and it is needed for evolving a condensate formation theory using these methods to provide the physical fundamentals for numerous practical applications.

In addition, this paper analyzes stability of the structural state and mechanical properties of materials of a new class, i.e. ion-plasma coatings of quasi-binary systems subjected to the influence of factors peculiar for the open space.

Introduction

Making materials in an environment of highly unbalanced process, in particular, obtaining coatings in an ion plasmous flow environment was formed recently as a new line for creating materials with unique structural and high functional physical-&-mechanical properties.

The research done during the last ten years showed that the high functional and primarily mechanical properties can be expected from optimization of a method of ion-plasmous formation of single-phase [1-3] and multi-phase coatings [4-8].

Such a condition can be reached either by depositing multi-layer systems or by natural division of phases during their deposition. For the latter the coating compositions should be based on limited solubility materials. Such systems include carbides, nitrides, borides and silicides based on transition materials of the 4-th group usually with relatively simple crystalline lattice as well as the systems based on the transition metals of the 6-th group that form more complicated crystalline structures. The simplest systems for the materials of such a kind are the quasi-binary ones that are in essence triple compounds.

Both components and WC-TiC quasi-binary system-based solid solutions that are given consideration in this project refer to the structures with cubic crystalline lattice and isolated arrangement of interstitial atoms in the octahedral interstitial sites of metal sub-lattice. These structures have sufficient physical-&-mechanical properties and thermal stability [9]. High melting temperatures, modulus of elasticity and carbide hardness of transition metals account for their application as protective heat-resistant coatings. Solid alloys based on tungsten carbides and titanium possess the required properties (oxidation resistance, heat conductivity and strength), thus providing the material stability at high temperatures, thermal shocks and in aggressive media environment [10]. If we approach this problem from the standpoint of electronic structure then we can see that among the lower borides whose interstitial atoms occupy the isolated positions in the interstitial sites of metal lattice are the borides that are formed by electron acceptor metals. Accordingly the electron transfer in such borides is directed to the metal and the metal components play the main role in the electronic structure of compounds.

High functional characteristics of initial components, a structure based on the relatively simple cubic lattice make the vacuum WC-TiC system –based coatings rather promising for application and research. A simple crystalline structure peculiar both for individual components of this system and solid condensed –state solution [10-12] allows for description of the processes revealed by structural analysis.

In borides of MeB_2 composition and higher the electron transfer is directed from metal atoms to the boron sub-lattice [13] leading to the formation of complicated structural clusters (chains, meshes, skeletons). The structural elements complicated by boron atoms lead to the increase in crystalline lattice rigidity, hardness, melting temperature and oxidation resistance in $\text{Me}_2\text{B} \rightarrow \text{MeB} \rightarrow \text{MeB}_2$ line [13]. Boron p-state plays the main role in the electronic structure of higher borides. Due to this fact the higher borides that are formed by electron donor metals, in

particular TiB_2 that maximally meets this criterion, are more stable. For example, in contrast to the transient metal carbides the distance between boron atoms in diborides approaches the covalent B-B distance equal to 0,178 nm [14] and therefore in addition to “metal- to-nonmetal” and “metal-to-metal” bonds that define structural state in mono-carbide, the bond between nonmetal atoms plays a very significant role in a diboride; it generates more complicated structural formations in comparison with carbides.

Among the quasi-binary ceramic systems that have been well studied nowadays [15-22] in a massive macrocrystalline state the $\text{TiB}_2\text{-W}_2\text{B}_5$ system showed the greatest increase in strength combined with high hardness in comparison with separately taken system components. The bending strength in a massive state of ≈ 1000 MPa was reached for this quasi-binary system at hardness of 28 GPa and density of $5,88 \cdot 10^3 \text{ kg/m}^3$. The bending strength and hardness of individual components does not exceed 400 MPa and 26...27 MPa [15], accordingly. The ductility index made up a rather low value of $H/E \leq 0,06$.

It should be noted that the tungsten boride like the tungsten carbide has a high Young modulus value. However, in comparison with the carbide the tungsten boride has a higher hardness value. Therefore, the tungsten boride and tungsten boride-based composites can provide high wear-resistance. On the contrary, the decrease in the Young modulus can be expected for the nanostructured films and it is of interest to reveal the influence produced by the Young modulus value on the mechanical and service properties of the boride-based materials.

In this connection we assumed while doing this work that both the quasi-binary WC-TiC system and the $\text{WB}_2\text{-TiB}_2$ system can serve as a foundation for generation of condensed materials on their basis whose high hardness will match the high H/E ratio peculiar for the nanostructured condensed state.

1. Test Subject and Methods of Research

1.1 The Methods of Preparing Samples

1.1.1 Methods, Used for Fabricating the Targets to Produce the Ion-Plasma Coatings by Sputtering

1.1.1.1 W-Ti-B Quasi-Binary Target Fabrication and Certification

The targets using for sputtering (a diameter of 50 mm and thickness $t = 4$ mm) were prepared by hot pressing. The X-ray spectra of the single-phase TiB_2 and W_2B_5 targets show the peaks for phases that correspond to the balanced state: TiB_2 with the crystal lattice (a space group of $P6_3/mmm$, a hexagonal lattice with the lattice spacing ratio of $c/a \approx 1,07$ [13] and W_2B_5 (see Fig.1) with the crystal lattice (a W_2B_5 structure type and a $D_{6h}^{4-}P6_3/mmc$ space group [14]).

While producing the targets of quasi-binary system we used the modes of hot pressing that provide formation of the equilibrium two-phase ($\text{TiB}_2 + \text{W}_2\text{B}_5$) state [15]. The obtained X-ray spectra for two –phase targets show the peaks peculiar for the equilibrium state of two mixed phases, in particular, TiB_2 and W_2B_5 .

Fig.2 shows the typical X-ray diffraction spectra obtained for targets of quasi-binary composition system: 46 mol. % W_2B_5 and 52 mol. % TiB_2 .

In order to obtain the coatings using the method of d.c. magnetron sputtering in Ar environment we sputtered the targets of W_2B_5 and TiB_2 compositions and the targets of quasi-binary $\text{W}_2\text{B}_5\text{-TiB}_2$ system with a TiB_2 component content of 5, 10, 15, 20, 25, 50, 75, 80,90 mole %.

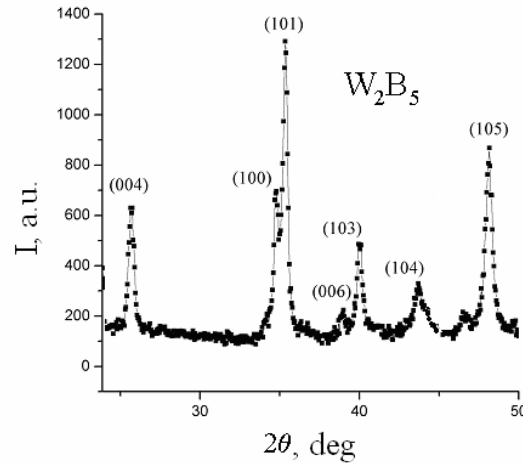


Fig. 1. A X-ray diffraction spectra of a target W_2B_5 obtained by hot pressing

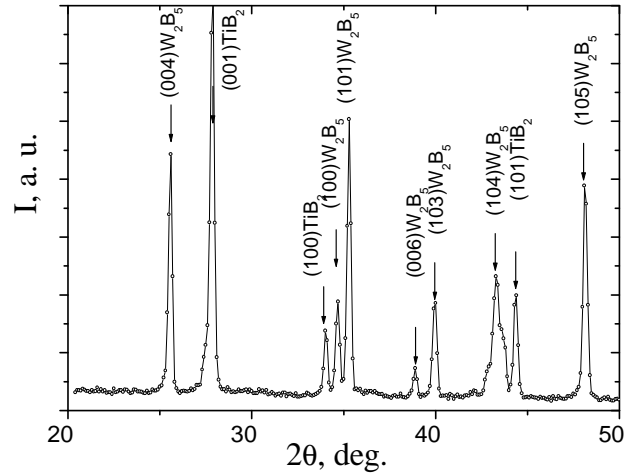


Fig. 2. A diffraction pattern for a target of quasi-binary system 46 mol.% W_2B_5 – 52 mol.% TiB_2 (Cu- K_α radiation)

1.1.1.2 W-Ti-C Quasi-Binary Target Fabrication and Certification

The targets intended for sputtering were fabricated using the method of hot pressing at a temperature of $T_{hp} \approx 1900$ K. A phase composition of the tungsten carbide target corresponded to the single-phase state of the equilibrium α -WC phase with the hexagonal lattice [10]. While obtaining the targets of quasi-binary composition the indicated temperature provided the quasi-equilibrium conditions for the formation of a two-phase stage with the well-controlled composition at the cooling rate of 100 K/min [23]. In this case we used the two-phase targets that contained the TiC- phases with the cubic lattice of a NaCl type and a α -WC phase with the simple hexagonal lattice. Fig.3. shows a peculiar target spectrum with average content of titanium carbide in amount of 31 mole %. In this work we used the targets with the following compositions: 85 mole% WC-15 mole% TiC, 79 mole % WC-21 mole% TiC, 69 mole % WC-31 mole% TiC, 25 mole % WC-75 mole% TiC, 10 mole % WC-90 mole% TiC, and those consisting only of TiC and WC.

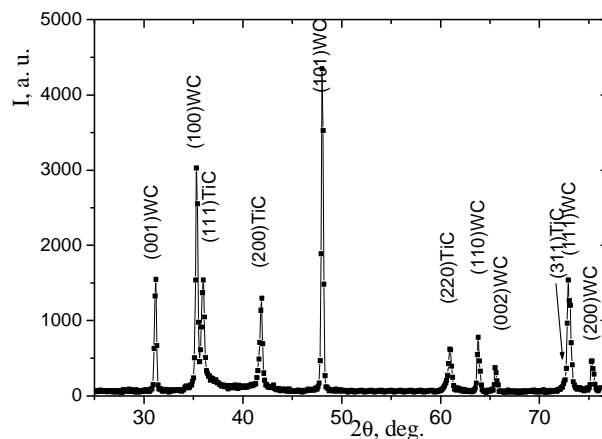


Fig. 3. A diffraction pattern for a target of composition 31 mol.% TiC – 69 mol.% WC

1.1.1.3. Preparing Films and Coatings of Ti-B System

The Ti-B films were obtained using the method of d.c. magnetron sputtering of a TiB_2 target ($\varnothing=50$ mm, 4 mm thick) in Ar atmosphere.

The TiB_2 targets were synthesized by subjecting TiB_2 powders to hot pressing at 2000 °C to obtain the boride films using the methods of magnetron and triode sputtering. As the target was used up during ion sputtering its phase composition was periodically controlled using the method of X-ray diffractometry. Prior to a film deposition the substrates were kept for one hour in vacuum at $3 \cdot 10^{-4}$ Pa and a temperature of 950 °C to remove contamination surface.

Thin films ($t < 1$ μm) that have the stainless steel and (00.1)-muscovite mica substrates were obtained using a magnetron sputtering. During deposition the substrate temperature was raised up to the room temperature of ~500 K. The substrate was heated up to $T_s \approx 500$ K just due to the operation of magnetron and release of condensation heat at a sputtered target substance deposition. The deposition rate was 0.17 nm/s at a magnetron power of 400 V x 100 mA ($W = 400$ V x 100 mA) and at a distance between a target and a substrate of 60 mm ($H = 60$ mm). The argon pressure (p_{Ar}) in chamber during target sputtering was 0.15 Pa.

The Ti-B films were deposited through magnetron sputtering of a TiB_2 target ($\varnothing=50$ mm, 4mm thick) onto silicon substrates that were heated to a temperature of 300 to 950 °C at a deposition rate of 0.3 nm/s. These films were 1μm thick.

Thin Ti-B films, ~30 nm thick were obtained by a method of triode sputtering of TiB_2 target in argon medium at $P = 3 \cdot 10^{-1}$ Pa. The films were deposited onto a thin (~10 μm) copper foil. Prior to evaporation of a substance the substrate was subjected to ion cleaning at a substrate potential of ~500 V. The target had a diameter of 80 mm and a substrate was placed at a distance of 55 mm from a target. A target potential was 1.5 kV, current density was 3 mA/cm² and substrate temperature was ~600 °C. The Ti-B films intended for electron-microscopic studies were prepared by dissolving copper in HNO_3 .

1.1.1.4 Preparing Films and Coatings of W-B System

At preparing coatings by vacuum **triode sputtering potential** on a W_2B_5 target varied, that defined energy of deposited and bombarding ions and atoms. Potential on a target U_s changed from 0.5 up to 3.5 kV. Thus the deposition rate changed also. The target had a diameter 110 mm, diameter of the screen was 80 mm. Before deposition of a coating the clearing of a target and substrate by vacuum ion bombardment will be carried out: a target up to a level of

potential on a target 1.2 Us, where Us – potential in a condition sputtering; potential of a substrate and a target was 400-500 V. After preparation will be carried out deposition of coatings at the following geometry: distance a target was substrate of 80 mm; the size of the holder of substrates 70x 70 mm². The substrate temperature T_s was raised up to 700-1000 K just due to the radiating influence at ion-plasma sputtering. As substrates the following materials by thickness ~ 100 µm were used: stainless steel, silicon, permalloy, copper et al.

The coatings was obtained at the following conditions sputtering: a current on a target was 200-250 mA; a potential on a target are specified in the table 1 together with the appropriate deposition rate; time deposition was 1-2 hours.

Table 1. Sputtering conditions of coatings: a potential on a target and appropriate deposition rate

Potential on a target, U _s , kV	0.5	0.7	1.5	2.3	2.5	2.7	3.0	3.5
Deposition rate, nm/s,	0.28	0.37	0.5	0.61	0.64	0.62	0.6	0.61
Deposition rate, µm/h	1	1.35	1.8	2.2	2.3	2.25	2.16	2.2

The coatings were obtained using the method magnetron sputtering of a W₂B₅ target (Ø=50 mm, a distance between a target and a substrate of 40 mm, sputtering potential was 300-400 V, current on a target was ~100 mA). The substrate temperature varied by thermal heating in the range of 600-1200 K. The deposition rate was about 2 µm/hours. As substrates the following materials by thickness ~ 100 µm were used:pyroceramics, silicon, permalloy, nickel.

The method of **magnetron sputtering** in Ar atmosphere of a W₂B₅ target in Ar atmosphere (target diameter was Ø=50 mm, thickness t=3.5 mm)were prepared films deposited onto permalloy, tungsten and silicon substrates. During deposition the substrate temperature T_s increased from a room temperature up to ~500 K. The substrates were heated only due to the magnetron work and release of the condensation heat while depositing the substance of a sputtered target. At magnetron power of W=420Vx100 mA and target –to- substrate distance of H=60 mm the deposition rate ω was 0.08 nm/s. The argon pressure (pAr) in the chamber during target sputtering was 0.15 Pa.

1.1.1.5 Preparing Films and Coatings of TiB₂ – WB₂ Quasi-Binary System

The ion-plasma coatings were deposited into substrates (monocrystalline silicon 340...420 µm thick, aluminium foil 15 µm thick, beryllium foil 35 µm thick, pyroceramics, tantalum, niobium) Thus the detailed structural researches were carried out for the coatings deposited on the silicon polished plates. The structural data got on other types of substrates were used for qualitative comparison. An application as substrates of thin foils from easy materials (aluminium, beryllium) allowed in one experiment to study a structure and substructural descriptions of coatings both athwart plane of substrate (survey “for reflection”), and in the plane of substrate (survey “for transparency”).

1.1.1.6 Preparing Films and Coatings of W-C System

In this case the coatings were obtained using the tungsten carbide target (Ø100 mm, 5 mm thick) prepared from the synthesized powder of tungsten carbide by hot pressing. The results of X-ray analysis showed that the target composition corresponded to WC α-hexagonal phase. The target screen had a diameter of 80 mm and the target-to-substrate distance was 80 mm. In order to supply a biasing potential to a substrate for ion bombardment at purging and sputtering the coatings it (the substrate) was isolated from the body.

The WC coatings were deposited onto substrates with preliminary prepared surface (cleaned, washed and attested). The polished silicon 350 µm thick, stainless steel X18H10T

400 μm thick and copper foil 70 μm thick were used as substrates. The triode deposition was performed under the following conditions: it was done in vacuum using argon as a working gas $\sim 10^{-1}\text{Pa}$, target current of $\sim 250\text{ mA}$; the voltage U_s during sputtering on a target varied within 0.5 to 3.5 kV; the deposition rate increased within 0.1 to 0.5 nm/s, accordingly.

1.1.1.7 Producing Films and Coatings of Quasi-Binary TiC – WC System

The coatings was prepared using the method of vacuum triode sputtering. Coatings prepared by ionic sputtering of targets. The planar magnetron diagram of ionic sputtering for sputtering of targets was used. Sputtering was carried out in the environment of the rare gas Ar at pressure 0,2...0,3 Pa. The supplied sputtering voltage of 320...400V provided the flux density for the deposited metal atoms of $J_{\text{Me}} \approx (2,3...2,7) \cdot 10^{15} \text{ cm}^{-2} \cdot \text{s}^{-1}$. The deposition temperature varied through a controlled heating of a table that was specially designed for the specimens. The thickness of coatings made 1,0...1,4 μm . As substrates the following materials were used: aluminium foil, beryllium, plates from a nickel and pyroceramics, polished monocrystalline silicon.

1.2 Studying the Structure and Elemental Composition Condensates

The X-ray diffraction analysis of samples was performed using the diffractometer DRON-2 in a filtered $\text{Fe-K}\alpha$ radiation and DRON-3 in a filtered $\text{Cu-K}\alpha$ radiation at registering X-ray in a discrete survey mode with scanning pitch varying within the interval of $\Delta(2\theta) = 0.01...0.05^\circ$ depending on the half-width and intensity of diffraction lines. The exposition time at one X-rayed point was 20...100 s. The electronic information transfer and control units (BUIP-2), (BUIP-3M) developed by NTU “KhPI” were used for pointwise registration. The diffraction profiles were separated in case of their superposition according to the “New_profile” program of separation of superimposed lines, which was developed by NTU “KhPI”. The volume fraction of phases in a film was calculated using the standard technique that takes into consideration the integral intensity and reflecting capacity of several lines in each phase [24].

The substructure characteristics (the coherent scattering region size (crystallites) and micro-deformation) were studied using the method of approximation. This information was obtained using the standard Hall plot construction technique at several orders of reflection from the planes [25].

The degree of structure perfection ($\Delta\psi$) was determined at full width at half maximum (FWHM) of a diffraction line taken at Ψ -scanning. The value $\Delta\psi$ describes the degree of disordering of crystallites. Thus texture samples can be separated into low- and strong textured with the conditional boundary value $\Delta\psi \approx 0,2 \text{ rad}$.

The macrostressed state in polycrystalline coatings was studied using the method of X-ray tensometry (“ $\sin^2 \Psi$ -method”) [24].

In the case of visible flexure in a film-substrate system and in the case of amorphous structure the mode of deformation was studied with reference to a coating-substrate flexure value using the Stoney correlation [26].

The structural studies of a thin film (thickness $t_f \approx 12... 30 \text{ nm}$) were carried out using the methods of transmission electron microscopy provided by electron EMV-100AK microscope at accelerating potential of 100 kV. The reflection high electron energy diffraction investigation was performed also using the electron diffraction device at accelerating voltage of 50 kV.

The elements concentration was determined using the secondary (fluorescent) emission spectra (X-ray fluorescent analysis-XFA). The radiation of X-ray tube of a shooting –through type with Ag anode was used as a primary excitation radiation at excitation voltage of 42 kV.

The film composition was studied using the method of X-ray photoelectron spectroscopy at XPS-800 Kratos spectrometer in vacuum of $p = 1.3 \cdot 10^{-6} \text{ Pa}$. Photoelectrons were excited by

MgK α radiation ($h\nu=1253,6$ eV) at X-ray tube power of 15 kV x 20 mA. The spectrometer resolution was 1 eV, the accuracy of determination of a bonding strength was 0.3 eV. A layer-to-layer etching was carried out using the ion gun (Ar $^+$, E = 2 keV). The thickness of analyzed layer was ~ 5 nm.

1.3 Using the Updated “New Profile” Software Package to Analyze Structure and Substructure Characteristics of Nanocrystalline Condensed Materials

Figure 4 gives the functional diagram for “New profile” software package. All the package functions can conditionally be subdivided into several groups, in particular, data input-output, preliminary processing, work on line shapes, structure and substructure analysis and auxiliary operation functions. Most computational procedures are of universal character and can be used for analysis of a different type. However, the main purpose of this software package is to process X-ray diffraction data.

Such stages as smoothing, background separating (the program envisages three different methods of background separation) and eliminating the doublet K α_2 – component (main option for Rechner method [24]) are mandatory for preliminary processing of the above data.

Experimental data smoothing is one of the most important operations used for preliminary processing of the results of X-ray diffraction studies, because the obtained experimental data can significantly differ from real dependence due to wanted signal suppression by noise of a different origin. If the experimental noise is caused by instrumental error, then in most cases its level can be reduced by taking purely technical measures. However in case of X-ray experiment the main reason for noise appearance can be a statistical nature of X-ray radiation. The registered pulse counting rate is subordinated to the Poisson statistics and the measurement error estimation can be obtained using formula [27]:

$$\sigma = \sqrt{N} \quad (1)$$

where σ is a measurement error and N is pulses counting rate.

For tenfold reduction of noise it is necessary to increase hundred-fold count of pulses taken at each spectrum point. Therefore the technical noise smoothing results in a very significant increase in time required for X-ray experiment. At the same time the analysis that uses the derivatives is only possible for relatively smooth spectra. Therefore preliminary processing is required to smooth or digitally filter the obtained experimental data.

The simplest method of digital filtering, which is realized in this program is called “moving average”. The noises are smoothed by plotting a curve the closest to all experimentally obtained points. Taking a line with odd number of points we can obtain a smoothed value for a line midpoint. It is the best one for the selected cluster of points and selected approximating function. A one-point shift allows for determination of smoothed value for the next point, etc. In the simplest case the linear approximation is used and the midpoint is calculated as arithmetic mean of ordinate of all cluster points. The smoothing done using the linear digital filter allows us to reduce noise by a value, which is approximately equal to a square root of number of the used points. The number of points should be such that any convolution interval includes only one bending point. However the linear filter distorts the wanted signal as well. In particular, the peak intensity is reduced. In addition to the linear digital filter the cubical polynomial smoothing also found realization in the “New _Profile” program.

The experimental data can be processed using the convolution conceptions. However the problem arises that requires finding such a method of convolution that would lead to the fluctuation smoothing and would cause no drop in maximum intensity. Therefore, in many cases it is reasonable to use nonlinear methods, for example, a median filtering (Fig.5).

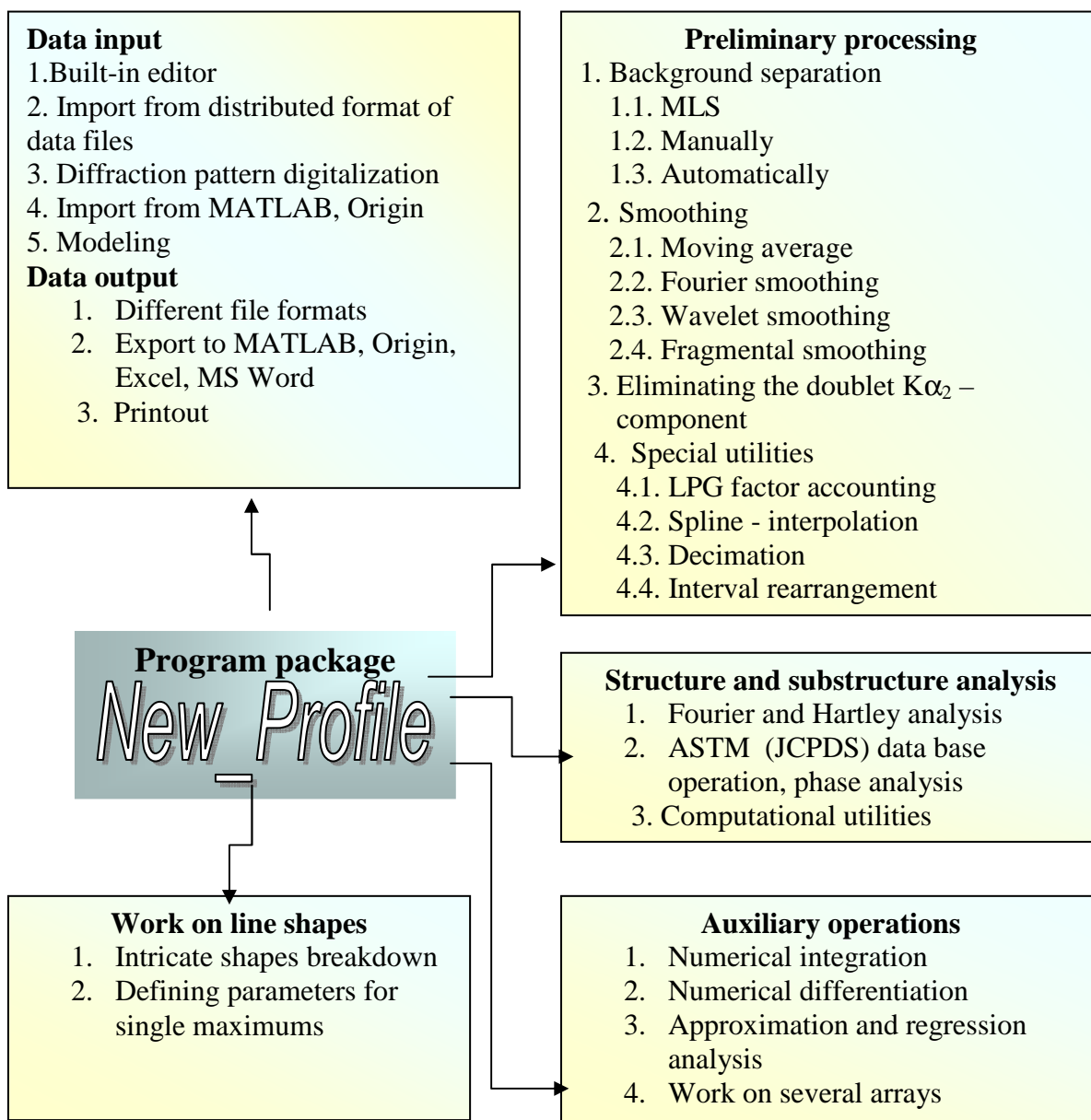


Fig. 4. Functional diagram for “New profile” software package

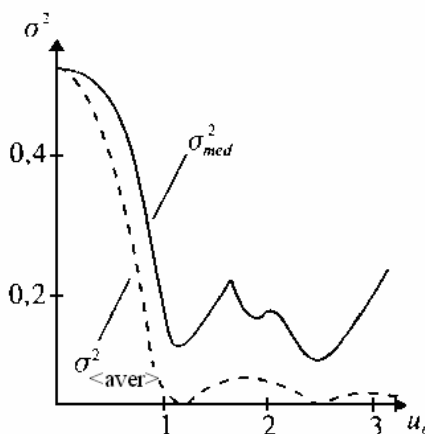


Fig. 5. Decreasing the noise dispersion at filtering using the method of moving average ($\sigma^2_{<aver>}$) and median filtering (σ^2_{med})

The important advantage of median filtering is that it allows for elimination of pulse noises actually without distortion of smoothly changing sequences of signal values whose duration exceeds the half of aperture length of median filter. The 1-D median filter represents the so-called “running window” of n -counts expansion, in which the central element is replaced by a median. The obtained data [28] show that in case of stationary random process the median filter with $N \geq 5$ has characteristics very similar to those obtained using the method of **“moving average”** (Fig.5). The drawback of this method is a “step” type profile distortion.

The most effective and universal method of smoothing is to represent the arbitrary function as a Fourier series. The Fourier series represent the trigonometric polynomials that were constructed on the basis of periodic basic function, i.e. sinusoid. Due to this fact the Fourier series are capable of approximating the periodic functions. The relationship [29]:

$$y(t) \sim \sum_{n=0}^N c_n \cdot e^{in} \quad (2)$$

serves as a basis for representation of periodic signal $y(t)$ by Fourier series

where i is an imaginary unit. A function of $y(t)$ is a sum of products of sinusoid represented by e^{in} term multiplied by Fourier coefficients C_n that are calculated as :

$$c_n = \frac{1}{2\pi} \int_0^{2\pi} y(t) e^{-in} dt \quad (3)$$

The drawbacks of representation of arbitrary signals and functions by Fourier transformation are as follows:

It cannot be used for analysis of nonstationary signals;

- The basic function at series expansion is a harmonic oscillation, which is mathematically defined along the entire time axis and has parameters invariable in time;
- Certain signal peculiarities cause insignificant changes in frequency image of a signal in the entire range of frequencies that spread along the frequency axis, which makes their spectrum-related detection actually impossible.

The problems of time-limited spectral analysis and signal synthesis are partially solved through transition to the short-term or window Fourier transformation. The idea of this transformation is as follows: the time interval of signal existence is broken into several gaps, i.e. time windows. Each gap does its own computation of Fourier transformation. If the frequency components of a certain signal were present in a certain window, then these will be present in spectrum as well. Thus, we can switch over to the frequency-temporal signal representation.

The short-term (window) transformation is done using expression:

$$A(\omega) = \int_{-\infty}^{\infty} y(t) \cdot \omega(t-b) \cdot e^{-i\omega t} dt \quad (4)$$

Here in contrast to the Fourier integral the $y(t)$ function under integral sign is additionally multiplied by window function $\omega(t-b)$. The window b -parameter prescribes its shift along the time axis. Thus for elementary rectangular window the function of $\omega(t-b)$ gives within the window 1 and outside the window it gives 0. Each window has its own set of complex amplitude of a signal in a frequency range.

Due to the fact that each window covers a small time interval the description accuracy of local changes in a signal can be improved. However, taking into consideration Heisenberg uncertainty principle we conclude that choosing a window with small temporal width we obtain high temporal resolution and low frequency resolution and visa versa taking a window with large

temporal width we obtain a good frequency resolution and a bad temporal resolution. Therefore the contradiction peculiar for this method cannot be resolved.

Wavelet transformation of signals used for smoothing by the “New_profile” software package is based on breaking the approximation into two components, in particular, an approximating component and specifying component with their further refinement. The wavelets can be represented as wave signals that were formed on the basis of a certain initial (basis) function capable of performing the Fourier transformation locally at the site of their location not along the entire temporal axis (or x-axis) [30]. The basis functions are assumed to be prescribed as certain functions and only C_k coefficients contain signal-related information. The coefficients for such Fourier –similar series for arbitrary signal $s(t)$ are calculated using the formula :

$$C_k = \frac{1}{2\pi} \int_0^{2\pi} s(t) e^{-itk} dt \quad (5)$$

The removal of noises is based on eliminating the signal spectrum high-frequency components. However, one more method is applicable for wavelets, in particular, restriction of specifying coefficients. The short-term signal peculiarities (for example, the noises in a form of a set of such peculiarities) create specifying coefficients with high content of noise components that have essential accidental release of signal values. By prescribing a certain threshold for their level and removing the level specifying coefficients it is quite possible to reduce the level of noises and thus to smooth the curve of spectral distribution.

The main step of preliminary processing of experimental X-ray diffraction patterns is a background separation operation. The “New_profile” program envisages three different modes of realization of this operation. The selection of the mode depends on the type of experimental data. The manual selection of parameters of linear bevel background can be used only for processing the profiles with “ragged tails”, i.e. for those lines, in which due to the incomplete information the background can be separated using the additional information obtained by processing similar arrays.

The linear background separation using the method of least squares (MLS) found wide application. This processing option indicates the intervals of points through which the program plots a straight line using the method of least squares. This straight line is the linear background that should be excluded from initial data to ensure the correct follow-up computations.

The third option of background cancellation provided by the “New_profile” program envisages fully automatic determination of parameters for linear or curvilinear background.

The “New_profile” program eliminates the doublet $K\alpha_2$ – component using several methods. A classic Reehinger method [24] is the basic method embedded into the program. The program realizes it using two methods, in particular, left - calculation method and right-calculation method. The second method is preferable if two long tails are available in the right portion of a profile and are unavailable in the left portion of a profile. However, due to the specificity of computations this option approaches the quality of initial data in a more critical way, especially from the standpoint of correct background separation and proper smoothing.

The value of mean residual function is used as a criterion of accurate parameters fitting and is computed using the formula:

a) Lorenz (Cauchy) function

$$I(x) = I_0 / (1 + kx^2), \quad (6)$$

where I_0 is an intensity in maximum; $k = 1/(\omega/2)^2$; ω - width at a half of height.

b) The updated Lorenz (Cauchy) function

$$I(x) = I_0 / (1 + kx^2)^2, \quad (7)$$

where $k = 0,4142/(\omega/2)^2$.

c) The intermediate Lorenz (Cauchy) function

$$I(x) = I_0 / (1 + kx^2)^{1.5}, \quad (8)$$

where $k = 0.5874 / (\omega/2)^2$.

d) Pirson function VII

$$I(x) = I_0 / (1 + kx^2)^m, \quad (9)$$

where $k = (2^{(1/m)} - 1) / (\omega/2)^2$; m is a coefficient of form.

e) The forked Pirson function VII

$$\begin{cases} I(x) = I_0 / (1 + k_1 x^2)^{m_1}, & x > 0 \\ I(x) = I_0 / (1 + k_2 x^2)^{m_2}, & x \leq 0 \end{cases}, \quad (10)$$

where $k_1 = (2^{(1/m_1)} - 1) / (\omega/2)^2$; $k_2 = (2^{(1/m_2)} - 1) / (\omega/2)^2$; m_1, m_2 are a coefficients of form.

f) Pirson function IV

$$I(x) = I_0 / (1 + kx^2)^m \cdot e^{-\eta \arctan kx^2}, \quad (11)$$

where $k = (2^{(1/m)} - 1) / (\omega/2)^2$; m is a coefficient of form.

g) Gauss function

$$I(x) = I_0 * \exp(-kx^2), \quad (12)$$

where $k = 0.6931 / (\omega/2)^2$.

The value of mean residual function is used as a criterion of accurate parameters fitting and is computed using the formula:

$$\bar{\epsilon} = \left(\sum_{j=1}^N [y_i - I(x_i)]^2 \right) / \sum_{j=1}^N [y_i]^2 * 100\%, \quad (13)$$

where y_i is an experimental array of intensity values; x_i is an angle array; N is a number of points of X-ray profile; $I(x_i)$ are the intensity values for x_i angles obtained through model calculation.

The “New_profile” program uses the method of full profile analysis to expand the intricate profiles in components, i.e. the model approximation is constructed, which is successively refined later on by adding new lines and correcting their parameters for the best coincidence with a real profile. The value of residual function is used as a criterion (13). For search of optimal parameter values the following minimization technique is used, in particular Hook –Jives method, Nelder- Mid method, Paul’s conjugate directions method, Davidon-Fletcher- Paul and Levenberg-Markwart methods [31-33]. To describe the shapes of model lines same functions are used as for description of separate peaks (6-12). Depending on the adjustment of optimization parameters the computation proceeds either until the value of minimal residual is found or until maximally possible number of iterations is done.

The expansion of intricate profile in components (quantity, intensity and position of lines) can serve as a basis for qualitative phase analysis. The electronic database of ASTN file is used for this purpose [34]. The ASTM database can be operated both in manual and semiautomatic modes. In case of manual operation the sampling from database is done in compliance with inquiry filters. The restrictions on card numbers and availability or unavailability of chemical elements can serve as the filters including more complicated restrictions on availability of card lines selected with prescribed accuracy. In the semiautomatic mode the restrictions related to the position of revealed lines can be generated automatically on the basis of the result of expansion of intricate profile in components. The obtained list of cards is browsed and it is compared with the revealed lines.

The substructure characteristics were studied using the well-known method of approximation of shape of the diffraction peak. This study requires the selection of approximation function that provides the minor discrepancy at comparison with the experimental

curve. The Cauchy function of $(1+\alpha x^2)^{-1}$ or Gauss function of $\exp(-\alpha x^2)$ that are generally used for the approximation are attributed to the ultimate cases and describe the real experimental profile with a relatively high discrepancy. To specify the most accurate approximation function the "New_profile" program envisages a comparative selection that includes a profile description by eight primary functions including the asymmetric ones (Fig.6). The latter are important if the profile asymmetry appears, for example, during formation of the growth defects in a packing.

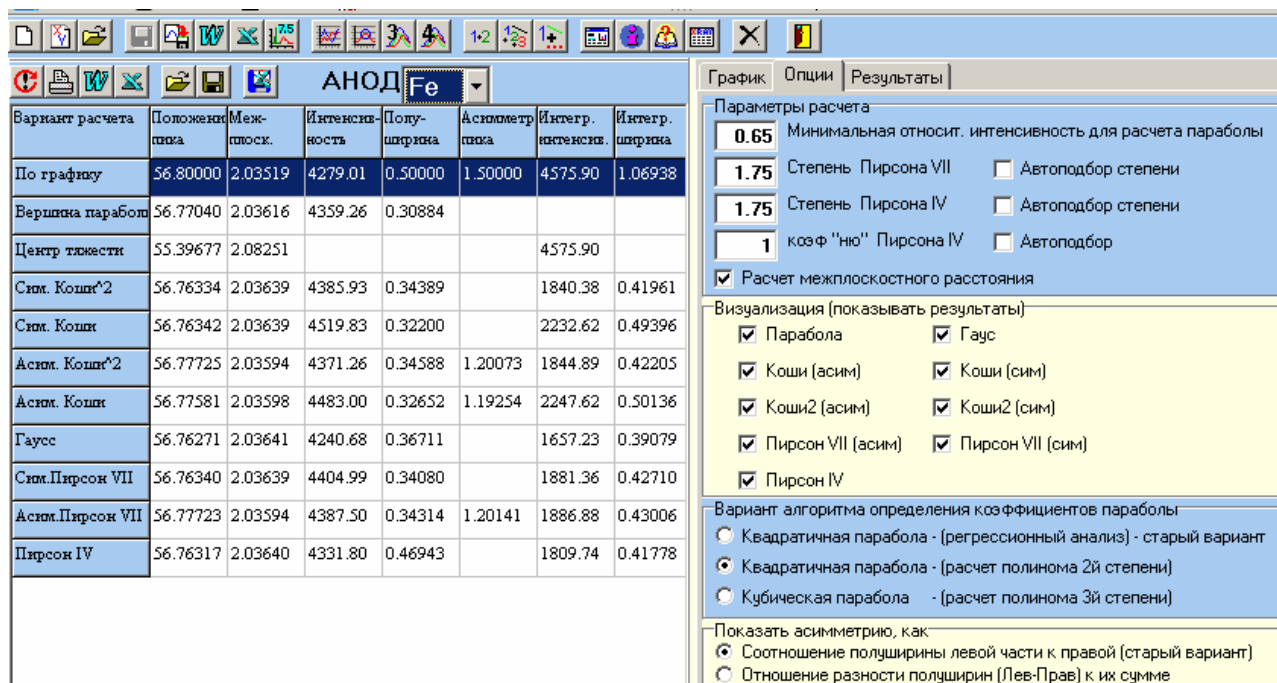


Fig.6. A window used for the choice of approximation function of diffraction lines

1.4 The Methods of Mechanical Tests

The permalloy and tungsten substrates were used to define the mechanical stress and Young modulus for the amorphous films using the method of cantilever bending, which was described in our 01-04 quarters 2008 report submitted previously. While depositing a film onto a console-fixed substrate the deviation of its free end was controlled in situ using a microscope KM-6 with accuracy of $\pm 5 \mu\text{m}$. To increase film adhesion the working surface of a film was treated by high-frequency plasma directly before starting the film condensation.

The stresses in films in the process of their deposition were determined from the bending value of substrates. The substrates were fastened as a cantilever. The thickness of substrates from mica made $t_f = 22 \mu\text{m}$ and $15 \mu\text{m}$ and for substrates from stainless steel $t_f = 53 \mu\text{m}$.

The mechanical tensile properties of the objects under research were determined in the mode of active loading under the room temperature. The tension machine with prescribed strain rate equipped with the device for automatic recording of load-elongation diagram was used to carry out the thin foil active loading tests.

The strip-like and figured samples with the test portion of $15 \text{ mm} \times 3 \text{ mm}$ were used for active tension tests. The samples were strained at a rate of $3,3 \cdot 10^{-4} \text{ s}^{-1}$. The tension diagrams were used to determine the yield point $\sigma_{0,2}$, which is the flow stress at residual strain of 0.2%; the strength limit σ_t , i.e. it is a stress at which the sample is destroyed and deformation prior to a sample collapse δ .

The microscopes MIM-7 (with magnification of 500) and BIOLAM-M (with magnification of 100) were used for examining the condensate surface fractographies.

1.5 The Method of Nanoindentation

Mechanical characteristics of the coatings (hardness and modulus of elasticity) were determined using the method of nanoindentation by nanoindenter. Coatings (thickness $t=1,2\dots1,4\text{ }\mu\text{m}$) obtained by sputtering of targets with different compositions and at different deposition temperatures into silicon substrates were investigated. The «Nanoindenter II, MTS System» and G200 were used for examining the mechanical properties. The load was equal 10 mH. The depth of informing layer made 100...130 nm. On the one hand it exceeds the value of a surface layer enriched by the foreign atoms by more than one order and on the other hand it is equal to a value, which is less than 0.1 of a film thickness, when the influence of a substrate can be neglected [35].

1.6 The Method of Simulating Tests

Simultaneous impact of space factors on studied films was produced using the integrated simulator [36], whose diagram is shown in Fig.7.

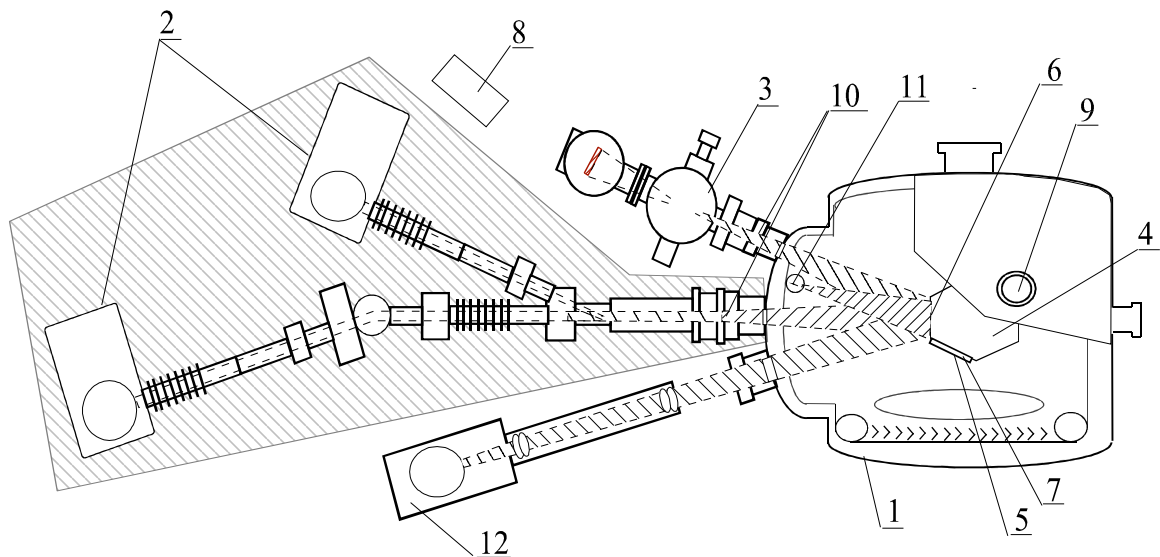


Fig. 7. Diagram. of integrated simulator of space factors

1- vacuum cryogenic chamber; 2- proton-&-electron injector; 3- VUV –radiation source; 4- multiway rotating sample holder; 5-a sample; 6 –zone of impact produced by radiation factors on a sample; 7- sample fixing plane, 8- simulation system control console; 9- vacuum electrical connection; 10 –vacuum slide gates; 12-Sun radiation source

A simulator structure envisages the possibility for studying both the influence of individual space factors and their joint action, at least of the main factors. The given specimens were tested under the joint action conditions, in particular:

- solar irradiation by a xenon lamp of 5 kW in a spectrum range of 0.2. to 0.4 μm at a beam diameter in a reference plane of 100 mm, an irradiance of up to 1600 W/m^2 and a distance from a vertex of a calibrated mirror to a reference plane of 800 to 1000 mm. A collimation angle did not exceed $\pm 2^\circ$ and the irradiance nonuniformity was equal to $\pm 5\%$.
- irradiation with protons and electrons of the combined beams to simulate the action of protons and electrons of the radiation bands of the Earth. The accelerator of protons and electrons had an operating range of energies of 50 to 200 keV at a value of the summed current of 0.01 to 20 μA and current density of $5.2 \cdot 10^8 - 1,0 \cdot 10^{12}\text{ part./cm}^2 \cdot \text{s}$. The studied samples were irradiated at the particle energy of 100 keV.

The principal of action of the used proton accelerator is that the ionization of the neutral H_2 hydrogen occurs due to the use of the high-frequency power-supply source and certain portion of this hydrogen is ionized into H^+_1 , H^+_2 , H^+_3 ions. Using the extraction electrode we extracted the charged particles from the ionization region; these particles pass through the focusing system and make their way to the magnetic field of a mass-analyzer with the rotation angle of 60° . By selecting the appropriate intensities of a magnetic field it is possible to extract ions of a required mass and to direct them into the acceleration tube, in which the energy of ions can be brought up to 200 keV because of the high (up to 200 keV) voltage.

A beam of protons and electrons irradiated the area of 100 cm^2 at a total current of protons and electrons of 5 to $20\text{ }\mu\text{A}$.

The working volume of a vacuum test chamber was evacuated by turbomolecular pump equipped with the nitrogen traps and screens.

The exposition time varied in the range of 3,5 to 14,5 hours, which correspond to the irradiation doses of $(1,6-6,5)\times 10^{17}\text{ cm}^{-2}$. The specimens were irradiated using different schemes: discretely, from a minimum dose to a maximum dose while screening some of them; other variations were also used.

2. Results and Discussion

2.1 Results of Structure Research

2.1.1 Film Structure of the Ti-B System

2.1.1.1 The Electron –Microscopic Data

Thin Ti-B films, 30 nm thick that have the copper substrate were obtained using the method the method of triode sputtering of a TiB_2 target (potential on a target was 1,5 kV, current density was 3 mA/cm^2 , substrate temperature was 600°C). These films have crystal structure which is shown by micro-diffraction pattern as well as by bright field and dark field [the reflex (111)] electron-microscopic images (Fig.8). The average size of crystals measured on the dark field electron-microscopic image is $\sim 12\text{ nm}$. A slope of Ti-B film under electron beam indicates the absence of a texture in the film. A comparison of d_{exp} with interplanar spacing of known borides shows that d_{exp} coincides with interplanar TiB spacing of cubic modification with $a = 0,424\text{ nm}$ period. Hence, TiB film composition differs from that of a sputtered TiB_2 target. A noticeable contribution made due to the sputtering of a growing film by the titanium and boron ions in deposition can be one of the possible reasons for decrease of boron concentration in a film.

A structure of Ti-B films that were obtained at low deposition temperatures (down to 500 K) is mainly characterized by amorphous base with volume - distributed ($\sim 10\text{ nm}$) inclusions of a small size. The faceting of those inclusions, which is observed at the electron microscopic images, proves their crystalline structure. Fig. 9 shows the typical structure of such films.

The low intensity of diffraction lines and their broadening prevent us from judgments with regard to the phase composition of a film. Nevertheless, three of four diffraction maximums (d_2 , d_3 , d_4) satisfactorily coincide with interplanar spacing $d_2 \rightarrow d_{(100)} = 0.262\text{ nm}$, $d_3 \rightarrow d_{(101)} = 0.203\text{ nm}$, $d_4 \rightarrow d_{(110)} = 0.152\text{ nm}$, that are peculiar for a TiB_2 [37] phase and d_1 may belong to the most intensive elementary boron $d_{(101)} = 0.407\text{ nm}$ line [38]. An assumption of presence of an elementary boron is not at variance with the results of film studies carried out using the method of X-ray photoelectron spectroscopy, because of high possibility. In this connection it is possible to assume that the inclusions observed at the electron microscopic images belong to the elementary boron microcrystals. The electron-diffraction patterns obtained for reflections from thicker films ($t_f \approx 600\text{ nm}$) testify that with the increase in thickness of coatings the width of diffraction peaks is not reduced and semiring intensity redistribution is not observed. It should be

noted that during the growth the texture is formed in the films with crystalline TiB_2 structure that is realized at higher temperatures.

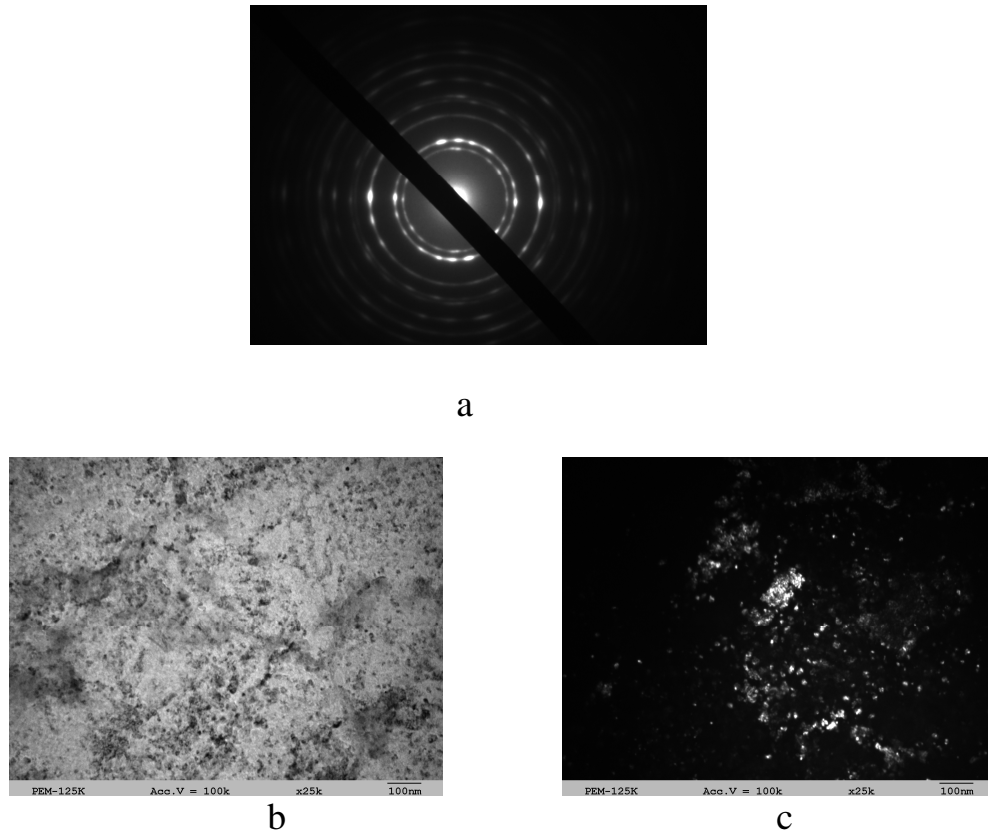


Fig. 8. An electron diffraction pattern (a), a bright-field image (b) and a dark-field (c) image by using (111) ring taken from a Ti-B film 30 nm thick

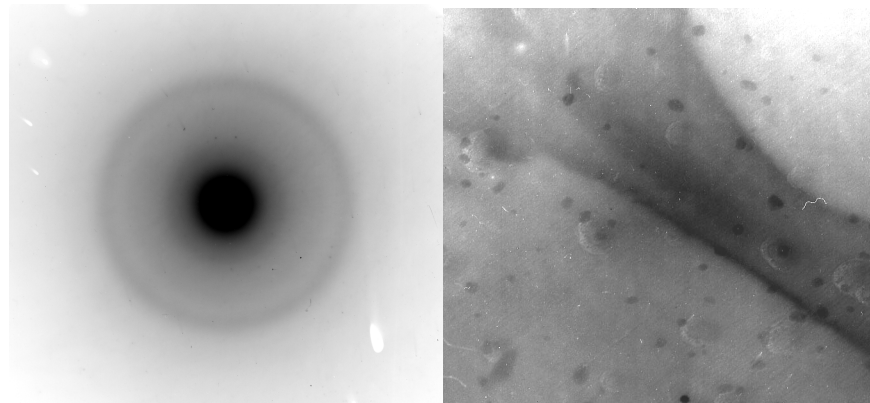


Fig.9. The electron diffraction pattern and electron microscopic image of a film structure obtained at TiB_2 target sputtering. The film is 30 nm thick

2.1.1.2 Data the Structure Research of Thick Films

Fig.10 shows that the condensates, $t \geq 1\mu\text{m}$ thick obtained through ion sputtering of single phase TiB_2 target in argon atmosphere and deposited onto silicon substrates at a temperature of 1170 K had noticeably smaller number of diffraction lines than the sputtered target diffraction patterns. The sputtered target diffraction patterns taken in $Fe-K_\alpha$ radiation (Fig.10) showed the

presence of reflections that are peculiar for TiB_2 hexagonal lattice (spatial group of $P6/\text{mmm}$, hexagonal lattice spacing relationship is $c/a \approx 1.07$ [14, 37].

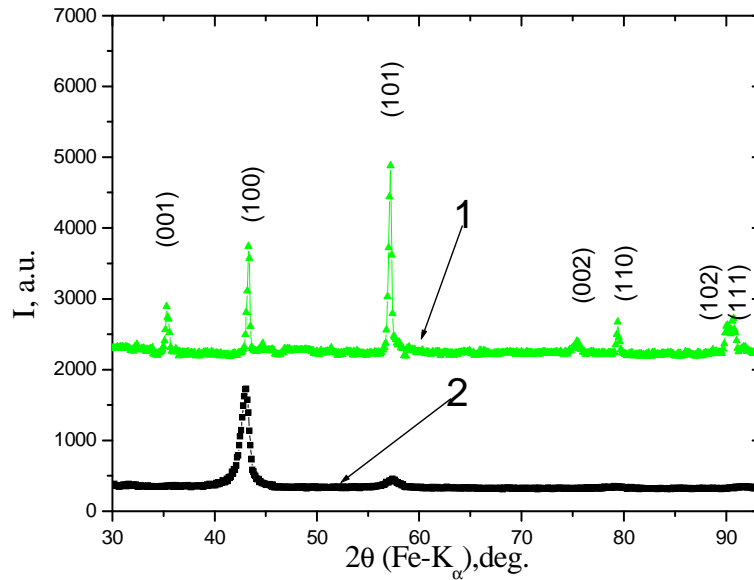


Fig.10. A diffraction pattern of a sputtered target (1) and condensate obtained at deposition temperature of 1170 K (2), (Fe-K_α radiation)

The obtained results show that the crystallites formed in condensates with a plane (10.0) parallel to the surface of growth have certain orientation. The relationship of intensity of revealed lines changes towards increase in intensity of lines from a system of planes (10.0). Thus, the relationship of the integral intensities of the lines (10.0) and (10.1) differs from the tabulated value of 0.55 for the random-orientation powder by 12.3 in a condensate obtained at $T=1170$ K. The decrease of substrate temperature down to 770 K resulted in decrease of degree of texturing down to 1.8 (Fig.11) and decrease at the of temperature down to 570 K the intensities relationship is approaching a tabulated value and is equal to 0.9.

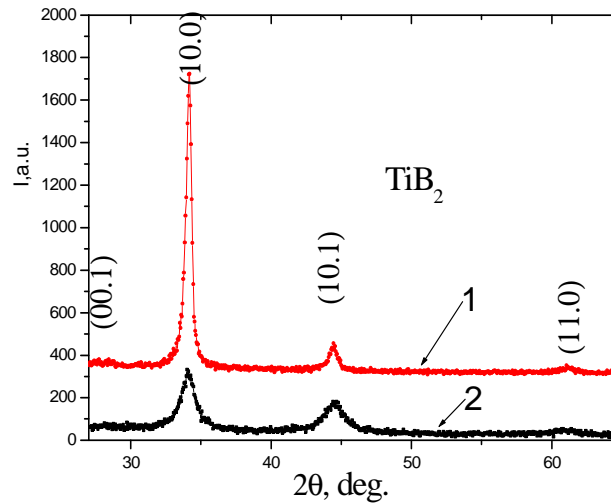


Fig.11. The diffraction patterns for a condensate obtained at onto-substrate deposition temperatures of 1170 (1) K and 770 K (2), (Cu-K_α radiation)

The diffraction patterns show that the width of diffraction lines increases with decrease in substrate temperature; this is an evidence of dependence of substructure characteristics of the condensates on a substrate temperature. Table 2 gives the data related to the size of the regions

of coherent dispersion (L is a size of crystallites) and microstrain. This information was obtained using the standard Hall plot construction technique at several orders of reflection from the planes [25].

Table 2. The sizes of the crystallites (L) and the values of microstrain (ε) as well as lattice a_{\perp} and c_{\perp} spacing as a function of a substrate temperature

T_s , K	L , nm	ε , %	a_{\perp} , nm	c_{\perp} , nm
570	19	1.1		0.3248
770	28	0.9	0.3041	0.3248
1170	70	0.3	0.3035	0.3246

It follows from Table 2 that the increase in substrate temperature leads to the increase in average size of crystallites from 19 nm at 570 K to 70 nm at 1170 K; the level of microstrain of crystals decreases from 1.1 % down to 0.3 %. In addition with increase of a substrate temperature the TiB_2 lattice spacing is somewhat decreased. It should be noted that the value of microstrains is an evidence of high mechanical characteristics of TiB_2 films.

2.1.2 Film Structure of the W-B System

2.1.2.1 The Electron –Microscopic Data

The W-B films deposited at low temperatures have disordered amorphous (nanodispersed) structure with the small-size inclusions (~5 nm) distributed within the volume. The nature of emissions has not been established yet. However the sorption contrast of these inclusions that can be seen on the electron-&-microscopic images proves their higher absorption ability in comparison with the amorphous matrix. One can assume that these emissions are enriched by tungsten. The typical structure of films is shown in Fig. 12.

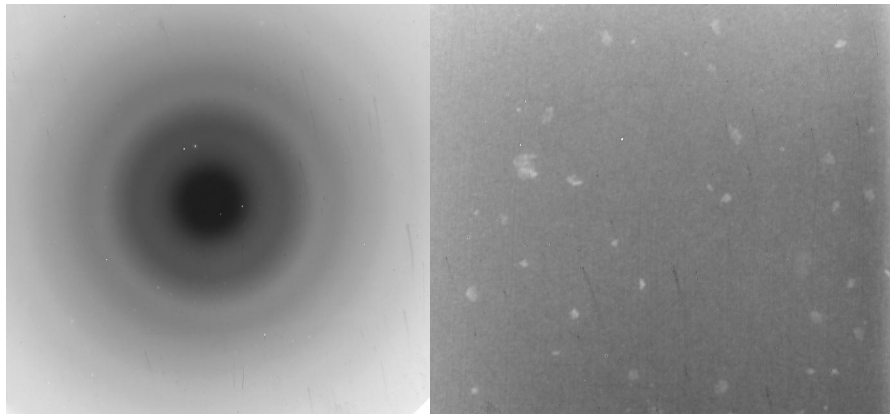


Fig.12. An electron diffraction pattern and a bright-field image taken from a film 12 nm thick obtained using the method of magnetron sputtering of a W_2B_5 target. The substrate temperature T_s increased from a room temperature up to ~500 K on account of radiating influence at preparing of films

2.1.2.2 Structure of Coatings on a Basis of Tungsten Boride

The coatings that were obtained using the triode sputtering of a W_2B_5 target had structure close to amorphous at all conditions sputtering from 0.5 up to 3.5 kV of potential on a sputtered target. The Fig. 13 shows X-ray diffraction pattern from coatings that were prepared by sputtering of a target at a potential U_s 2.3, 2.7, 3.0 kV. The amorphous-crystalline state with

decrease of a potential U_s is formed. The data of X-ray analysis of a coating showed that the films had a crystal phase having a presumably cubic lattice on the basis of metal FCC lattice.

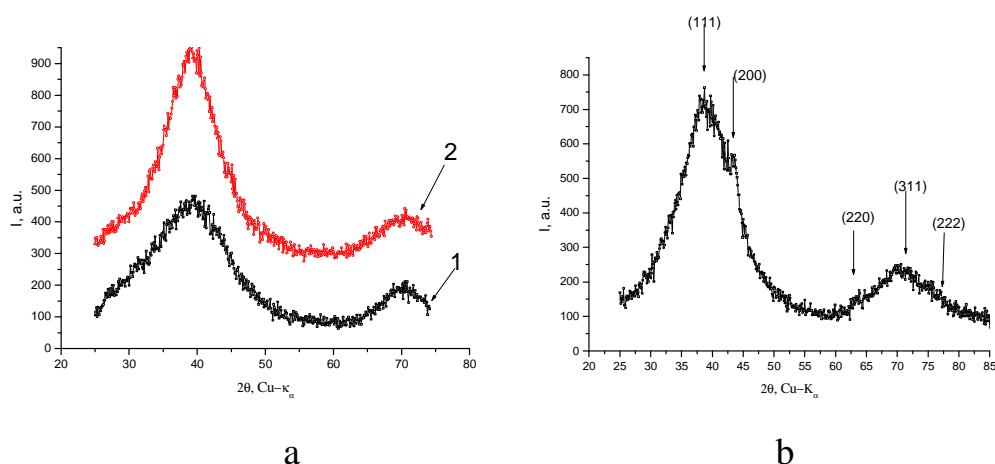


Fig.13. Diffraction pattern of a coating prepared at a potential on a sputtered target:
a – $U_s=2.7$ kV (1), 3 kV (2) and b - 2.3 kV, (Cu- $K\alpha_1$ radiation)

The condensation temperature of coatings at the magnetron sputtering varied with preservation of close other parameters of a deposition. The survey in a condition X-ray diffraction $2\theta > 10^\circ$ have shown (fig. 14, what at sputtering of a single-phase W_2B_5 target (a target had of a hexagon α - W_2B_5 structure) there are characteristic peculiarity.

In condensates obtained at relatively low temperature deposition (570-670 K), on a background of halo from amorphous phase the diffraction peak from nanocrystalline phase with hexagonal crystal lattice, that characteristic for boride of transitive metals (Me), structure MeB_2 (fig. 14, a, curve 1) appeared.

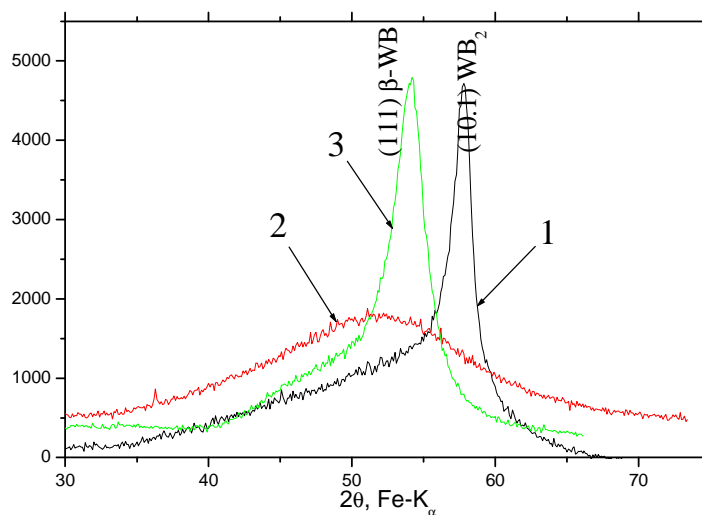


Fig.14. Diffraction patterns of a tungsten boride condensates obtained at substrate temperature 570 K (1), 770 K (2) and 1170 K (3), (Fe- $K\alpha$ radiation)

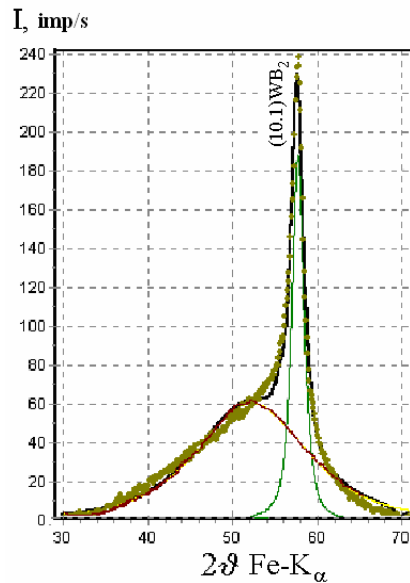


Fig.14a. Section of diffraction pattern with divided maximums according to amorphous and crystalline structural component of a coating ($T_s = 570$ K)

It is known, that amorphous like state is characterized by local chemical ordering with structure of the near order similar to structure of crystals [39]. The average size of amorphous like areas (nanocluster) which have been carried out on a technique [40], in our case gives size ~ 1 nm.

Increase of substrate temperature (T_s) up to 770 K results to formation in films only of amorphous structure with a characteristic angular position of a intensity maximum of a diffraction curve in radiation Fe- K_α $2\theta \approx 51^\circ$.

Increase of substrate temperature up to 1070-1170 K is accompanied by formation of a structural state in films, in which alongside with amorphous component are present nanocrystalline of boride β -WB [41] with strongest diffraction line from a plane (111) (fig. 14, curve 3). The size of crystalline appreciated on broadening of a diffraction line was 12-14 nm.

2.1.3 Coating Structure of the Quasi-Binary TiB_2 - WB_2 System

Prior to the description of the obtained structural results it should be noted that the designation of this quasi-binary system as TiB_2 - WB_2 is rather simplified, because a crystalline lattice of the tungsten boride in its equilibrium state somewhat differs from that of TiB_2 and it corresponds to the W_2B_5 formula [14]. Such a lattice defines a possibility for a higher content of the boron atoms per one tungsten atom (W_2B_5 , in terms of one tungsten atom corresponds to a $\text{WB}_{2.5}$ formula). Therefore, in many papers the quasi-binary system is designated as TiB_2 - W_2B_5 on the basis of participating phases [14, 42]. Such a designation can be used when the difference in the types of lattices of participating components should be indicated. If the comparative content of the components of quasi-binary system is determined then it is convenient to use the TiB_2 - WB_2 notation, which gives an exact ratio of the metal components.

According to the X-ray phase analysis data, the coatings obtained by magnetron sputtering of a target of quasi-binary TiB_2 - W_2B_5 system with titanium boride content more that 40 mole % in substrate temperature range of 550 to 700°C are the single-phase ones. It is a solid (Ti, W) B_2 solution with hexagonal crystal lattice of the same structural type as TiB_2 phase. In (Ti, W) B_2 solid solution, the titanium atoms are replaced by tungsten atoms in metal sublattice at unvaried composition of layers consisting of boron atoms. A single-phase state with peculiar change of lattice spacing in this concentration range of ion-plasma condensates accounts for respective states of solid macrocrystal specimens obtained under conditions similar to the equilibrium ones (region I in Fig.15.) The distinctive feature of ion-plasma coatings in this

concentration range is a decrease in the lattice spacing a with an increase in tungsten boride content. As it was shown above, such a change is defined by decreased content of boron atoms in condensate in comparison with solid macrocrystalline state. According to the research data of the secondary ion-mass spectrometry (mass spectrometer MC7201), the B/(W,Ti) ratio in coatings of 50 mole % TiB_2 -50 mole % WB_2 at $T_s=700^\circ\text{C}$ is 1.96 (in comparison with 2.25 for solid state).

In the concentration ranges II and III (Fig.15), the distinctive feature of ion-plasma MeB_2 condensates (Me is a transition metal) in concentration boride section of W-Ti-B system is a considerable broadening of a single-phase region of existence of $(\text{Ti,W})\text{B}_2$ solid solution with TiB_2 crystal lattice (spatial group $P6/mmm$, the hexagonal lattice with lattice spacing ratio ≈ 1.07 [41]), which is peculiar for the premelting state in case of equilibrium conditions of material production. Under the equilibrium conditions of material production the expansion of a single-phase region for existence of solid $(\text{Ti,W})\text{B}_2$ solution is peculiar for the premelting state. The change in the a and c lattice spacing of a solid $(\text{Ti,W})\text{B}_2$ solution acquires nonmonotonous character (II and III concentration regions in Fig.15) with an increase in the molar content of a WB_2 component in a solid solution in the ion-plasma nanocrystalline coatings at WB_2 content exceeding 62 mole %.

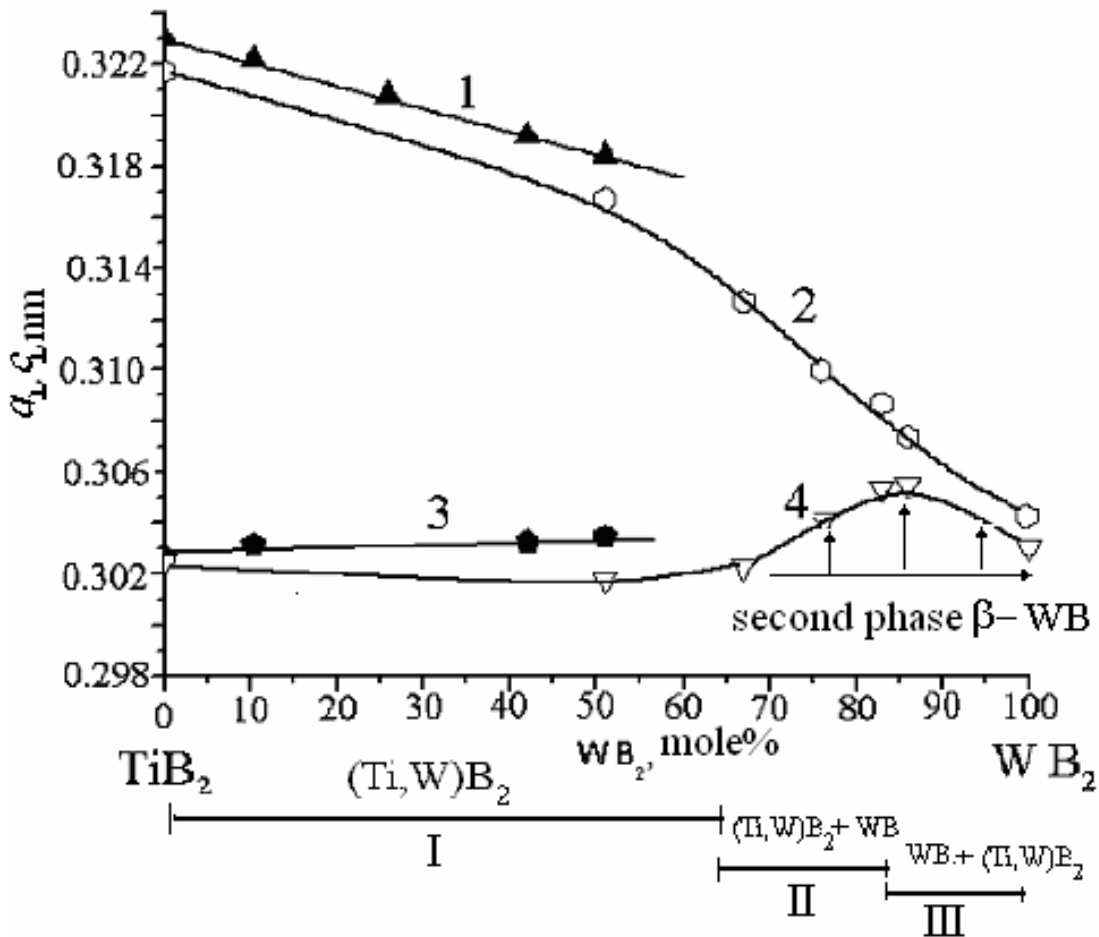


Fig. 15. Change in lattice spacing c_{\perp} (curves 1, 2) and a_{\perp} (curves 3, 4) of solid $(\text{Ti,W})\text{B}_2$ solution on content of WB_2 component in solid macrocrystalline material obtained by hot pressing (curves 1, 3) [15] and in nanocrystalline ion-plasma coating (curves 2, 4, $T_s \approx 700^\circ\text{C}$). (The lattice spacing c_{\perp} and a_{\perp} were obtained under exposure conditions with reflection from lattice planes parallel to the surface (“ θ -2 θ ”))

Let us note that the replacement of Ti atoms with W atoms that have a smaller radius should lead to the reduction of spacing with an increase in W_2B_5 component. In this connection, the increase in a lattice spacing of solid solution in bulk state can be explained by the fact that the true composition of WB_2 component at equilibrium conditions corresponds to W_2B_5 phase or, as it was indicated above, in terms of one tungsten atom it corresponds to $WB_{2.5}$ formula. Thus, the boron atoms should be present in excess in comparison with the TiB_2 . Under the formation conditions that are close to equilibrium (in a bulk state) the excess content of boron atoms can be preserved in a solid (Ti, W) B_2 solution. The interstitial sites in a TiB_2 lattice are the most probable places for the location of excess atoms.

The analysis showed that the centers of the largest interstitial sites in hexagonal TiB_2 cell have the following indices $[[1/3\ 2/3\ 0, 2/3\ 1/3\ 0]]$. Each interstitial site is formed by two triangle prisms (Fig.16). It's sizes along $[120]$, $[210]$ directions in the basal planes of Ti atoms are equal to 0, 0234 nm. Along the $[001]$ directions, these are equal to 0.074 nm. It is seen that the interstitial site is not symmetric (Fig.16). It means that injection of a boron atom ($r_B=0,0875$ nm) into such interstitial site would lead to the increase in both a and c spacing. However the increase in a lattice spacing should be higher than c lattice spacing. Thus, the introduction of 1% boron atoms in such interstitial site leads to the increase in a spacing by 0.00107 nm and in c spacing by a considerably smaller value of 0.000277 nm.

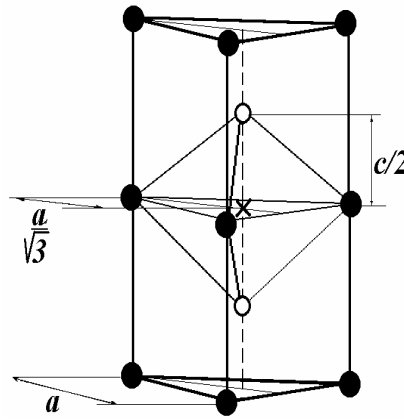


Fig.16. Schematic model of interstitial position of a boron atom leading to the asymmetric change in lattice spacing (at $r_B=0.0875$ nm per 1 at. % boron $\Delta a=0.00107$ nm, $\Delta c=0.000277$ nm)

In order to understand the reasons for nonmonotonic change in lattice spacing of a solid solution in ion-plasma coatings, it is necessary to study the structural features peculiar for three concentration ranges. The I range is of 0 to 62 mole % WB_2 in (Ti,W) B_2 solid solution, in which monotonous change in lattice spacing is observed. The II range is of 62 to 85 mole % WB_2 and the III range exceeds 85 mole % WB_2 in (Ti, W) B_2 solid solution and these lattice spacings display a spacing change nonmonotony different in type.

For compositions of the first concentration range, the increase in T_s is accompanied by a change in intensity of diffraction peaks of (Ti, W) B_2 phases conditioned by the formation of a texture of an axial type in ion-plasma coatings with $[00.1]$ axis.

The degree of perfection of a growth texture in thick ($t=1\ldots 2\ \mu m$) coatings increases with increase in T_s and at $T_s>700^\circ C$ the diffraction spectra reveal only four orders of plane returns $\{00.1\}$. Unavailability of peaks of other types except several orders $\{00.1\}$ on diffraction patterns at “ θ -2 θ ” scanning and at temperature T_s above $700^\circ C$ indicates the appearance of strong texture, which is confirmed by an abrupt decrease in $\Delta\psi$ (Fig.17). The similarity of diffraction patterns for coatings obtained for substrates of a different type (silicon, pyroceramics, tantalum, niobium) indicates the condensation nature of observed peculiarities of structural state and axial-type texture development.

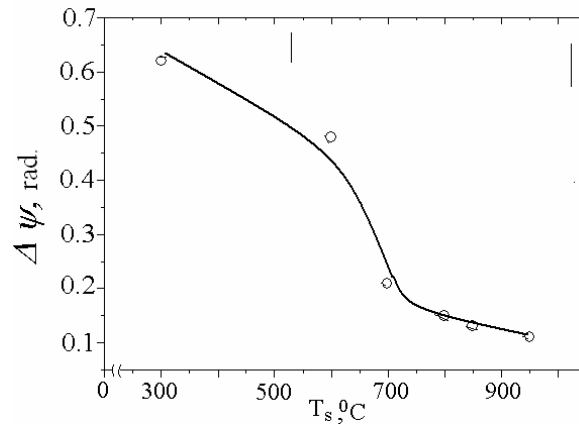


Fig. 17. Change of perfection of texture (00.1) depending on T_s

For the purpose of construction of a volumetric model of the coatings' structure we obtained the X-ray diffraction data both for the case when the diffraction vector (\mathbf{k}) is perpendicular to a coating surface plane and when the diffraction vector lies in a coating plane.

The analysis of substructure characteristics of coatings allowed us to establish the following regularity: the size of crystallites increases with increase in T_s in plane (00.1) normal direction. At $T_s=300^\circ\text{C}$ $L_\perp=13$ nm, at $T_s=700^\circ\text{C}$ $L_\perp=25$ nm and $T_s=900^\circ\text{C}$ $L_\perp=80$ nm. In a coating growth plane the size of crystallites (L_\parallel) is considerably lower and is equal to 4,1...5,7 nm (Table 3). To obtain data in the latter case, we used the wide-angle X-ray transparency exposure of coatings separated from a substrate (Fig.18). Thus, with an increase in T_s the appearance of anisotropy is observed in the average crystal sizes with preferred increase in size along the texture axis [00.1].

Table 3. Crystallite size for coatings $(\text{Ti,W})\text{B}_2$ (Ti/ W obtained at different T_s

$T_s, ^\circ\text{C}$	L_\perp, nm	L_\parallel^*, nm	L_\perp / L_\parallel
100	5,2	3,1	1,68
300	13,0	3,7	3,51
600	19,0	4,7	4,04
700	25,0	4,3	5,81
800	50,0		
950	80,0		

* it is determined by transparency survey (Fig. 18).

The increase in deposition temperature leads to the annealing of defects during formation of crystallites of a coating. It is manifested by a change in microstrain value, which decreases from 1,8 % at $T_s=300^\circ\text{C}$ down to 0,49 % at $T_s=950^\circ\text{C}$ with increase in deposition temperature.

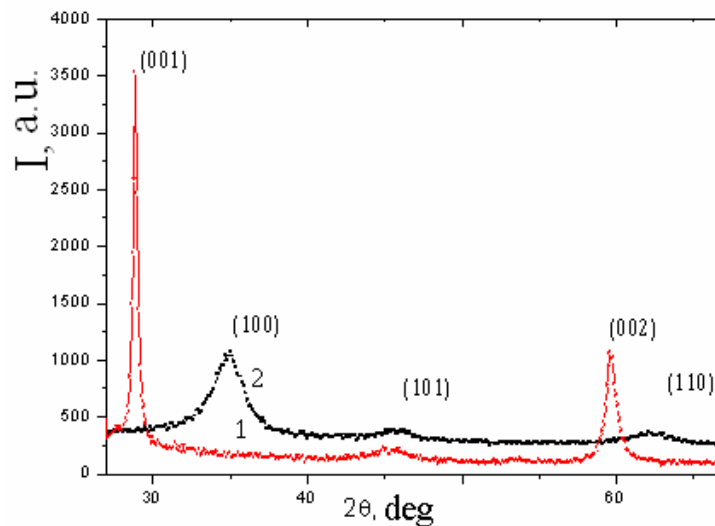


Fig.18. Sections of diffraction patterns for solid solution (Ti,W)B₂ coatings with hexagonal lattice of a 50 mole %TiB₂-50 mole %WB₂ composition taken under condition that the diffraction vector is parallel to the normal of substrate surface (1) and for the condition when a diffraction vector is perpendicular to the normal of surface plane (2), (Cu-K_α radiation)

In order to construct the structural model of ion-plasma coatings we studied in this paper a change in the degree of texture perfection [00.1], crystal size and macrostrain while varying a coating thickness.

The analysis of the results of selection of approximating function (see 1.3) showed that if the size of material crystallites is less than 30nm then the profile shape of diffraction lines in the mean angle portion of spectrum can be described sufficiently well by Cauchy function or quadratic Cauchy function.

This result allows us to perform separation and to define substructure characteristics even in case of superposition of several diffraction lines as shown in Fig.19.

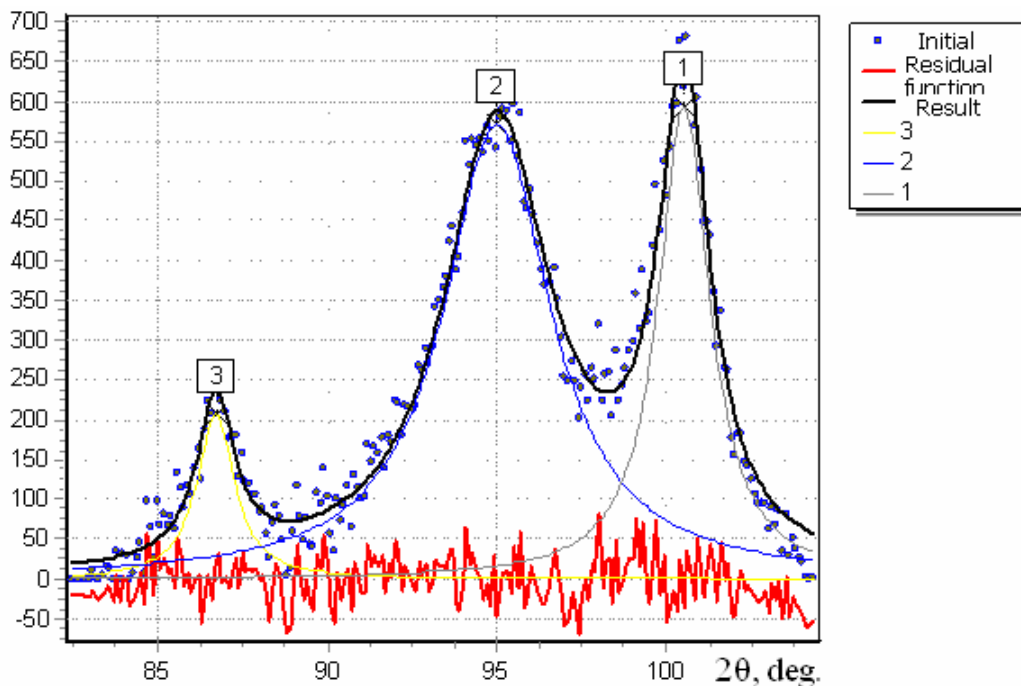


Fig. 19. Processing the intricate diffraction profile with separation of three component peaks using the previously established Cauchy function $(1+\alpha x^2)^{-1}$ of shape approximation

Using the “New_profile” program to process the diffraction data we managed to examine substructure characteristics of the condensates of the following composition 50 mole% TiB_2 /50 mole% W_2B_5 . The diffraction patterns of 3 orders of reflection from the texture plane (00.1) were used for the research; it allowed for obtaining the information in the orientation, which is the most sensitive to variation of such characteristics in hexagonal lattice with layered atomic packing [00.1]. It has been established that with increase in condensate thickness the increase in the average size of crystallites (L) takes place and microstrain reduces ($\langle\epsilon\rangle$) (Table 4).

Table 4. Values of $\Delta\psi$, L and $\langle\epsilon\rangle$ at different condensat thickness for composition 50 mol.% TiB_2 / 50 mol.% W_2B_5 obtained at $T_s=850^\circ\text{C}$

Condensat thickness, μm	$\Delta\psi$, rad	L , nm	$\langle\epsilon\rangle$, %
1,5	0,16	40	0,74
4,0	0,13	52	0,52
8,0	0,12	79	0,48

Due to the fact that with increase in coating thickness the texture perfection growth and higher anisometry of crystallites (with preferred growth in direction of beam incidence of film-forming particles, i.e. towards the coating surface plane normal) are observed. One can assume that the size of crystallites derived from analysis of substructure characteristics is rather exaggerated, with regard to the initial layers of growth, and considerably understated for near-surface layers. In other words, the thickness distribution model for dimensional state of crystallites has the following shape: the weakly anisomeric crystallites are replaced in the initial coating growth layers by increasingly anisomeric crystallites (elongated in direction perpendicular to the growth plane) with increase in coating thickness forming in this way elongated fiber structure of crystallite growth perpendicular to the surface in thick (more than 1 μm) coatings.

Structural peculiarities of the following two concentration ranges are connected, both with change in plane of preferred orientation of growing crystallites of solid $(\text{Ti}, \text{W})\text{B}_2$ solution, and in phase composition of a coating material. Fig.20 gives the sections of diffraction spectra of coatings obtained at $T_s=700^\circ\text{C}$.

It is seen that in the concentration range with Ti/W ratio changing from 0.61 to 0.33, which corresponds to the concentration range of content in a solid solution of 62...75 mole % WB_2 , the second pronounced texture of crystallites of solid solution (10.1) appears and at $\text{Ti/W}<0.4$ the formation of the second nanocrystalline β -WB phase with orthorhombic lattice takes place.

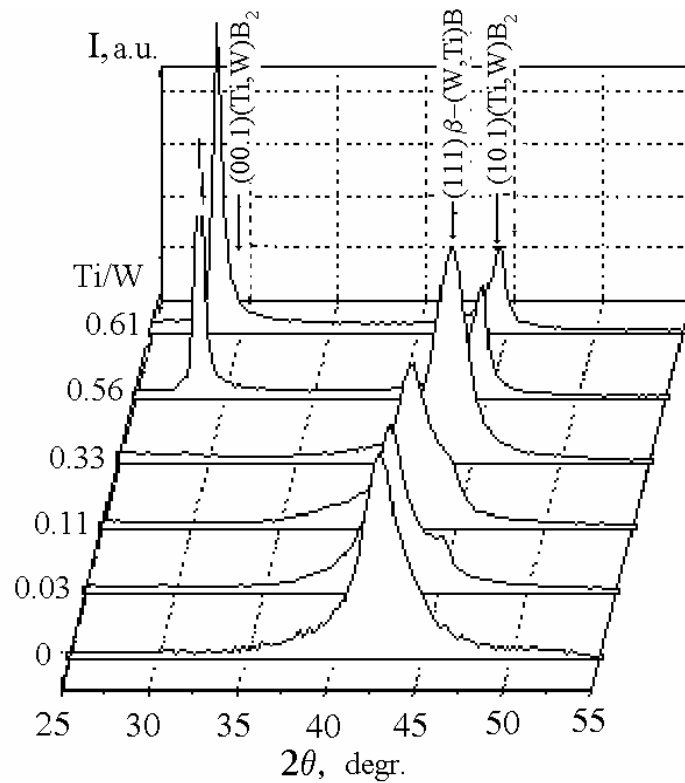


Fig.20. Sections of X-ray diffraction spectra of condensates obtained at $T_s = 700^\circ\text{C}$ with different atomic Ti/W ratio (see left side), (Cu- K_α radiation)

The crystals anisotropy for the second concentration range (with a high content of WB_2 component) is less pronounced. We used for our studies the $(\text{Ti,W})\text{B}_2$ coatings with the $\text{Ti/W}=1/2$ ratio, deposited onto aluminum foil. The X-ray analysis was carried out for two exposure conditions $\mathbf{k} \parallel \mathbf{n}$ (reflection survey) and $\mathbf{k} \perp \mathbf{n}$ (transparency survey) (\mathbf{k} is a diffraction vector, \mathbf{n} is a surface normal). The comparison of diffraction spectra obtained at $T_s=80^\circ\text{C}$, 300°C , 500°C , (Fig.21) shows that at the lowest T_s the formation of amorphous cluster state takes place (Fig.21, a). In this case the clustering is manifested by the appearance of asymmetry of “halo” diffraction at reflection survey (curve 1). It indicates the initial stage of clustering in direction of incidence of film forming particle flux. The substrate temperature of 300°C at deposition is actually a maximum permissible value for formation of amorphous component in coatings of such composition. It is seen from Fig.21b that nanocrystallites of solid $(\text{Ti,W})\text{B}_2$ solution are the main structural component at this temperature. In the coating growth plane (parallel to the substrate surface) the formation of two preferred orientations (00.1) and (10.1) takes place. At the crystal's size in a growth plane of $L_{\parallel}=3.1$ nm, the relation $L_{\perp} / L_{\parallel}$ is equal to 3.38.

The increase in T_s up to 500°C leads to the formation of polycrystalline coating with average crystal size in a growth plane of 4.1 nm and the relation $L_{\perp} / L_{\parallel}$ is equal to 3.9.

If the content of Ti-atoms is less than 17%, the β -WB phase becomes the main component of a coating. The dependence of the volume content of β -WB phase on relative concentration of titanium atoms in a coating is given in Fig.22.

Fig.22 shows that at a ratio of $\text{Ti/W} \leq 0.2$, which corresponds to the TiB_2 phase content less than 17 mole %, the abrupt increase in the volume content of β -WB component with simpler (in case of transition from amorphous state) orthorhombohedral lattice in comparison with hexagonal takes place. Formation of β -WB phase lower in boron atoms should be accompanied by displacement of excess boron atoms from crystallites of β -WB phase with enrichment by them of the second phase component (solid $(\text{Ti,W})\text{B}_2$ solution) of a coating. The manifestation of

this effect can be associated with the increase in a spacing for a solid $(\text{Ti,W})\text{B}_2$ solution in this concentration range, which is given in Fig.15.

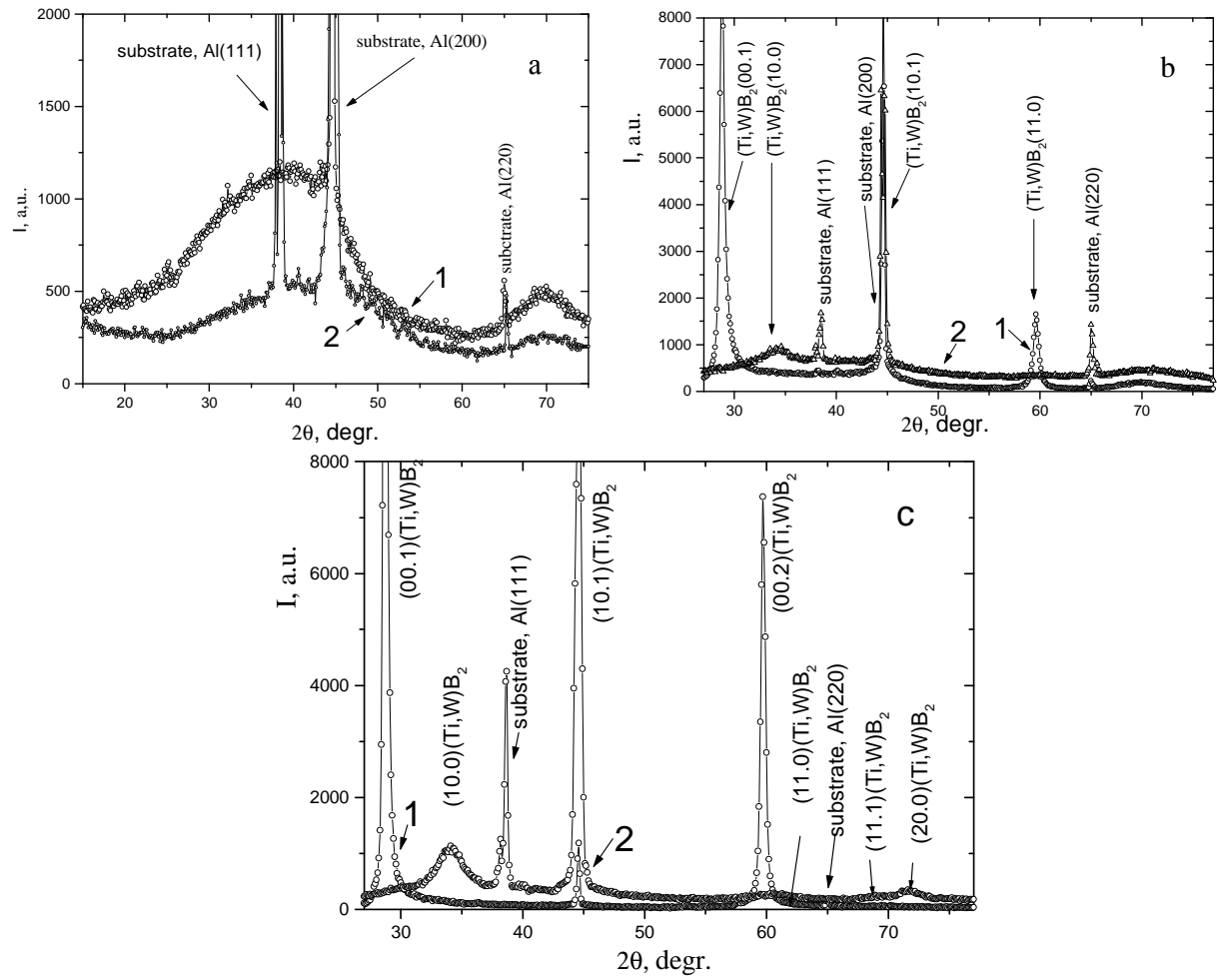


Fig.21. Sections of X-ray diffraction spectra of solid solution $(\text{Ti,W})\text{B}_2$ coatings for composition of 35 mole % TiB_2 – 65 mole % WB_2 deposited onto aluminum substrate at T_s , °C: a- 80, b – 300, c – 500 [$\mathbf{k} \parallel \mathbf{n}$ (1) and $\mathbf{k} \perp \mathbf{n}$ (2)]

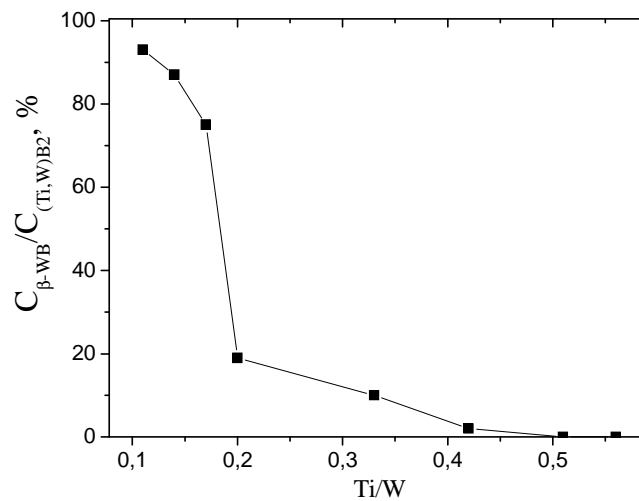


Fig.22. Change of volume ratio of $\beta\text{-WB}$ and $(\text{Ti,W})\text{B}_2$ phases content depending on atomic Ti/W ratio in condensate

2.1.3.1 Macrostrained Condition of Quasi-Binary Coatings of $\text{TiB}_2\text{-WB}_2$ System

The experiments carried out at deposition temperatures of 800-950°C showed the high level of macrostresses in ion-plasma coatings and that the elastic stresses that are developed in films lead to the bend of “film-substrate” system. If we compare the films obtained on pyroceramics and silicon substrates, we will notice that in the case of pyroceramic substrates, such a bend is observed at lower temperature ($T_s = 700^\circ\text{C}$) in comparison with monocrystalline silicon substrates ($T_s = 750 - 850^\circ\text{C}$). The domelike “film-substrate” system flexure (with a dome from a film side) peculiar for the whole concentration range used for scattering the sintered targets of $\text{W}_2\text{B}_5\text{-TiB}_2$ system is indicative of the development of compressive macrostrains in films.

While sputtering the pure W_2B_5 target, the reverse-side system flexure is observed. This is peculiar for the development of tensile stresses in films.

The evaluation of compressive stresses by flexure value of a film obtained by sputtering the 50 mole % TiB_2 -50 mole % ($1/2\text{W}_2\text{B}_5$) system at condensation temperature of 950°C on monocrystalline (111)Si of 385 μm thick using the Stoney formula [26] showed that their values reach 6.5 GPa.

At lower substrate temperature of coating deposition, when the marked substrate bending under action of formed macrostresses is not observed, the elastic deformed state that develops in a coating can be evaluated using the X-ray method of multiple oblique exposures ($\sin^2\psi$ -method).

The conducted analysis showed that in strongly deformed coatings deposited at $T_s = 600^\circ\text{C}$ (Ti/W ratio ≈ 1), the strong compressive deformation reaching the value of -2.8 % is observed. Such high value of elastic strain is indicative of strong interatomic bond of diborides in their condensed state.

In coatings with lower Ti/W ratio, (i.e. with higher specific content of WB_2 component), the texturing degree is reduced and it has impact on the decrease of maximum reached elastic strain. At $\text{Ti/W} = 0.33$ it decreases abruptly and is equal to -0.6% and further reduces down to -0.4% with a decrease in Ti/W ratio from 0.33 to 0.1 (the entire study is related to the coatings deposited at $T_s = 600^\circ\text{C}$).

2.1.3.2 Fractal Studying of Surface

At applying a layer of elastic copper of 40 to 50 nm thick onto a silicon substrate prior to a coating condensation the relaxation of structural compressive stresses that occur inside the film results in 3-D formations (Fig. 23). The individual dome-shaped film sections are evidence of high compressive deformation in a condensate [43]. Fig. 23 shows a picture of a film of 50vol.% TiB_2 -50vol.% W_2B_5 of 1 μm thick.

It is seen that the surface relief is represented by bulging lines. These lines are needle-like and are bulged in the center. Fig.23 shows that the film is almost completely peeled-off in a bulging area; it implies the presence of maximum compressive strains in this area.

The useful information on the properties of such formations can be obtained from the analysis of fractal dimensionality of projection to the cutting plane in a bulged coating region [44] (Fig.24).

A value of fractal dimensionality (D_f) can be evaluated using the grid method, i.e. by a number of grid cells N , through which the line of intersection passes at changing the side of a log grid (l) from ratio $N(l) = \alpha \cdot l^{-D_f}$ or graphically as straight line slope ratio in $\lg N$ (l)- $\lg l$ coordinates [45] (Fig.25). The obtained values of $D_f = 1.23 \dots 1.25$ exceed one (1) (for a straight-line boundary of $D_f = 1$) and in addition these correlate perfectly well with fractal dimensionality of unbalanced winding boundaries of crystals that as we know are formed due to the self-

organized processes [45] On these grounds we can assume that the process of formation of fractographic pattern of bulged condensate areas has an analogous nature.

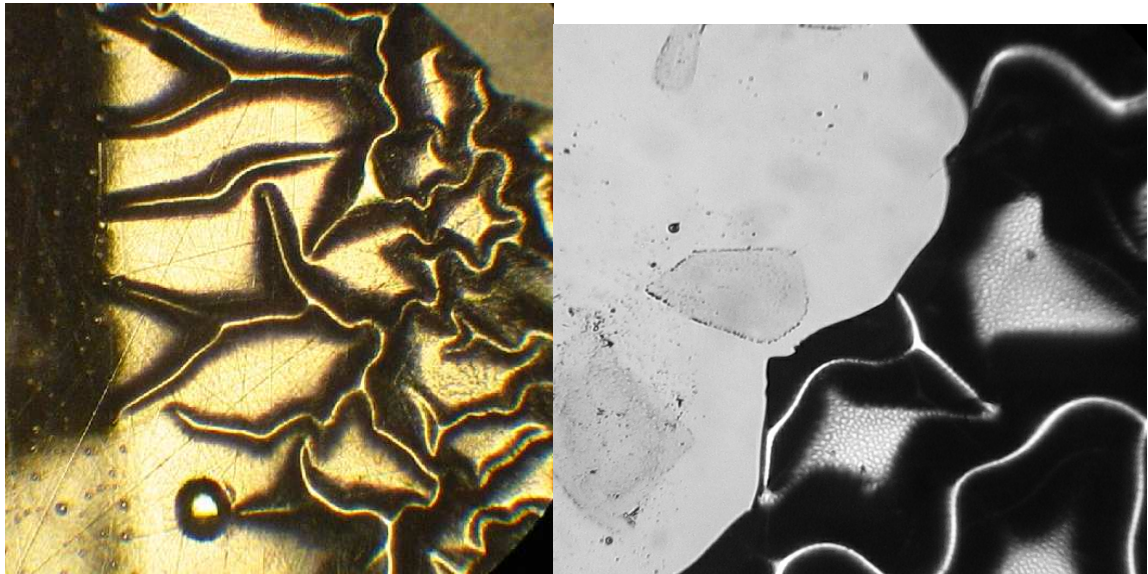


Fig. 23. The microscopic image of a film structure obtained at 1170 K. The survey is done in central part of specimen at multiplying 20

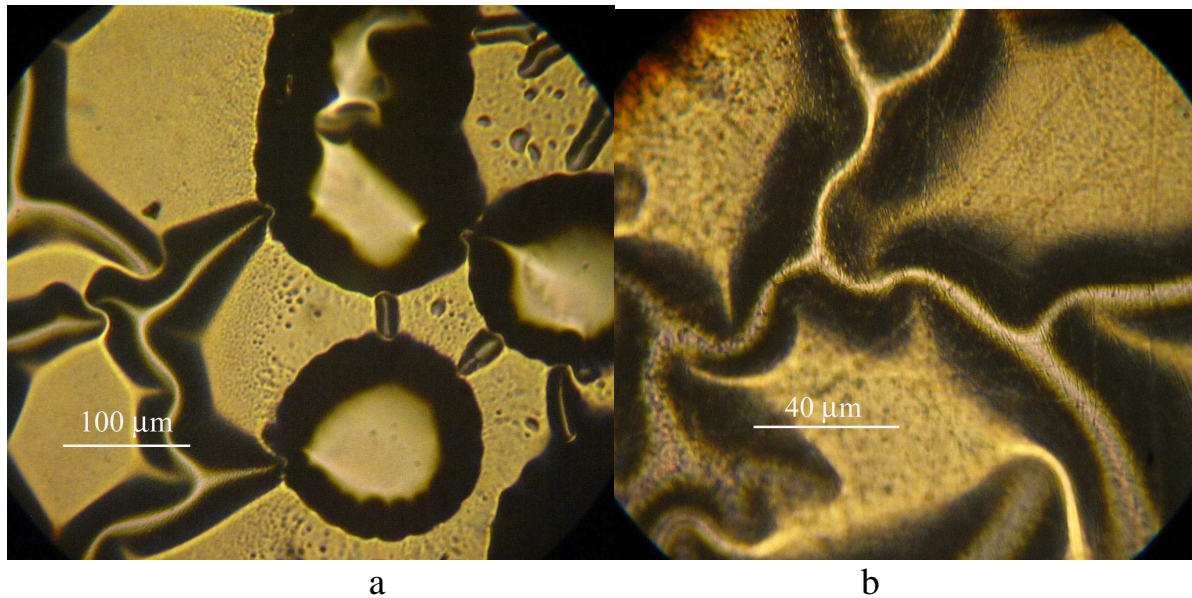


Fig. 24. A view of the 3-D surface formations that appeared due to the structural compressive stresses while depositing condensate onto a copper sublayer of 40 to 50nm thick (a); the enlarged fragment of a branching section of 3-D fractal formations (b)

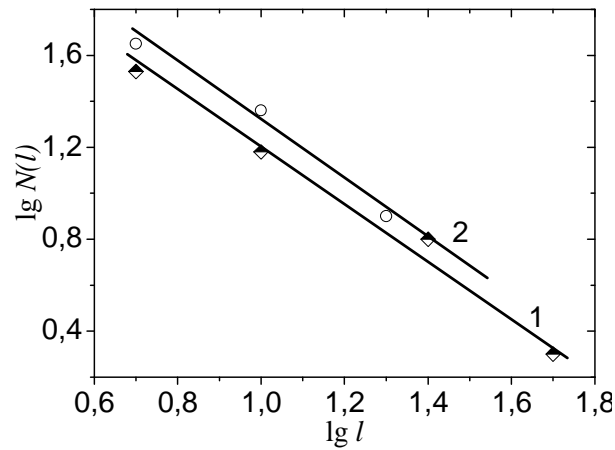


Fig. 25. Diagram $\lg N(l) = f(\lg l)$ for fractal dimensionality of structure on Fig. 24a (curve 1) and Fig. 24b (curve 2)

2.1.4 Phase Composition, Structure and Macrostrained Condition of Coatings Obtained Using the Method of Triode Sputtering of WC Target

The tungsten carbide refers to the interstitial phases, for which the dominant role of chemical bonds between the metal atoms is peculiar while the nonmetal atoms are located inside the metal lattice (at interstitial sites) therefore the tungsten-based interstitial phases can be considered as two sub-lattices: one of them is a modified metal tungsten lattice and the other is an ordered lattice that consists of atoms of interstitial elements; it can have different volume configurations up to the cluster ordering depending on the vacancies density.

The formation of the metastable high temperature β -WC phase with the cubic lattice of a structural NaCl type is a natural phenomenon for the low deposition temperatures of tungsten carbide coatings when the ion-plasma methods of coating formation are used [12, 46].

The previous studies of a structure and strained state of tungsten boride films using the triode sputtering showed the increasing role of a thermal radiation factor. Primarily its impact can be manifested in change of elemental and phase composition peculiar for the triode tungsten carbide films in comparison with condensates obtained through magnetron sputtering [12].

Auger-electron analysis of coatings that were obtained using the method of three-electrode sputtering of α -WC target showed that the coatings obtained at $U_s=0.5-1$ kV contain 42 to 46 at.% of tungsten (mean concentration), 48 to 52 at.% of carbon, up to 2 at.% of oxygen and up to 5 at.% of nitrogen (Fig.26.). With increase in U_s up to 3 or 3.5 kV the concentration of carbon in samples decreases down to 36-40 at.%, and nitrogen down to 3 to 4 at.%.

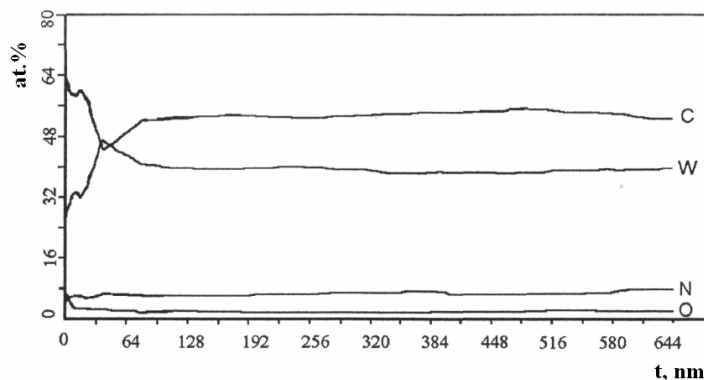


Fig.26. In-depth change (t) of elemental composition of a WC film obtained by triode sputtering at $U_s=1$ kV

At sputtering the α -WC target the coatings with phase composition similar to that of a sputtered target (hexagonal WC) [47], were obtained on silicon and stainless steel substrates at low deposition rates of 0.08 to 0.13 nm/s (a condensed atoms stream $j_{\Sigma} = 8 \cdot 10^{14} - 1.3 \cdot 10^{15} \text{ cm}^{-2} \text{ s}^{-1}$) and substrate heating temperature of 450 to 500°C (Fig.27).

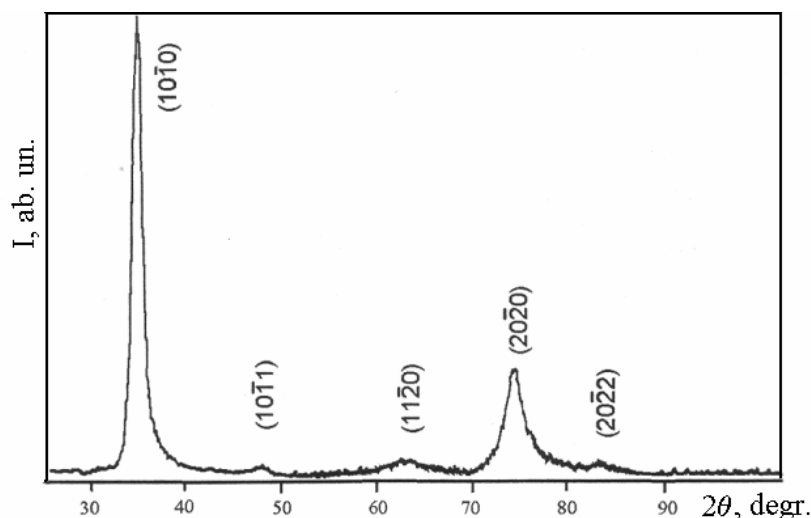


Fig.27. A section of diffraction pattern for a α -WC sample in Cu- K_{α} radiation

The films show the formation of texture of an axial type. Its axis $[10\bar{1}0]$ coincides with the film surface normal and the rocking curve of textured reflex is within 20° . The peculiarity of the initial stages of growth of hexagonal α -WC at the three- electrode dispersion diagram is that a plane $(10\bar{1}0)$ is arranged parallel to the film surface and a close-packed basal plane (0001) is arranged perpendicular to the film surface.

The coatings obtained at the lowest speed of deposition of 0.008 nm/s ($U=0.6$ kV) used in this work had the spacing of $a=0.2941$ nm and $c=0.2843$ nm increased in direction of a film normal and the strain determined in the basal plane (0001) was compressive.

The coatings obtained at $U_s=1$ kV showed that the lattice spacing a and c dropped down to the values of 0.2935 nm and 0.2838 nm, accordingly, remaining somewhat higher than the tabulated values of $a=0.29062$ and $c=0.2837$ nm [47]. In addition the weak plane maximums of β - WC_{1-x} phase with spacing of 0.4264 nm appeared. The average size of crystallites increased from 4 nm ($U_s=0.6$ kV) up to 5.2 nm ($U_s=1$ kV). The increase in U_s up to 3 kV and T_s (due to the substrate bombardment) from 550 to 600°C accordingly lead to the change in phase composition of condensed samples and to the formation of two-phase films (α - $\text{W}_2\text{C} + \beta$ - WC_{1-x}) on the basis of α - W_2C phase. The presence of two the most powerful diffraction maximums from the $(11\bar{2}0)$ and $(10\bar{1}1)$ planes proves the two-component crystallites texture of α - W_2C phase in the formed films. The crystallites of β - WC_{1-x} phase also had the preferred orientation with the plane $(h00)$ parallel to the surface.

The obtained samples (coated substrates) were strained, which is indicative of the presence of significant compressive stresses in WC coatings. The deflection value of coated substrates was used to define the values of compressive coating stresses using the Stoney formula. These were equal to 2....4 GPa and increased with increase in dispersion strain of U_s and accordingly in coating deposition rate. It should be noted that the stress value measured using the bending of coated silicon substrates was in compliance with the stress values measured using the X-ray tensometry.

2.1.5 Phase Composition, Structure and Macrostressed Condition of Quasi-Binary Coatings of TiC-WC System

Let's note that the tungsten carbide has the lowest heat of formation among the transition metals' carbides and therefore it is subjected to a rather noticeable influence of thermal radiation. On the contrary, the titanium carbide has a high heat of formation and therefore it displays the highest resistance to a thermal radiation [10]. To study the influence it produces on the structure and properties of the condensates of tungsten carbides we used in our work a quasibinary WC-TiC system with different volume content of TiC component.

The addition of TiC component to a sputtered target stabilizes the solid (W, Ti) C solution with the cubic crystal lattice of a NaCl type. The Fig. 28 a and b give the diffraction spectra for the coatings deposited onto the silicone substrate at different substrate temperatures. It is seen that with an increase in TiC component the solid (W, Ti) C solution becomes more decomposition-tolerant.

It is known that the formation of phases with lower carbon content in comparison with the initial monocarbide phase occurs via ordering the vacancy subsystem in the carbon sublattice with a lack of carbon atoms in it [10]. Fig.28 shows that such a process has the most intensive character in the textured condensates with [100] axis that were deposited on the flat surface, for example, a silicon surface, for which an angle of scattering at the collision of deposited atoms with a surface is rather low.

Thus, the planarity of a deposited coating and high mobility of carbon atoms at a condensation temperature above 700°C result in their intensive re-evaporation and escape from a condensate deposition region. This process has the most explicit character in the regions enriched with the tungsten atoms. In these regions the carbon depletion occurs up to the formation of crystallites whose high metallic bond stimulates the formation of a cubic bcc lattice peculiar for pure tungsten. The fact that the titanium monocarbide crystallites are formed at a carbon deficiency due to the solid (Ti, W)C solution decomposition, and in addition to the tungsten monocarbide the tungsten carbide and tungsten with lower carbon content (Fig.28) are formed, testifies the availability of more strong Ti-C bonds in comparison with the W-C bonds. This assumption is in good agreement with the Ti-W-C system state diagram: the solid (Ti, W) C solution, which is carbon unsaturated, decomposes not into two simple carbides but into two phases, in particular, W and (Ti, W) C [48].

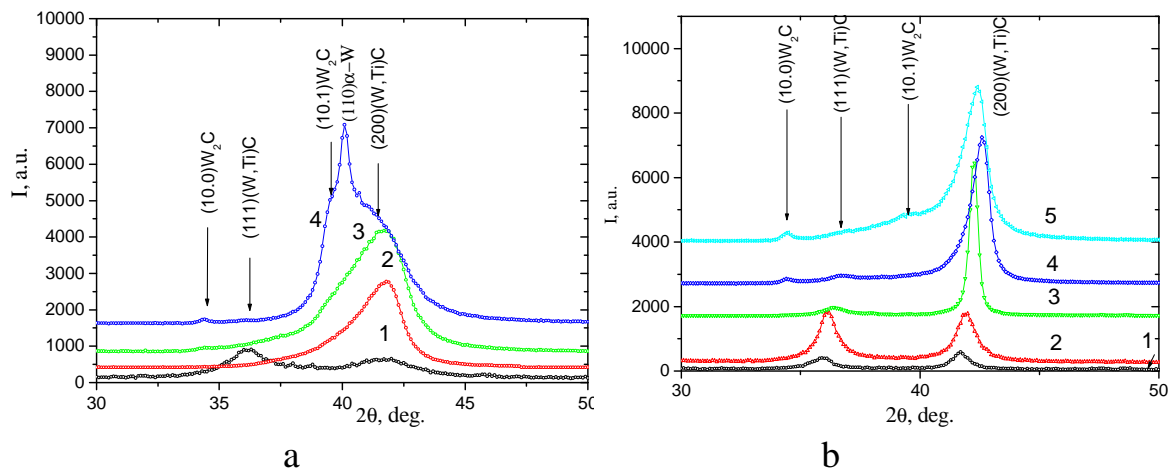


Fig.28. The spectra of X-ray diffraction of ion-plasma condensates obtained through sputtering of a – 15 mol.% TiC – 85 mol.% WC ($T_s, ^\circ\text{C}$: 80 (1), 700 (2), 750 (3), 850 (4)), b – 31 mol.% TiC – 69 mol.% WC ($T_s, ^\circ\text{C}$: 250 (1), 550 (2), 850 (3), 900 (4), 950 (5)) composition target

As it was noted above the formation of a single-phase solid (W, Ti) C solution in a nanocrystalline structural state is peculiar for the entire concentration range of the WC-TiC system studied at a relatively low deposition temperature (less than 300°C). It is accompanied by the formation of actually homogeneous structural state for the substrates of all types used in this work (Fig.29).

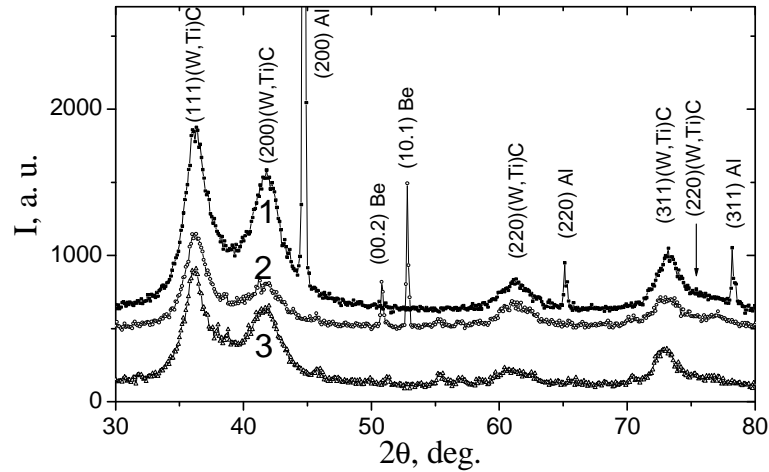


Fig.29. The spectra of X-ray diffraction of ion-plasma condensates obtained through sputtering of 15 mol.% TiC – 85 mol.% WC composition target at substrate temperature 80°C. Substrates: 1- aluminium foil, 2- beryllium, 3 – polished monocrystalline silicon

At a higher substrate temperature ($T_s \geq 300^\circ\text{C}$) and a small content of TiC component (less than 40 mole%) the formation of preferably oriented crystals with the axis [100] perpendicular to a growth plane (see Fig.28 a, b) was observed on the flat polished nickel substrates and on the polished pyroceramics and silicon substrates. At a deposition temperature of 600 to 700°C an abrupt decrease in half-width of diffraction peaks at ψ -scanning (Table 5) is observed and it is indicative of the decrease in the angular disorientation of crystals relatively the texture axis [100] (an increase in the degree of texture perfection). With an increase in a coating thickness the texture perfection improves.

Table 5. Change in the degree of texture perfection [100] in the coatings of 1 μm thick that were deposited onto a silicon substrate while sputtering a target of 15 mole% TiC -85mole %WC composition.

$T_s, ^\circ\text{C}$	80	300	500	600	800
$\Delta\psi, \text{rad}$	0,62	0,41	0,33	0,25	0,12/0,23*

*- coating thickness is equal 0,5 μm

Table 5 gives the data for a coatings of $\approx 1\mu\text{m}$ thick that can be compared with the data given for a coating obtained at $T_s=800^\circ\text{C}$ of 0.5 μm thick (asterisked).

At a high content of TiC component the preferable orientation at low deposition temperature ($T_s \leq 500^\circ\text{C}$) was a crystallite (111) plane parallel to the growth surface. However, in contrast to a texture (100), which is peculiar for the low content of TiC component the degree of texture perfection (111) decreased with an increase in substrate temperature up to 900°C. For the composition of 90mole % TiC-10 mole% WC the texture changes its preferable orientation to (220) (Fig. 30).

According to the data [49] given for the TiC coatings the preferable orientation [100] is caused by the lack of carbon and the transition to a texture [111] is observed with an increase in

a relative carbon content in a film. Specifically, in paper [49] such a transition was reached by increasing a pressure of the reactive C_2H_2 gas or through the intensification of carbide-forming reaction on a surface by heating a substrate to a temperature of above $450^\circ C$.

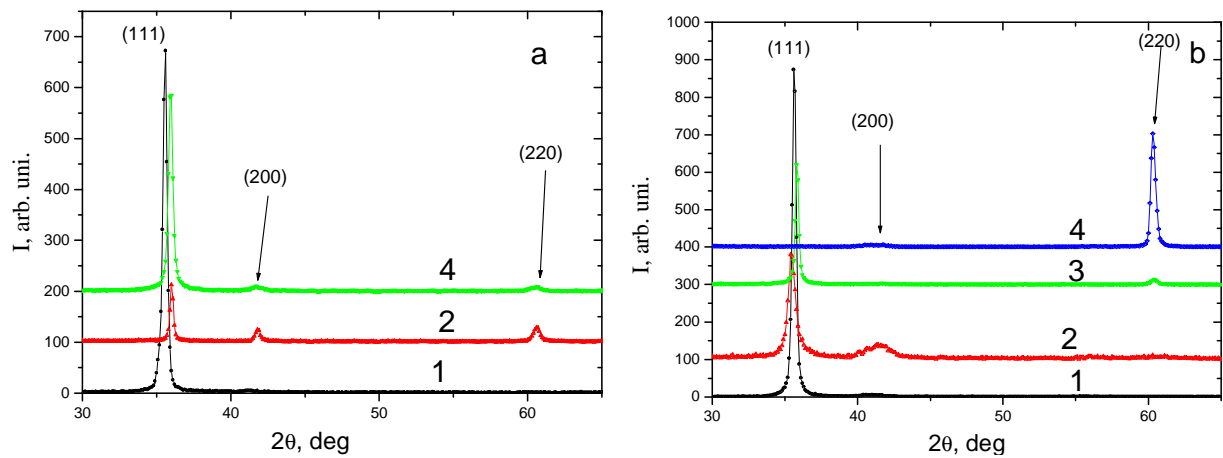


Fig.30. The spectra of X-ray diffraction of ion-plasma condensates obtained through sputtering of 25mol.% WC+75mol.% TiC (a) and 90 mol.% TiC – 10 mol.% WC (b) composition target condensed onto polished (001) Si substrates : 1- $T_s=300^\circ C$, 2 – $T_s= 500^\circ C$, 3 – $T_s=700^\circ C$, 4 - $T_s=800^\circ C$

According to the data given in [49] the texture formation [110] meets certain balance between the deformation energy and surface energy because the values of these two parameters of the plane (110) are in-between the appropriate values for the planes (111) and (200).

Thus, summarizing the data obtained for the texture state of coatings it should be noted that the texture (111) loses its perfection with an increase in temperature and becomes more stable (110) or (100). The appearance of texture (100) is peculiar for the coatings with a high content of WC component, and it (is defined by a deformation factor (minimum strain energy of a crystal lattice at a lack of carbon atoms). Particularly, it is confirmed by an increase in the degree of texturing (100) prior to the transition to the W_2C phase. Thereat, with increase in T_s the texture strengthening occurs.

Due to the insignificant changes in the atomic relationship in the films at a high content of TiC component in the temperature range of $300...700^\circ C$ all the structural changes observed in them can be related to the kinetics of diffusion processes that arise during the deposition. It is proved by the fact that the formation of a texture of any type is not observed in the case of deposition onto a rough beryllium substrate up to a maximum substrate temperature of $700^\circ C$, which is used in this case, i.e. the formation of polycrystalline films without preferable growth is noticeable in the entire temperature range.

On the basis of the angular dependence of the width of diffraction lines for multiple reflections we analyzed the substructural characteristics of condensed materials (crystallites' size and microstrain).

The substructural characteristics for different directions of a diffraction vector can be defined using two modes of survey “for reflection” and “for transparency”. Using “for reflection” survey of the coatings with the average composition of 25 mole % WC -75 mole % TiC on the beryllium substrate (a diffraction vector is perpendicular to the film plane and the value of α_\perp is obtained) we have established that with an increase in a coating deposition temperature in the range of $300^\circ C$ to $800^\circ C$ an increase in the size of crystallites occurs in the direction of incidence of the film-forming particles from 6 nm at $300^\circ C$ to 17 nm at $800^\circ C$. At the same time, “for transparency” survey (the diffraction vector is the growth plane and we

obtain the value of $\alpha||$) shows that the value of the crystallites' size slightly changes in this temperature range and it is within 5,7 ...6,7 nm.

Thus, the crystallites' size in the direction of incidence of a film-forming beam of particles is the most sensitive in the deposition temperature range of 300...700°C. Table 6 gives characteristics of the substructural state of coatings of about 1 μ m thick that were obtained on the silicon substrates using "for reflection" scheme at two deposition temperatures of 250 and 600...700°C.

Table 6. Substructural characteristics of the quasi-binary WC –TiC coatings deposited on different substrate temperature and with different composition

Ts, °C	WC		85 mol.% WC - 15 mol.% TiC		79 mol.% WC - 21 mol.% TiC		69 mol.% WC - 31 mol.% TiC		25 mol.% WC - 75 mol.% TiC		10 mol.% WC - 90 mol.% TiC	
	L,nm	< ϵ >, %	L,nm	< ϵ >, %	L,nm	< ϵ >, %	L,nm	< ϵ >, %	L nm	< ϵ >, %	L,nm	< ϵ >, %
250	9	1,25	5,1	0,95	7,5	0,8	10	0,4	77	0,3	145	0,4
600...700	4,1	0,88	4,5	0,8	22	0,7	70	0,3	57	0,25	200	0,4

It is seen that with an increase in the content of TiC component actually a monotonous increase in the size of regions of coherent scattering is observed in the direction of incidence of the film-forming particles, i.e. a more perfect fiber structure is developed. With an increase in the deposition temperature this process acquires a more explicit character; this is manifested by the increased size of crystallites. The microstrain has a tendency towards decrease (Table 6) both at relatively low and high deposition temperatures with an increase in content of TiC component. Such a character of changes that are observed in the substructural characteristics can be conditioned by a stronger covalent bond in a TiC component, which defines the development of structural states that are more stable to the action of compression stresses. In this connection a macrostrain is a rather important characteristic that defines a stability of the structural state and properties of the coatings. The studies of the surface of coatings that were deposited at a low temperature onto a brittle silicon substrate showed that in many cases high macrostrains that appear at a coating formation result in "separation" (burst) of a portion of the coating from the bonded portions of a silicon substrate. The method of multiple inclined surveys ($\sin^2\psi$ -method) was used to study the macrostrains in this paper.

Table 7 gives the macrostrain and macrostress values for different coatings' compositions that were derived from the experimental data. It is seen that at a low deposition temperature the coatings are subjected to the action of compressive stresses (marked with "-"), which is accompanied by the development of the compressive strain in the crystalline lattice.

Table 7. Macrostrains and macrostresses for coatings of different composition in WC – TiC system deposited into polished silicon substrate

Ts, °C	WC		79 mol.% WC - 21 mol.% TiC		69 mol.% WC - 31 mol.% TiC		25 mol.% WC - 75 mol.% TiC		10 mol.% WC - 90 mol.% TiC	
	ϵ , %	σ^* , GPa	ϵ , %	σ , GPa	ϵ , %	σ , GPa	ϵ , %	σ , GPa	ϵ , %	σ , GPa
250	-1,3	-3,22	-1,6	-4,1	-1,8	-4,7	-2,9	-7,7	-2,1	-5,4
600...800	-0,15	-0,45	-0,1	-0,34	-0,3	-0,87	-0,37	-1,1	-	-

* - at computation of macrostresses ($\sigma = E\epsilon/(1-\nu)$) the E values obtained using the method of nanoindentation were used

At the same time at a high deposition temperature the value of macrostrain is relatively low and does not exceed -0.4%. The value of $\sin^2 \psi_0 = 0,39$ derived for the cubic lattice from a $\sin^2 \psi_0 = 2\nu/(1+\nu)$ relationship at the intersection of “ $a - \sin^2 \psi$ ” graphs for the coatings deposited onto the different substrates (beryllium, silicon, nickel) defines the value of Poisson's ratio (W,Ti) C for a solid solution in a condensed state, which is equal to $\nu \approx 0,24$.

The obtained data (Table 7) show that the influence produced by a TiC component on macrostrained state of a coating is manifested by an increase in the value of elastic residual macrostrain sustained by a coating. The maximum elastic macrostrain sustained by a coating both at a low coating deposition temperature of 250°C and at a high temperature of 800°C corresponds to a 75 mole% TiC-25 mole% WC composition, and being deposited onto a brittle silicon substrate it is equal to -7,7 GPa and -1,1 GPa, accordingly.

A macrostrain was calculated for the coatings of the same composition (75 mole% TiC-25 mole% WC) deposited onto a beryllium substrate using the survey results “for reflection” and “for transparency” and the values of a_{\perp} and a_{\parallel} that were obtained during calculations. The calculations showed that the values of compressive strain obtained at a relatively low deposition temperature of 300°C both for (111) ($a_{\perp} = 0.4371$ nm, $a_{\parallel} = 0.4332$ nm) plane and for (200) ($a_{\perp} = 0.4376$ nm, $a_{\parallel} = 0.4337$ nm) plane are actually the same and are equal to $\epsilon = -0.8\%$.

In the case of a high deposition temperature of 800°C the spacing values are equal to: $a_{\perp} = 0.4331$ nm, $a_{\parallel} = 0.4319$ nm; it corresponds to the strain value of $\epsilon = -0.42\%$. Such a decrease in a macrostrain value cannot be related to the different coefficients of thermal expansion (low CTE for a substrate), because $\text{CTE}_{\text{Be}} = 16,7 \cdot 10^{-6} \text{ K}^{-1}$, which is a high value and in this case one can expect the additional increase in a compressive macrostrain in a coating at cooling. Therefore, such a difference can be explained by a partial strain relaxation and, accordingly, by a macrostrain of a coating due to the “film-substrate” system flexure during a film-forming process, as the experiment shows. Thus, these stresses cannot be correctly evaluated from a flexure due to the partial relaxation of such stresses caused by the presence of the plastic deformation in a relatively thin beryllium substrate.

2.1.6 Modeling of the Open Space Factors for the Simulating Tests

A space environment is a huge research field for obtaining the new data on fundamental characteristics of a substance that are manifested under the influence of factors of the open space (OS) and for developing the new industrial branches and technologies, in particular, for producing the high purity materials with special properties, functional and protective film coatings, multilayered film structures for the micro-and-nanoelectronic devices, space astrophysics of X-ray range, etc [50].

A development of physical basics for the space technologies requires the development of appropriate devices and numerous experiments should also be carried out. Our domestic astronautics has been involved in such experimental work since 1978, when the orbital “Saliut - 6” station was involved, for the first time, in carrying out the experiments related to the evaporation and condensation of metal substances on the substrates made of different materials (see [51, 52]).

These experiments were carried out to solve an important problem dealing with providing an opportunity for the restoration and repair of multiple structural, functional and protective coatings, spacecrafts and other large-size structures intended for the long-term operation in the open space in addition to studying the fundamental regularities of formation of the condensed materials in the open space environment. This problem is still topical and the work done over the last few years is related to the efficient use of such an open space factor as the space vacuum including new opportunities and prospects for the industrial use of space as a technological environment. In addition, it has been shown that during an orbital flight it is possible to realize a vacuum with the evacuation levels of 10^{-10} - 10^{-12} torr and lower [52] behind the flat screens in

the aerodynamic trace. It opens big prospects for the development of space technologies related to the synthesis of multilayered heteroepitaxial structures, using the method of molecular beam epitaxy and other contemporary methods.

Therefore, the problem of reliability and longevity of the materials and devices of aerospace equipment is becoming increasingly important and topical due to their use for the spaceships with the long operation life up to 15 or 20 years.

Over the last few years we gained a certain experience in full-scale testing of different materials in the open space [51, 52]. The main space-&-physical factors that define the kinetics and mechanisms of degradation processes, a character of influence produced by the aggressive OS factors on the functionality of materials, structure elements and spaceships' devices have been established. It has been revealed that the long –term exposure to the OS factors results in erosion, change in shape and change in physical, chemical, electrical, optical and other characteristics of metals and alloys [52].

A lack of fundamental knowledge and physical understanding of the nature, mechanisms and regularities (at the atomic and molecular level) of the main elemental acts and processes that occur in the structural materials subjected to the action of strong multiple factors in the open space, such as high vacuum (10^{-6} - 10^{-7} torr), influence of electromagnetic solar radiation in the wavelength range of 5 to 2500 nm, action of protons and electrons of the natural and artificial Earth radiation belts in the broad energy range of ($10\text{ keV} < E < 10\text{ MeV}$), cyclic temperature changes in the broad range of (4.2-450) K, influence produced on materials and structures by the strong electric fields of $E=20$ to 30 kV that arise due to the electrization are the main barriers on the way to the solution of the above problem.

The most promising and relatively inexpensive way to solution of this problem is to create a simulator in the terrestrial environment to simulate the influence produced by the strong space factors with further comprehensive studies of physical and mechanical properties of new materials straight in the simulators (under the action of radiation, mechanical stresses, thermal changes, electrical and magnetic fields) and to analyze the mechanical, optical, dielectric, structural and other properties of the irradiated materials in order to work out the substantiated recommendations on their functionality and fitness for the aerospace equipment. The final task that requires a large scope of research is to create a physical model of formation and degradation of different structures subjected to the action of the open space factors in order to predict their behavior in the case of their long exposure to the open space. The research done is a definite step towards the solution of the given problem.

One more important problem is to develop a technology for the creation of new materials suitable for the solution of the problems related to the effective use of the space for the mankind needs. The structural materials and different functional (protective, wear-resistant, heat-resistant, heat-control, light adsorption, etc) coatings, amorphous alloys, quasi-crystals, composite nanomaterials with the unique properties refer to such materials. Therefore, the search experiments carried out in order to study the structure and properties of some types of the given materials were the subject of the research done in order to create a new technological base. The most important are the results of research of structure peculiarities of the materials that are promising for the indicated fields. These materials are required for programming the service parameters of the materials; for understanding the regularities of influence produced by the space-&-physical factors on stability of such parameters; for forecasting and improving the materials' functionality resource and for working out the recommendations that are needed for the development of the appropriate technologies that can be applied for the space material science and aerospace equipment.

2.1.6.1 Impact Produced by the Open Space Factors on a Structure and Substructure of Quasi-binary Coatings of TiC-WC System

The analysis of the phase composition of specimens of quasi-binary TiC-WC system that were obtained in a wide concentration range (of 90 mole % to 10 mole% TiC) revealed no formation of new phases under irradiation action. The coatings' substructure is also rather stable to the external action simulating the open space factors.

While analyzing a width of diffraction lines of coatings right before and after irradiation one can notice a slight decrease in a width of samples with [111] texture. Figures 31 to 33 give the specific X-ray diffraction spectra with low content of TiC component either with the lack of [111] texture (Fig.31) or rather weak [111] texture (Fig.32). In the first case the irradiation causes no change in a width of diffraction lines (crystallites size remains to be equal to 9 nm). However, in case of weak texture (Fig.32) the irradiation is accompanied by increase in crystallites sizes from 10 to 12 nm and at a strong texture [111] (Fig.33) peculiar for the higher TiC content in a coating the irradiation leads to the increase in the average size of crystallites from 28 to 31 nm.

Thus, the irradiation in the open space environment at a dose corresponding to that of one year's exposure causes no considerable changes in composition and substructural characteristics.

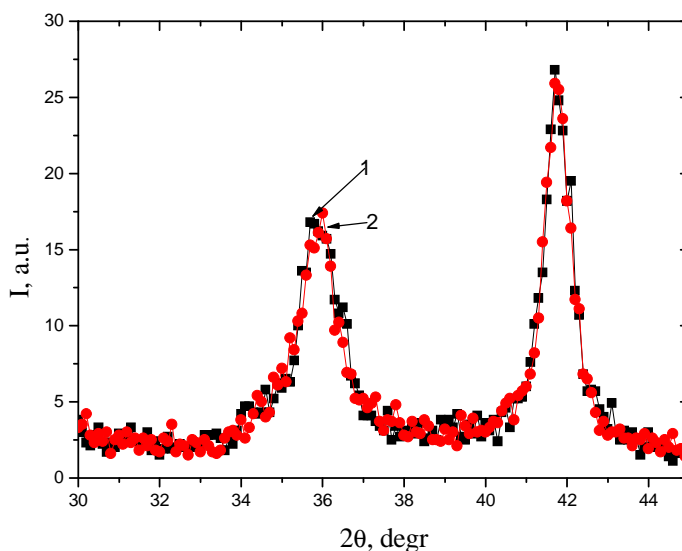


Fig.31. The spectra of X-ray diffraction of coating 20 mole % TiC-80 mole.% WC condensed at $T_s = 300^\circ\text{C}$, 1- initial, 2 – after irradiation

The stressed state of coatings appeared to be rather sensitive to the irradiation. The coatings under investigation that were obtained in the substrate temperature range of $100\ldots 700^\circ\text{C}$ were subjected to the action of compressive stresses. The value of compressive strain of a crystalline lattice in coatings with low content of TiC component (10...30 %) in a post-condensation state was equal to $-0.5\ldots -1.4\%$. At high content of TiC component (70...90%) the maximum value of compressive strain in a coating was somewhat higher and reached $-2.4 \ldots -2.5\%$. The effect of high elastic strain in coatings with high content of TiC component was explained by us by a higher bonding force in comparison with WC (one can judge thereof on the basis of TiC formation heat, which is 5 times higher in comparison with that of WC).based on the results obtained in the ninth and tenth quarters of work done under the given project.

Table 8 gives the results of research of macrostrained state of unirradiated and radiated portions of a coating (to reduce the comparison error a portion of a coating was tightly covered with metal foil, which allowed the foil-covered film to remain in its original (unirradiated) state).

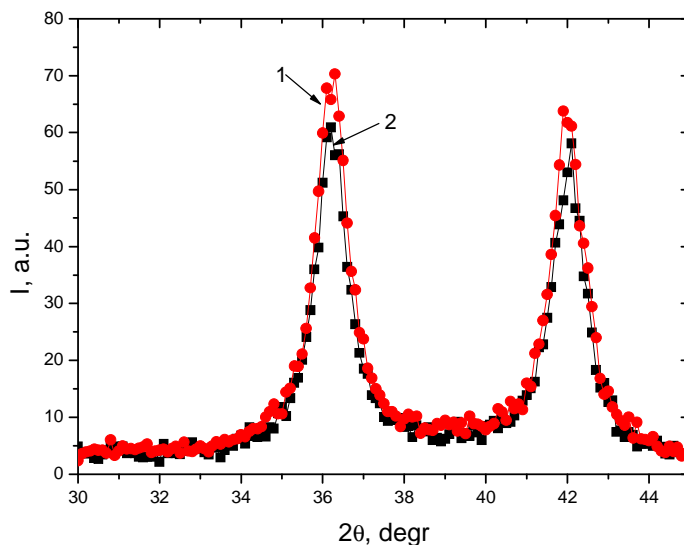


Fig32. The spectra of X-ray diffraction of coating 20 mole % TiC-80 mole.% WC condensed at $T_s = 500^\circ\text{C}$, 1- initial, 2 – after irradiation

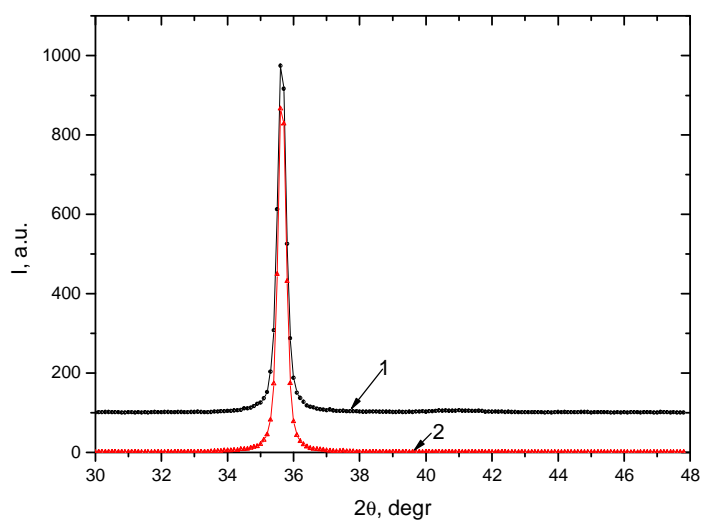


Fig.33. The spectra of X-ray diffraction of coating 90 mole % TiC-10 mole.% WC condensed at $T_s = 300^\circ\text{C}$, 1- initial, 2 – after irradiation

The last column of Table 8 gives data related to the lattice spacing in a stress-free section, which show the monotone decrease in spacing with increase in WC component: it is defined by a smaller radius of atoms and ions in comparison with that of titanium atoms and ions.

Table 8 shows the tendency common for all investigated samples, i.e. the irradiation leads to partial relaxation of initial compressive strain, which is developed accordingly under action of compressive stresses.

Table 8. Results of macrostrained state studies of coatings obtained using the $\sin^2\psi$ -method.

Composition of coating	$T_s, ^\circ\text{C}$	$\varepsilon, \%$		$\Delta\varepsilon/\varepsilon, \%$	a_0, nm
		initial	after irradiation		
90 mole %TiC-10 mole % WC	300	-2,4	-1,8	25	0.4332
80 mole %TiC-20 mole% WC	300	-2,2	-1,55	29,5	0.4327
30 mole %TiC-70 mole% WC	300	-1,27	-0,65	49	0.4293
20 mole %TiC-80 mole% WC	500	-0,95	-0,4	58	0.4287

It should be noted that in the coatings with the highest initial elastic compressive strain (which corresponds to the samples with highest content of TiC component) such relaxation is the lowest in comparison with the initial one (column $\Delta\varepsilon/\varepsilon$ in Table 8). The relative change in composition of 90 mole% TiC-10 mole % WC at irradiation dose that corresponds to that of one year's exposure in the open space is equal to 25%. However, for the coating of 80 mole%TiC-20 mole %WC the relative decrease in the elastic compressive strain reached 29, 5%.

The highest relative strain is observed in the coating maximally enriched with WC component. A relaxation character of structural compressive strain observed in the coating crystallites can be explained on the basis of a model of the cascade formation during irradiation by high energy protons. According to the explanation based on this standpoint the cascade formation in the material with prevalence of carbide with a low heat of formation (in this case WC) is simplified. Accordingly, the relaxation of initial compressive strains conditioned by surplus interstitial atoms in the initial (straight after the formation) coating state can be manifested to a greater extent. Annihilation of a portion of surplus interstitial atoms with the radiation-enhanced vacancies during irradiation occurs in the dislocations' cascade. This provides a partial relaxation of initial structural elastic compressive deformation, which is observed in the irradiated coatings.

2.1.6.2 Impact Produced by the Open Space Factors on a Structure and Substructure of Quasi-Binary Coatings of $\text{TiB}_2 - \text{WB}_2$ System

The studies of influence produced by the radiation factor that simulates the near-Earth space factors were conducted using the $\text{TiB}_2\text{-WB}_2$ samples of equiatomic composition of metal atoms. The irradiation of coatings did not result in the noticeable change of the phase composition (see Fig. 34). As before the irradiation the samples remained to be a single-phase $(\text{Ti,W})\text{B}_2$ solid solution with the crystallites that have a hexagonal crystal lattice. A size of crystallites was not subjected to the noticeable changes either; these preserved their nanocrystal structure. However, the insignificant increase in the line width in terms of Seliakov-Sheerer formula is indicative of the increase in their average size from 22 nm before the irradiation and up to 19...20 nm after the irradiation. Such an impact on the coatings resulted in the insignificant degradation of the degree of perfection of their initial growth texture with a (00.1) plane parallel to the surface growth (Fig.34, curves 1,2).

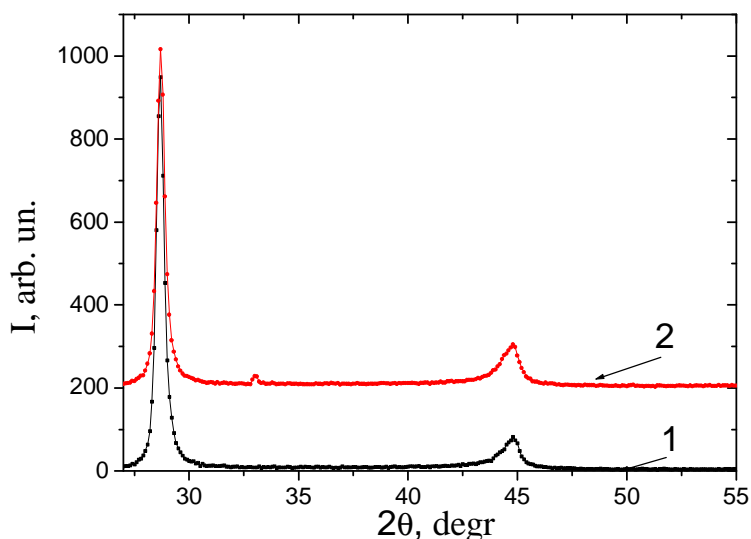


Fig. 34. The spectra of X-ray diffraction of coating 50 mole % TiB_2 -50 mole.% WB_2 condensed at $T_s = 700^\circ\text{C}$, 1- initial, 2 – after irradiation

Such a decrease is manifested by a change in the ratio of integral intensity reflected from the crystallites' texture plane (00.1) and, for example, (10.1) plane. Prior to the irradiation the texture maximum ratio of (00.1) to (10.1) was equal to 9 and after the irradiation it decreased to 7.2.

The irradiation by an annual dose of the open space factors produced the strongest effect on the change (relaxation) in the initial compressive strain of a crystal lattice that arose in a coating during its formation under action of "atomic peening" effect. A compressive strain of -1,0% was developed in a film in its initial state, i.e. straight after the deposition. After the irradiation the strain value went down to -0.76%. Thus, due to the irradiation the coating acquired a more thermodynamically balanced state. It is known that the strain results in the increase of the system energy by a $1/2E\varepsilon^2$ value, where E is a Young modulus of a coating.

If we compare the results obtained in this quarter with the data obtained for the quasi-binary WC-TiC system given in the report for the II quarter we will see that the irradiation produces the primary impact on the deflected state both of the ion-plasma boride coatings of quasi-binary system and carbide coatings making their state more equilibrium or less strained due to the partial relaxation of structural strain in a lattice.

The influence produced by the near-Earth space factors on the phase composition and substructure characteristics of coatings is rather weak and its' effects are usually not revealed using the above structural methods.

Thus, the influence of the Near-Earth space factors does not lead to the structure degradation for the types of coatings obtained in this work and by creating the conditions for partial strain relaxation and due to the transition to a more equilibrium state it allows us to predict an increase in the service life of coatings subjected to the influence of the Near-Earth space factors.

2.2 Stresses, Physical and Mechanical Properties of Films and Coatings That Was Determined Using Tests of Flexure Console and Tension

2.2.1 Determination of the Modulus of Elasticity Using the Dependence of Flexure Console

A considerable substrate deformation is observed during ion-plasma deposition of boride films. The deformation of substrates testifies that in films there are compression stresses. The sign of stresses did not depend on structure and kind of a substrate. This experimental fact is an evidence of good adhesion between film and substrate and high film strength properties.

The stresses that arise in films give an idea of the mechanical properties of those films. The stress value of σ_f was determined from deflection of a cantilever substrate, using the well-known Stoney formula [53, 54]:

$$\sigma_f = E_s t_s \delta / 3l^2 t_f, \quad (14)$$

where E_s is the Young modulus, t_s is a substrate thickness, l is a substrate length, δ is a free end deflection, t_f is film thickness.

Fig.35 and Fig. 36 show the experimental dependences of δ on thickness t_f of a amorphous-nanocrystalline Ti-B film that was formed on a stainless steel substrate and mica (00.1) - muscovite substrate.

Two stages of cantilever deflection caused by structural stresses in a film and by difference in coefficients of thermal expansion of a film and substrate have been revealed.

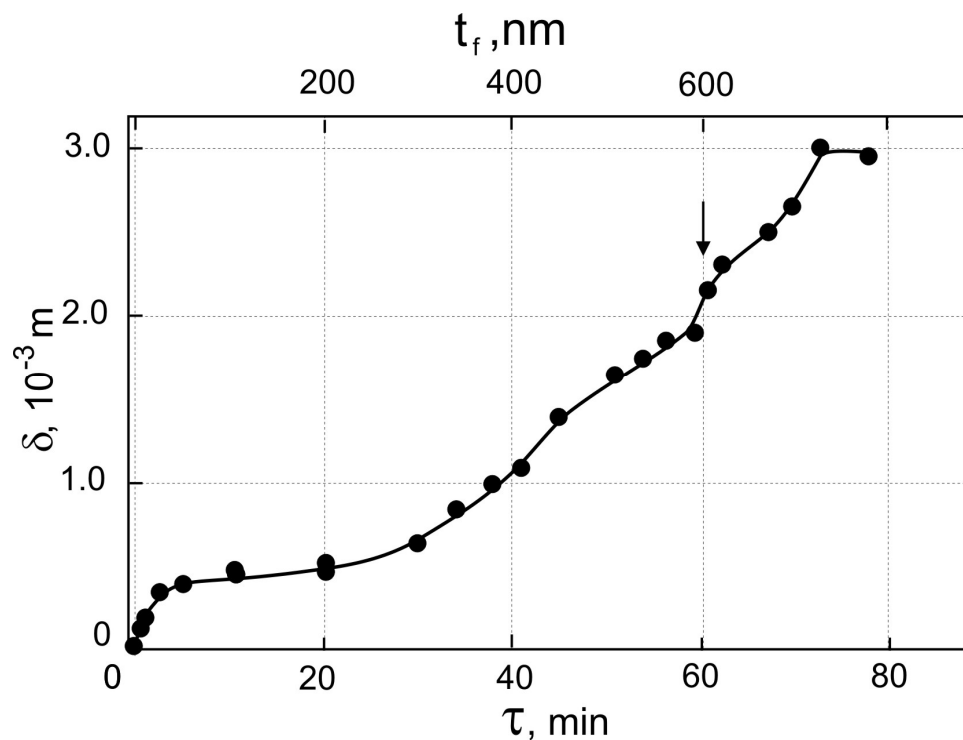


Fig. 35. The dependence of deflection of a cantilever substrate made from stainless steel (grade X18H10T, $E_s = 220$ GPa) while the film thickness gradually increased up to $t_f = 600$ nm with its further cooling from 500 K down to room temperature within 18 minutes. The arrow indicates the point at which the film deposition was completed. The substrate length was $l_s = 20$ mm and width $b_s = 40$ mm

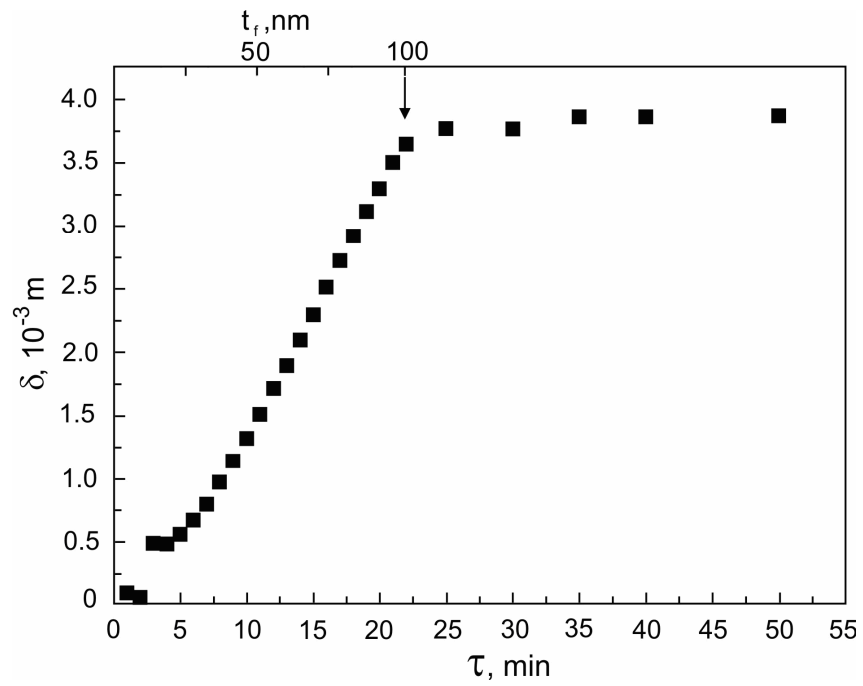


Fig. 36. The dependence of deflection δ of a cantilever substrate (mica $t_s = 22 \mu\text{m}$) on thickness of a growing film. The arrow indicates the point at which the film deposition was completed. The substrate length was $l_s = 30 \text{ mm}$ and width $b_s = 6 \text{ mm}$

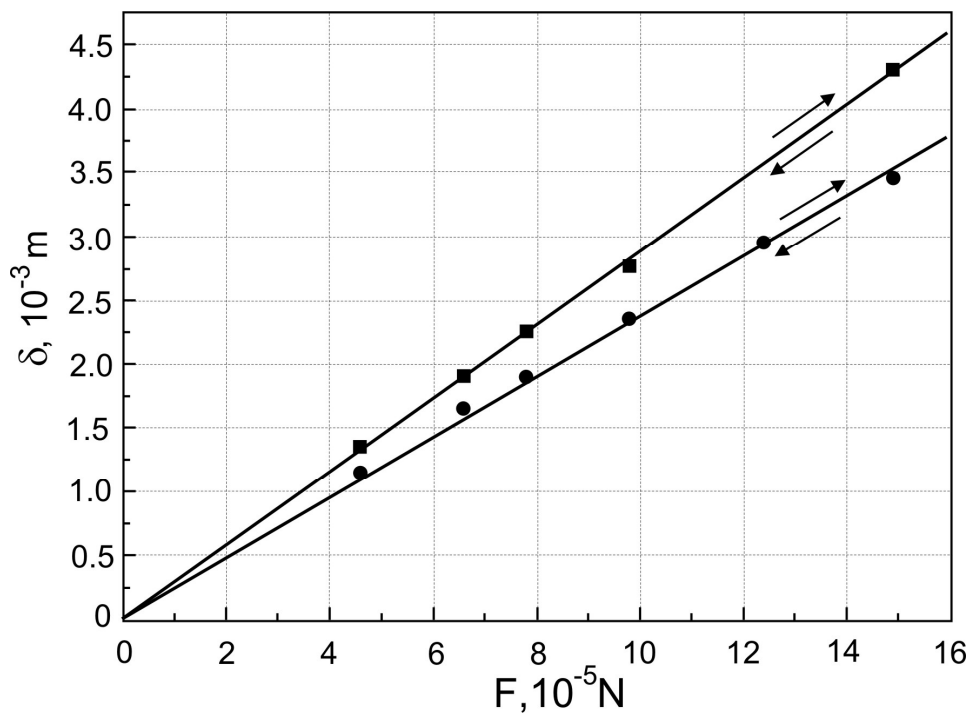


Fig.37. The dependence of a substrate deflection δ (mica, $t_s = 15 \mu\text{m}$, $l_s = 30 \text{ mm}$, $b_s = 6 \text{ mm}$) (upper straight line) and the same film-coated substrate ($t_f = 300 \text{ nm}$) (lower straight line) on the applied load F

The table values of the Young modulus from stainless steel ($E_s = 220$ GPa) were used to calculate the stresses in a film that was deposited onto a steel substrate and for the mica substrate the modulus was determined experimentally from the dependence of a deflection value of δ on load F applied to the cantilever (Fig.37, upper straight line) using relation [54] due to the wide data spread:

:

$$E_s = 4Fl^3/b_s t_s^3 \delta \quad (15)$$

For the mica the value of Young modulus was $E_s = 185$ GPa.

The stresses σ_f in the films deposited onto a stainless steel substrate reached 2 GPa and in the films deposited onto a mica substrate of 22 μm and 15 μm thick reached 1.4 GPa and 0.2 GPa, accordingly.

In order to determine the Young modulus of the amorphous -nanocrystalline Ti-B film from the dependence given in Fig.37 (lower straight line) the effective modulus of elasticity E_o was preliminary determined for mica with the film deposited onto it and intended for analysis.

The experimental data obtained on dependence of a substrate deflection on the applied load F are enough well approximated of line:

$$\delta = 4Fl^3/E_o b t_s^3 \quad (16)$$

It is important to note that the dependence between δ and F was the reversible one. The linear dependence and reversibility allowed for determination of the effective modulus of elasticity for a film-coated substrate using (16).

It has been shown within the bounds of the theory of elasticity [55] that the effective modulus E_o for the film-substrate system is defined by the relation

$$E_o = \frac{(E_s t_s^2 - E_f t_f^2)^2 + 4t_s t_f t^2 E_s E_f}{(E_s t_s + E_f t_f) t^3}, \quad (17)$$

where E_s, E_f are Young modules for a substrate and film, accordingly, t_s and t_f is thickness of a substrate and film, $t = t_s + t_f$.

The experimental data obtained on deformation of a cantilever substrate and film-coated substrate (Fig.37) were used to determine the values of the modules of elasticity of a substrate $E_s = 185$ GPa and effective modulus of elasticity of the same film-coated substrate $E_o = 207$ GPa. At such values of the modulus of elasticity E_s and E_o the modulus of elasticity E_f of studied amorphous -nanocrystalline Ti-B films was 590 GPa. These values are very similar to the available references data obtained using the method of nanoindentation for coatings [56] and massive titanium boride [57]. It should be noted that the method of nanoindentation is used for experimental determination of the Young modulus using a film normal and the present method is used to determine the Young modulus in the film plane.

The mechanical stresses σ_f that occur in the films W-B during their deposition were determined from the flexure of console substrates manufactured from textured permalloy band (a chemical composition is as follows: 0.39 mass% Mn, 51.51% Fe, 48.1% Ni) and tungsten foil using formula (14).

A value of the Young Modulus for the used substrates was determined experimentally using the dependence of flexure δ on load F (Fig.38 and Fig.39) applied to console from ratio (15).

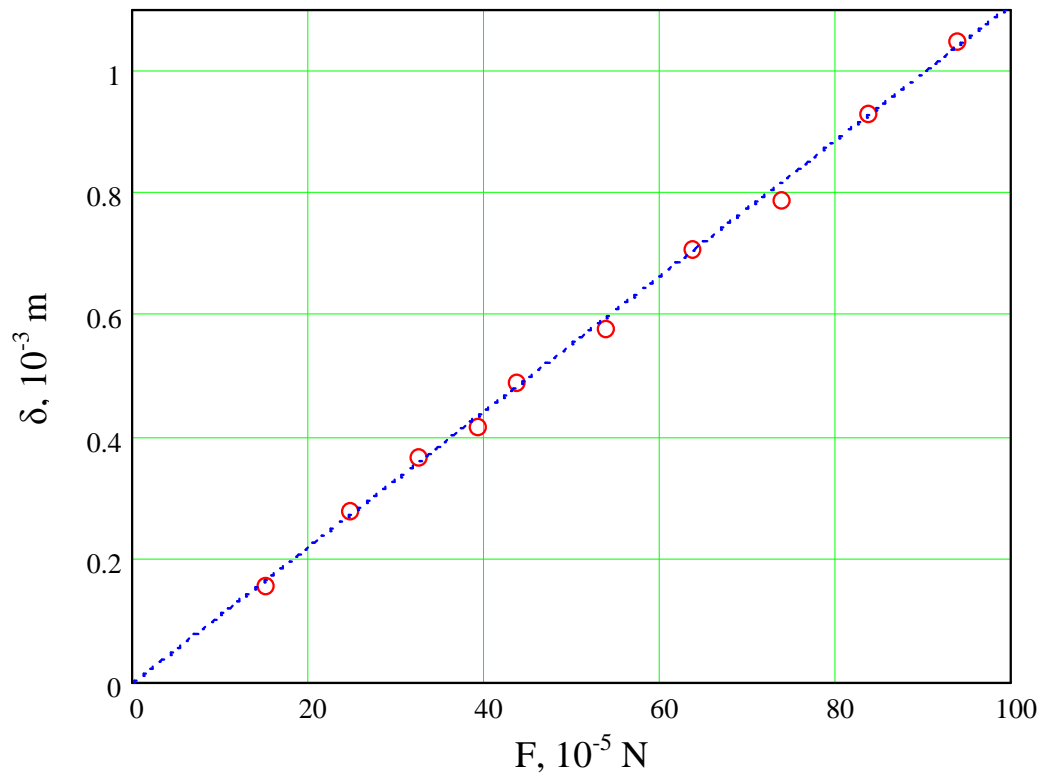


Fig.38. The dependence of deflection δ of a substrate (permalloy, $t_s=46 \mu\text{m}$, $l_s=30 \text{ mm}$, $b_s=5 \text{ mm}$) on the applied load F

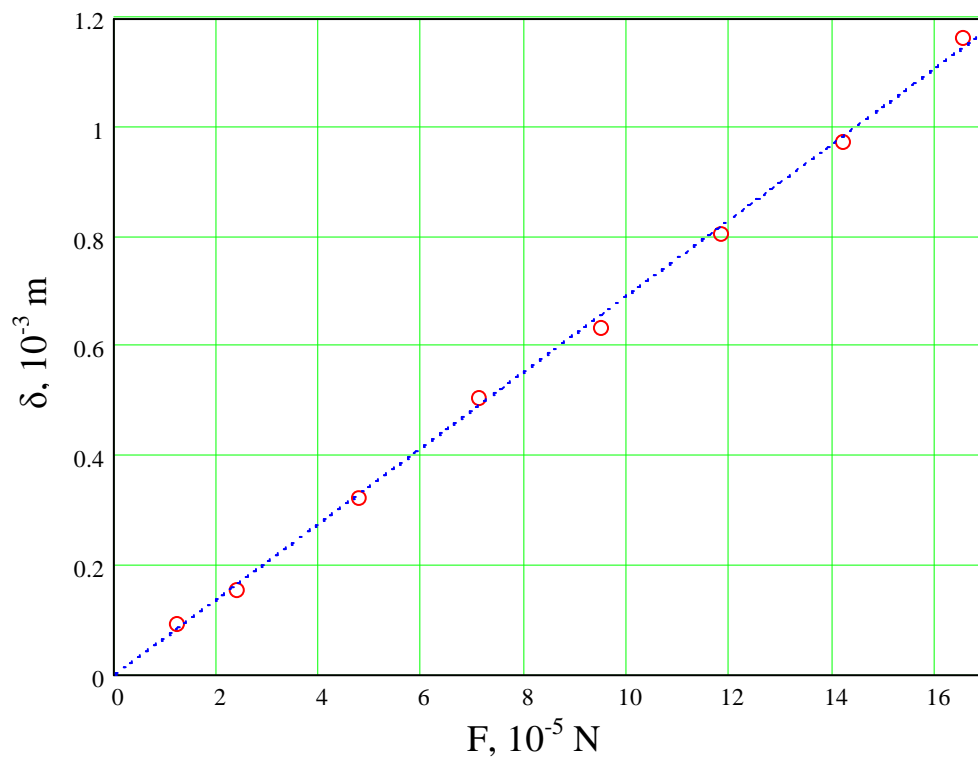


Fig.39. The dependence of deflection δ of a substrate (tungsten, $t_s=20 \mu\text{m}$, $l_s=30 \text{ mm}$, $b_s=5,1 \text{ mm}$) on the applied load F

The tungsten console is of interest because the Young modulus for isotropic tungsten for all the crystallographic lines and consequently the texture influence are reduced here to zero. We have used this material to verify the correctness of technique employed to define the modulus of elasticity. A value of the Young modulus derived from the above experimental dependences was 200,6 GPa and 382 GPa for permalloy and tungsten, accordingly. The value of $E = 328$ GPa obtained by us is very similar to the value given in the references for tungsten monocrystal ($E = 389$ GPa) [58] and we managed to determine the modulus of elasticity for permalloy of a prescribed composition for the first time.

The level of compressive stresses σ_f in a film W-B deposited onto a permalloy substrate reached the value of 0.32 GPa (at a film thickness of $t_f = 436$ nm) and in a film deposited onto tungsten substrate this value was equal to 0.1 GPa ($t_f = 334$ nm).

The value of the given modulus of elasticity E_0 for a film-coated tungsten substrate ($E_0 = 401,3$ GPa) was derived from the experimental dependence of $\delta = f(N)$, as shown in Fig.40 (a straight line 2).

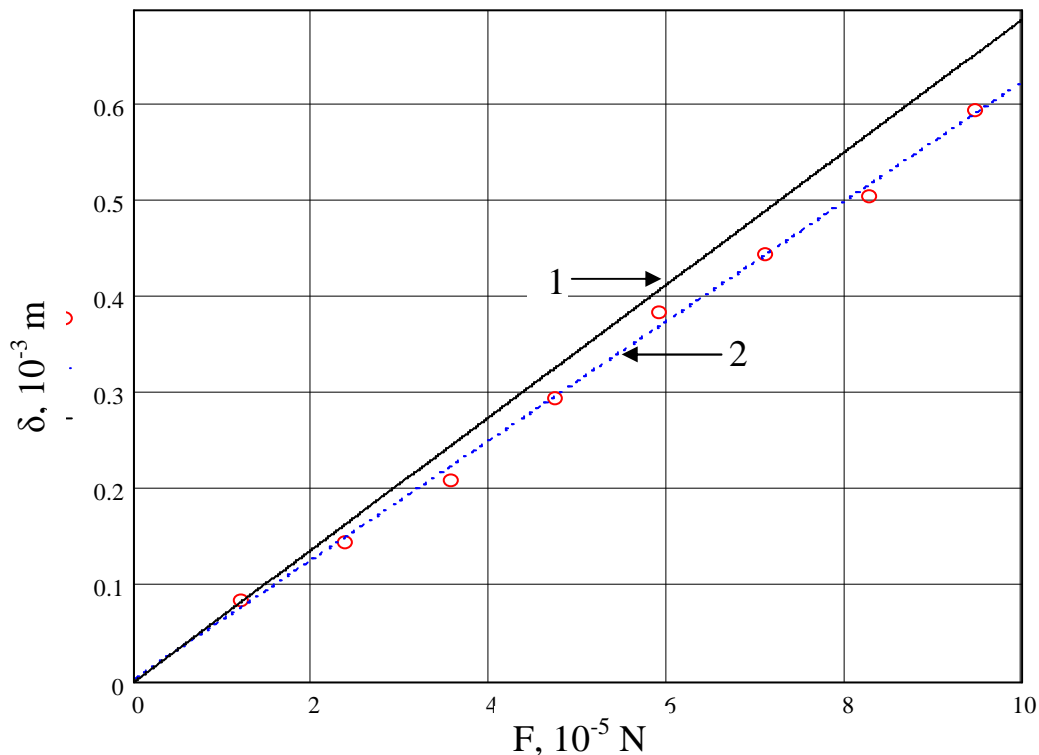


Fig.40. The dependences of deflection δ of a substrate (tungsten, $t_s = 20$ μm , $l_s = 30$ mm, $b_s = 5,1$ mm) (upper straight line -1) and the same film-coated substrate ($t_f = 334$ nm) (lower straight line-2) on the applied load F

A value of the Young modulus for a nanodispersed W-B film is equal to $E_f = 794 \pm 60$ GPa (at absolute film thickness measurement error of $\Delta t_f = \pm 25$ nm). The obtained value of the modulus of elasticity exceeds two-fold the analogous values obtained using the method of nanoindentation at different specimen points (see below).

2.2.2 Defining the Condensates Strength While Studying Tension

2.2.2.1 Defining the WC Coatings Strength While Studying the Samples Tension

The strength value of coatings was calculated using the test results and measurement results of tensile test diagrams for copper foil and copper foil with a film deposited onto it. The rule of additivity of foil and coating properties at tensile deformation of samples [59] served as a

basis for computation. The strength of coatings was determined based on the value of samples strengthening at deformation.

The copper foil samples of 50 x 5 mm were manufactured to carry out mechanical tests. The smooth uniform WC coatings were obtained on the samples after substrates were subjected to ion purging while condensation temperature did not exceed 500°C. A good adhesion of these coatings is proved by the fact that the separation of layers after condensation with further sample tension has not been observed.

The method of determination of properties of the coatings is as follows. After testing the coated and uncoated copper foil samples and knowing the tension parameters one can determine the tensile stress in a coating using the rule of additivity of composition properties:

$$\sigma_f(\varepsilon) = \frac{\sigma_c(\varepsilon) - \sigma_s(\varepsilon)t_s/t}{t_f/t}, \quad (18)$$

where ε is a tensile strain; σ_c , σ_f , σ_m is a stress in a coating-substrate system and in a coating and in a substrate, accordingly; t_f , t_s , t is a thickness of a coating, uncoated and coated substrates, accordingly.

Figure 41 gives the averaged tensile test diagram for copper foils of 70 μm thick and WC-coated foils of 3.5 μm thick.

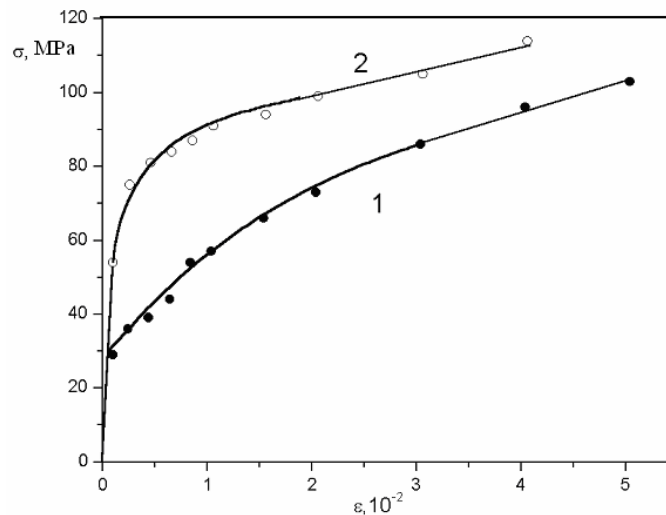


Fig. 41. Tensile test diagram for copper foil (1) and coated WC foil (2)

Fig.41 shows that the diagrams have a linear section of elastic loading of coated and uncoated substrates. The effect of essential strengthening of coated copper foil (curve 2), which was apparently possible due to the special properties of a coating, draws our attention. The curve 2 gives information about origination of film collapse, which can be determined from abrupt decrease in strain-hardening coefficient. The microscopic studies of a coating surface show that the cracks in coatings begin their propagation exactly at these strains. The tensile stress acting in σ_f film can be determined using the stress value in a substrate –coating system σ_c and substrate σ_s as given in diagrams (Fig.41) and a ratio (18). The coating strength is determined at a point of critical deformation, which is characterized by abrupt change in strengthening of a coated sample.

The studies of strength characteristics for tungsten carbide coatings at tension of thinner samples of 1 μm thick go on. At this stage of work the samples from copper foil coated with tungsten carbide WC have been fabricated. The copper foil was 45 μm thick and the WC coating was 1 μm thick. The coatings were deposited onto the foil using the method of ion-plasmous

dispersion at a target voltage of 1.5.kV and current density of 5 mA/cm². The samples with the test portion of 50x5 mm² have been fabricated and subjected to the tension tests.

The obtained stress-stain diagrams for coated samples and original pure foil samples were used for computing the coating strain. The foil –coating system is examined from the standpoint of the theory of strengthening the composite material on the basis of stresses additivity in the firm and elastic layers [59]. The coating stresses were calculated at fixed strains in terms of composition stresses and pure original foil stresses. The coating extension diagrams have been obtained. Fig. 42 gives the dependence $\sigma=f(\epsilon)$ for WC coating of 1 μm thick.

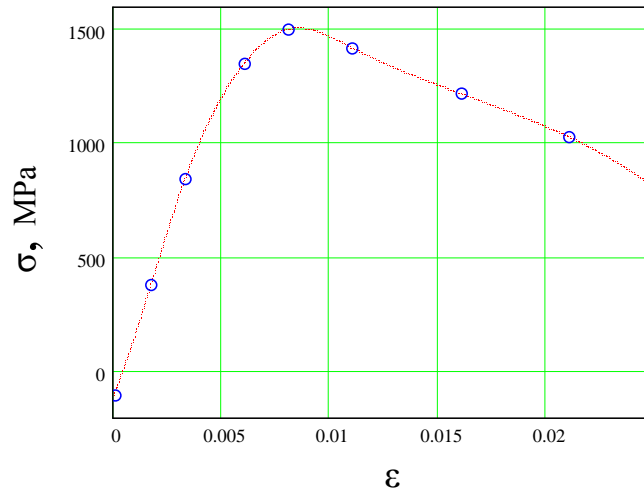


Fig.42. Assumption diagram for WC coating extension of 1 μm thick

The presented diagram shows the initial section of strengthening, the stress maximum that characterizes the coating strength and further drop in stress. The presence of the stage of elastic loading of a coating is evident. According to the estimate it corresponds to the elasticity modulus of 300 to 400 GPa. The stage of coating disintegration due to the formation of cracks transverse to the loading axis is also present. In this case the maximum tensile stress reaches 1.5 GPa; it corresponds to the level of a coating strength.

The strength value of WC coatings obtained due to the analysis of stress-strain diagrams makes up 1...2GPa. The stress-strain diagrams (Fig.41) show that the strain prior to coating disintegration was about $0.3 \cdot 10^{-2}$.

2.2.2.2 Defining the W-B Coatings Strength While Studying the Samples Tension

The studying of dependence «stress–deformation» of the coatings W-B gives to curve Fig.43. Table 9 and Fig.44 give the results of computation of deformation characteristics for the W-B coatings deposited onto permalloy substrate.

Table 9. Assumption tension diagram «foil 49 μm thick –coating 1.6 μm thick »

σ_m , MPa	σ_c , MPa	σ_f , MPa	E_{total}	C_f	C_m	t_f , μm	t , μm
451,48	500,45	1826,59	0,0018	0,032	0,979	1,6	49
459,94	516,34	2064,34	0,0023	0,032	0,979	1,6	49
538,23	586,75	1869,98	0,003191	0,032	0,979	1,6	49
582,26	605,52	1108,98	0,003911	0,032	0,979	1,6	49
604,28	614,91	728,75	0,005021	0,032	0,979	1,6	49
621,41	619,6	351,24	0,006107	0,032	0,979	1,6	49
631,19	629	345,78	0,007156	0,032	0,979	1,6	49

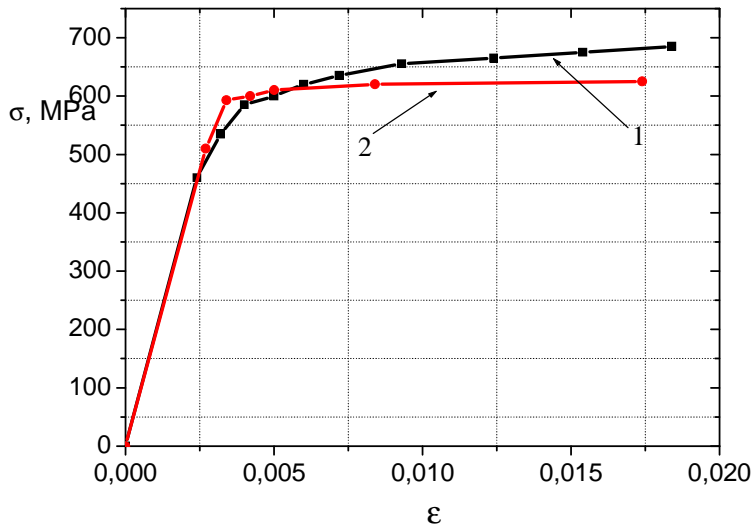


Fig.43. The stress-strain diagrams in the σ - ϵ stress –deformation coordinates of the permalloy foil 49 μm thick (1) and foil sample with a coating W-B 1.6 μm thick (2)

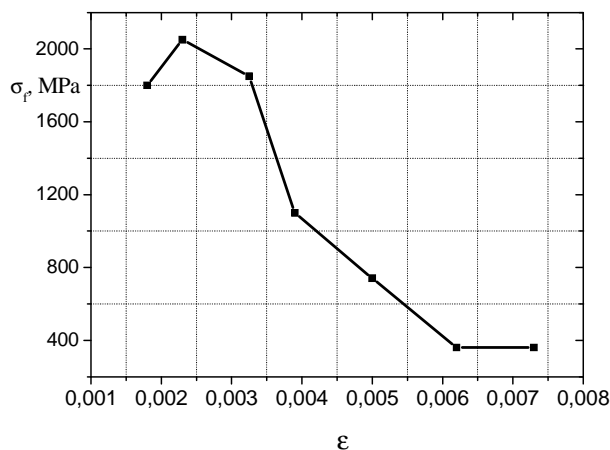


Fig. 44. Assumption tension diagram in the σ - ϵ stress –deformation coordinates for the system «permalloy foil - coating W-B» $t = 1.6 \mu\text{m}$ thick

The peculiar feature of the stress-strain diagrams of films-coatings is the stress buildup at the initial section, attainment of maximum with further maximum drop, which is indicative of disintegration. The evaluation of a film strength in terms of maximum σ_f shows that for W-B it is equal to 2000 MPa.

2.2.2.3 Defining the Systems W-Ti-B Coatings Strength While Studying the Samples Tension

The samples deformation test diagrams show three apparent stages: a- the foil and coating film elastic strain section; b- copper foil linear plastic strain hardening starting from the liquid limit and elastic film deformation; c- parabolic hardening section that corresponds to the plastic deformation of foil and film destruction. A characteristic point is a point of initiation of film destruction, which is shown on the diagram by abrupt decrease in strain hardening of sample [60]. The point position is used to determine the total deformation prior to a film destruction ϵ^* and foil with film composition hardening: $\Delta \sigma = \sigma_c - \sigma_{cop} \cdot C_{cop}$, as a difference between stress in

composition σ_c and yield load of a coating-free foil, which is multiplied by a volumetric portion according to the law of the additive composition hardening. The film strength is defined as $\sigma_f = \Delta\sigma/C_f$, where C_f is a volumetric portion of a film [61].

Fig.45 gives an example of a stress-strain diagram in the σ - ε stress –deformation coordinates of the copper foil sample with plastic base 39 μm thick (curve 1) and a foil sample with a coating 1 μm thick (curve 2). A critical point (K) that corresponds to the beginning of coating destruction is marked on a curve 2. In this case the difference values of deforming stresses shows that $\Delta\sigma$ is equal to 20 MPa. This hardening value can be created by a coating film-coating stress of $\Delta\sigma=600$ to 800 MPa. A coating tensile deformation by the beginning of its destruction is equal to $0,5...0,9 \cdot 10^{-2}$.

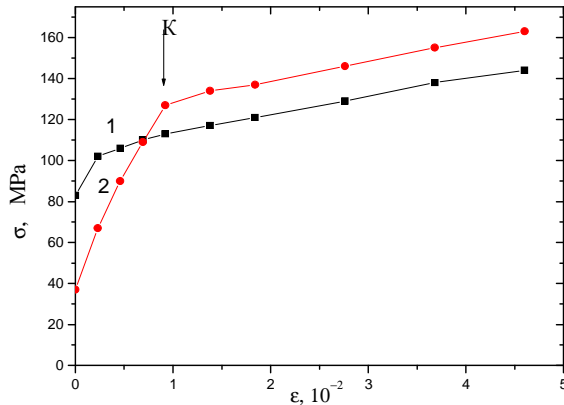


Fig. 45. The stress-strain diagrams in the σ - ε stress –deformation coordinates of the copper foil (1) and foil sample with a coating W-Ti-B (2)
 σ –stress, ε -deformation

2.2.3 Determination of the Modulus of Elasticity and Hardness Using the Method of Nanoindentation

2.2.3.1 Hardness and Modulus of Elasticity for W-B Coatings

The values of the modulus of elasticity and microhardness obtained using the method of nanoindentation are given in the Table 10.

Table 10. The results of nanoindentation for a nanodispersed W-B film 1,5 μm thick. The imprints were deposited at a distance of 15 μm from each other and four measurements were taken for each specimen.

Results	Modulus At Max Load (GPa)	Hardness At Max Load (GPa)	Disp at Max Load (nm)	Load At Max Load (mN)
1	404.979	34.007	98.726	5.046
2	375.930	32.094	99.290	4.822
3	401.273	34.752	97.619	4.973
4	398.525	31.752	99.170	4.891
Mean	395.177	33.151	98.701	4.933
Std. Dev.	13.101	1.457	0.761	0.097
% COV	3.32	4.40	0.77	1.97

The figures 46, 47 and 48 give the experimental dependences obtained at films nanoindentation.

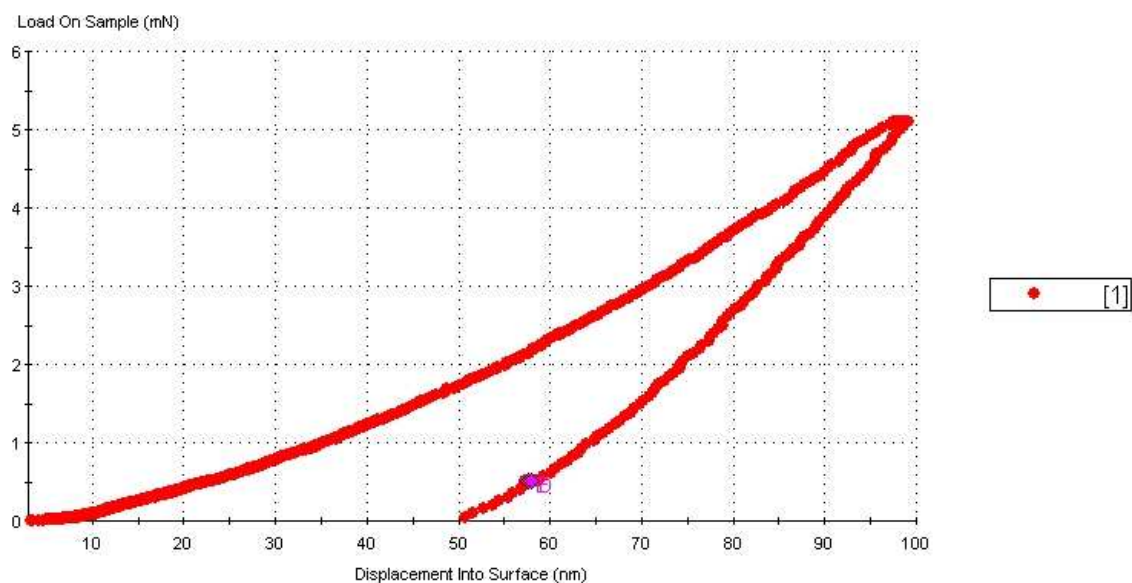


Fig.46. Diagram of loading for a nanodispersed W-B film obtained using the magnetron sputtering of a W_2B_5 target. A film thickness is $1.5 \mu m$

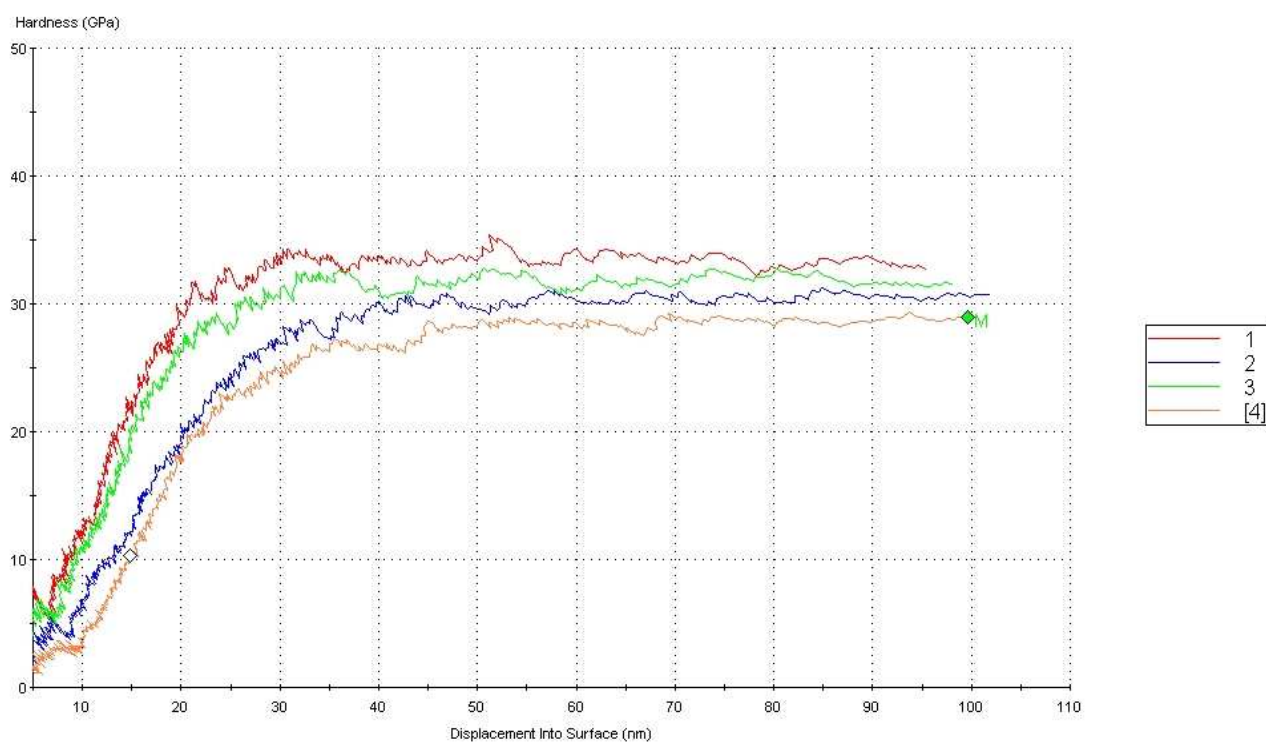


Fig. 47. Dependence of hardness for a nanodispersed W-B film on the depth of nanoindenter immersion

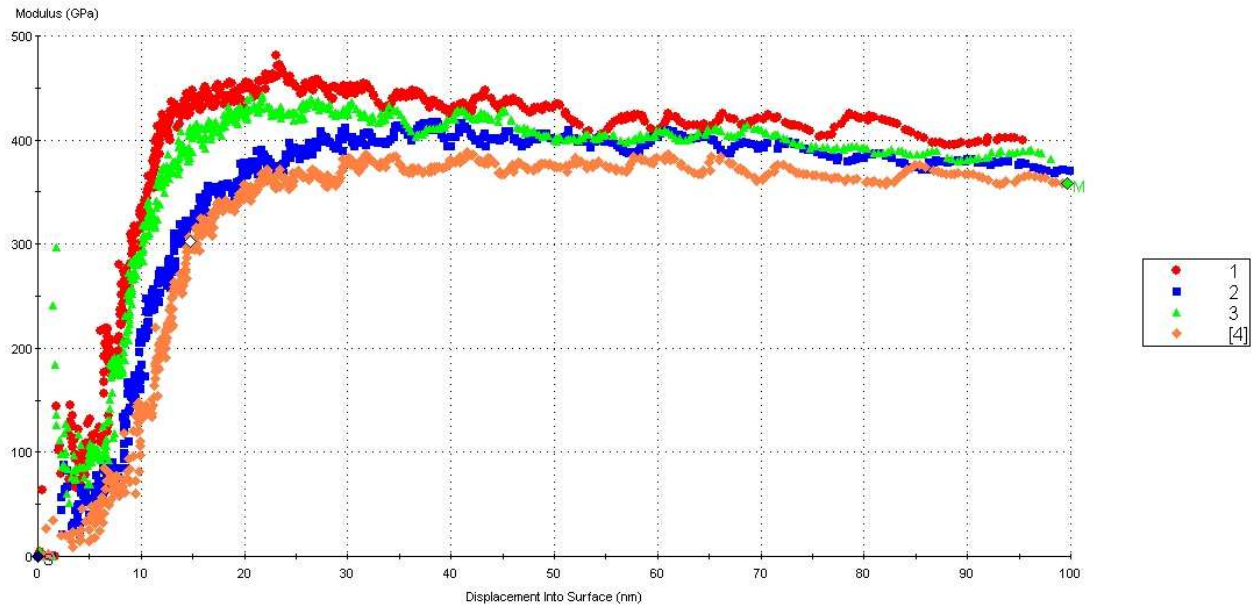


Fig. 48. Dependence of Young modules for a nanodispersed W-B film on the depth of nanoindenter immersion

2.2.3.2. Hardness and Modulus of Elasticity for Ti-B Coatings

The (100) Si plates were used to define modulus of elasticity and microhardness of Ti-B coatings using G200 nanoindenter. The values of the modulus of elasticity and microhardness obtained using the method of nanoindentation are given in the Table 11.

Table 11. The results of nanoindentation for a nanodispersed Ti-B film 1,0 μm thick. The imprints were deposited at a distance of 15 μm from each other and four measurements were taken for each specimen.

Results	Modulus At Max Load (GPa)	Hardness At Max Load (GPa)	Disp at Max Load (nm)	Load At Max Load (mN)
1	397.470	40.386	89.260	4.470
2	366.365	38.499	95.102	4.765
3	409.905	48.873	90.215	4.960
4	373.546	40.972	91.710	4.600
Mean	386.821	42.182	91.572	4.699
Std. Dev.	20.338	4.583	2.561	0.212
% COV	5.26	10.87	2.80	4.51

The figures 49, 50 and 51 give the experimental dependences obtained at films nanoindentation.

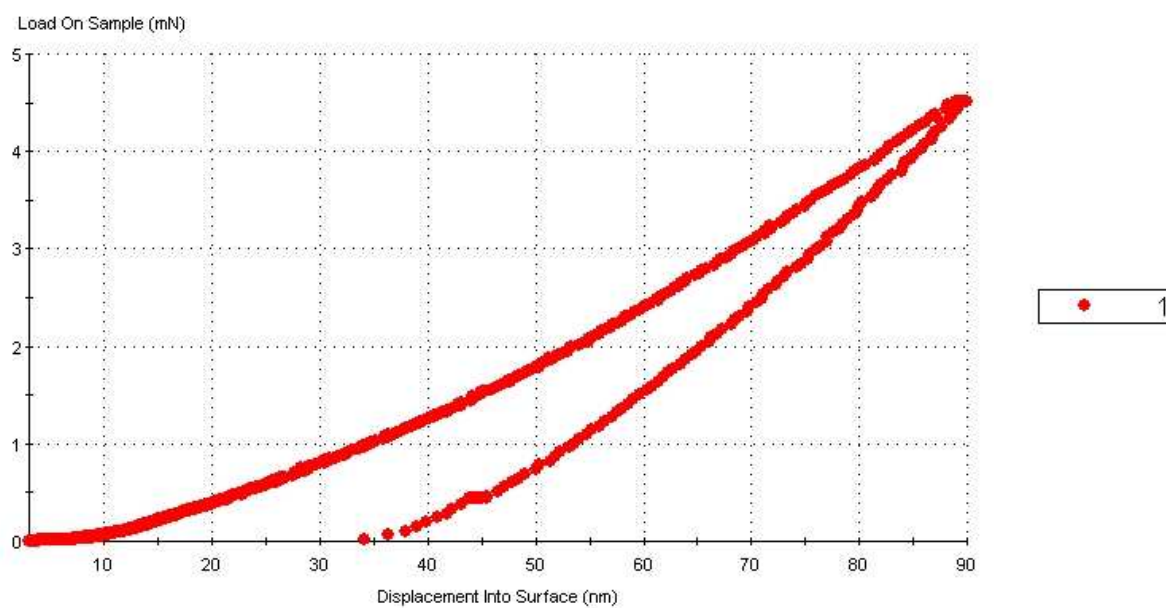


Fig.49. Diagram of loading for a nanodispersed Ti-B film obtained using the magnetron sputtering of a TiB_2 target. A film thickness is $1.0 \mu\text{m}$

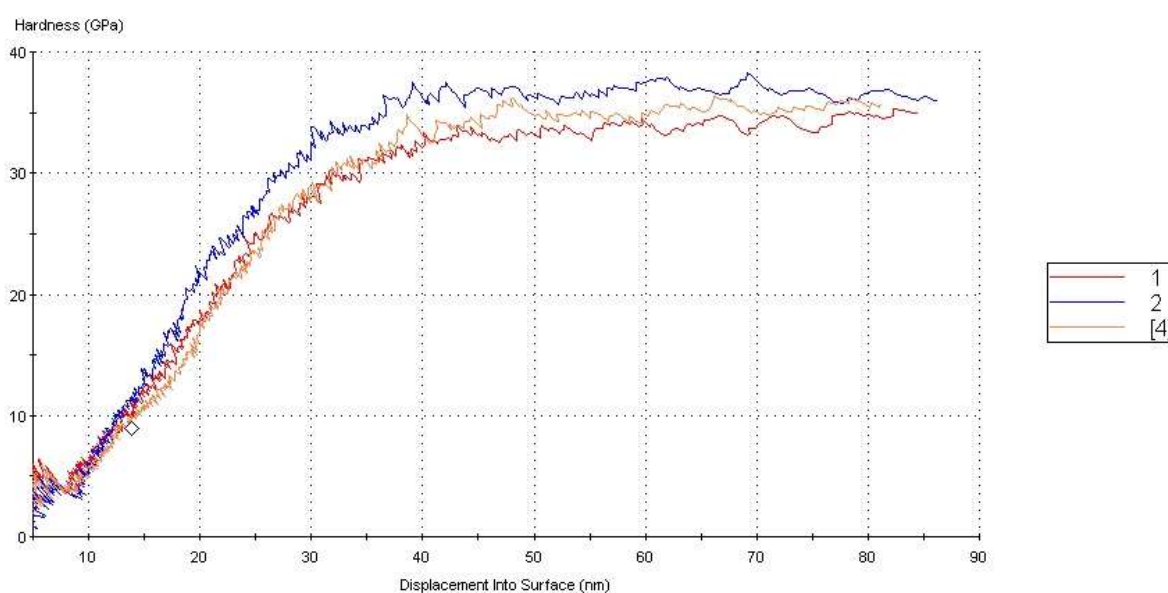


Fig.50. Dependence of hardness for a nanodispersed Ti-B film on the depth of nanoindenter immersion

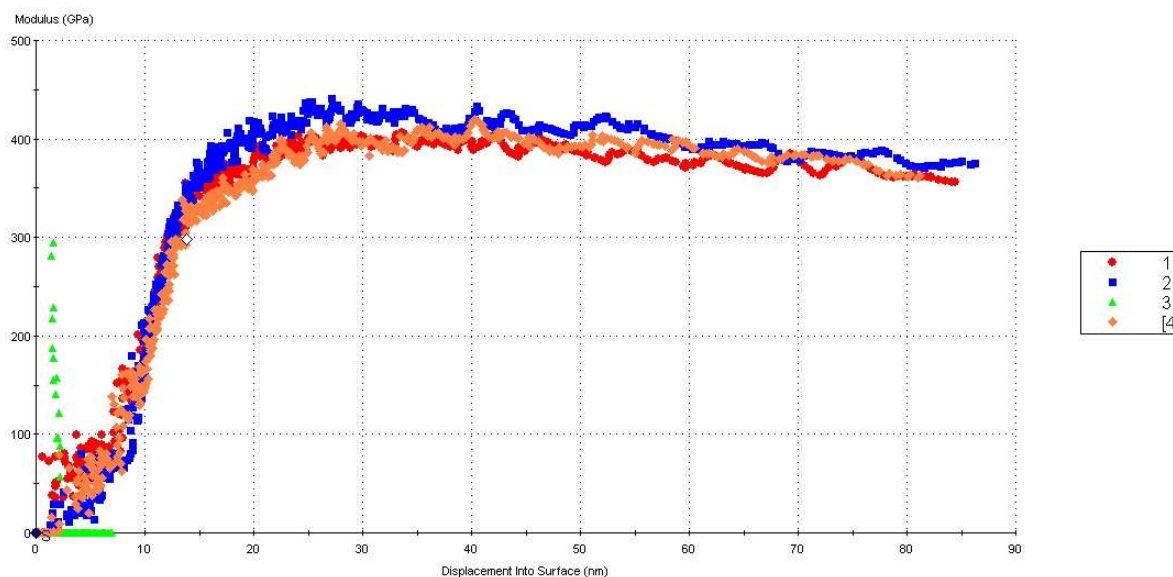


Fig.51. Dependence of Young modules for a nanodispersed Ti-B film on the depth of nanoindenter immersion

The Young module for a nanodispersed Ti-B film from the results of nanoindentation is equal to 386 GPa and microhardness is equal to 42 GPa.

A value of the modulus of elasticity determined by the deflection of cantilever turned out higher than a value determined by the method of nanoindentation both for Ti-B system (590 GPa and 386 GPa), accordingly, and for W-B system (790 GPa and 395 GPa), accordingly.

From our point of view this significant difference can be explained by behavior of a film material under indenter. It is quite possible that as indenter immerses in-depth the film the definite portion of a film material gets disintegrated under action of compressive stresses due to its high hardness and brittleness and ejects from the near-surface indenter-film contact region. As a result the contact area of a diamond pyramid and a film reduces facilitating its further penetration in-depth the film. The not monotonous character of Young modules and microhardness on the depth of nanoindenter immersion has been shown on obtained dependences. It confirms indirectly the assumption about destruction of film while nanoindenter immersion. The shape of the load profile is disturbed; it becomes flatter. It results in undervalued real mechanical characteristics of the test material.

2.2.3.3. Quasi-Binary $\text{TiB}_2\text{-WB}_2$ System

The methods of nanoindentation were used to obtain information on hardness and modulus of elasticity of a coating material and on the influence produced on them by the deposition modes. The coatings of 1 to 1.5 μm that were obtained by sputtering the TiB_2 , W_2B_5 50 mole% TiB_2 -50 mole% WB_2 targets with metal components' ratio of $\text{Ti/W}=0.09\ldots0.2$ have been studied. In the latter case in addition to the deposition on the substrates with an optimal temperature of 700°C the films were also deposited on the substrates with a lower temperature of 80 to 500°C for the purpose of variation of the crystallites' size. In all cases the coatings were deposited onto (100) Si plates.

The highest degree of nanohardness was reached for TiB_2 coatings and it was equal to 42,1 GPa and the lowest degree of nanohardness was peculiar for the coatings obtained by dispersion of a W_2B_5 target and it was equal to 33,1 GPa. The coatings obtained by dispersion of a 50 mole% TiB_2 -50 mole% WB_2 target had an average hardness value of 36,2 GPa. The modulus of elasticity for all those types of coatings varied in a rather narrow range of 386 to 395 GPa.

To study the influence produced by the crystallites' size on mechanical characteristics of coatings we used the samples of TiB_2 - WB_2 system of a variable composition (TiB_2 content was of 8 to 17 mole %) that were obtained at $T_s = 80 \dots 500^\circ\text{C}$.

The range of average crystallites' sizes of 2,7 to 19,3 nm that was established for these coatings allowed us to analyze the changes in the mechanical characteristics of coatings during transition from amorphous-&- cluster state to the nanocrystalline structural state of the condensates. It should be noted that the coatings that were used to study the mechanical characteristics were actually nontextured and their structural state fits the III concentration group of the structural classification given above.

The results of nanoindentation given in Table 12 show that with an increase in the crystallites' size the change in the elasticity modulus actually has a monotonous character. At the same time the relationship between the hardness and crystallites' size shows the marked flexure region with the maximum hardness value of $L \approx 9 \dots 12$ nm. The obtained maximum nanohardness value of 34,6 GPa somewhat exceeds nanohardness of the coatings obtained through sputtering of a pure W_2B_5 target.

A domain of the lowest L-values is marked by the highest H/E ratio that reaches the value of 0,12. When the crystallites 'size exceeds 12nm this ratio abruptly decreases (Table 12) and it tends to the value of 0,06, which is peculiar for the brittle bulk state.

Table 12. Nanohardness, modulus of elasticity and relationship H/E for TiB_2 – WB_2 coatings (content of TiB_2 8-17 mol.%, $T_s = 80 \dots 500^\circ\text{C}$) with average size of crystallites L

L, nm	2,7	2,9	4,1	9,0	12,3	15,1	19,3
H, GPa	22,5	22,8	26,9	34,6	34,2	32,9	31,9
E, GPa	179	184	213	289	301	324	333
H/E	0,12	0,12	0,12	0,12	0,11	0,10	0,09

2.2.4. Coatings Adhesion

A high adhesion can be judged by the values of mechanical stresses that arise in the substrate coatings. It was noted above that the rate of compressive stresses measured using the X-ray $\sin^2\psi$ method and the value of substrate flexure reached several GPa in the coatings. It means that the stress rate required for the separation of films from the substrates should be of the same order.

Other experiments also support a conclusion on high adhesion. The separation of a coating together with a substrate material was observed in many cases while depositing the (W-C, (W,Ti)-C) films onto silicon substrates at high temperatures ($T_s \geq 800^\circ\text{C}$). It means that the adhesion exceeds the silicon strength. According to the different data the strength value is in the range of 0.5 to 1GPa [62].

Under the action of high compressive stresses the W-Ti-B films of $\geq 1\mu\text{m}$ thick begin to separate from the silicon substrates. At the initial stages the hillocks with a diameter of $2R$ and a height of w_0 appear in a film. A substrate hillock can be considered as a film in a form of membrane fastened on an aperture with a diameter of $2R$, which is subjected to a hydrostatic pressure of P . The relationship between the pressure hillock geometry and its mechanic characteristics is given by a ratio [63]:

$$P = \left(\frac{\delta}{R} \right)^4 \cdot \frac{E \cdot w_0^3}{0.290 \cdot t^3} , \quad (19)$$

E – Young module, t -film thickness.

The formula (19) was derived for the Poisson ratio $\gamma=0.3$.

It is evident that the value P should be equal or should exceed the adhesion stress. The cupola height of w_0 was determined using the optical microscope, by focusing the cupola vertex and film on a flat substrate. At the values of $2R=10 \mu\text{m}$, $t=1 \mu\text{m}$, $w_0=1 \mu\text{m}$, $E=800 \text{ GPa}$ the P -value reaches several GPa.

2.2.5. Determining the Coefficient of Thermal Expansion of Boride Films

The experiments carried out to study the elastic stresses that arise in the films deposited on the substrates during condensation contain all the necessary data required to determine a linear expansion coefficient for the films.

Thus, on completing the deposition the film-coated substrate is subjected to cooling from 500 K down to 300 K and it experiences additional thermo-elastic stresses caused by the difference in coefficients of linear expansion. The information about deflection value of δ of a cantilever substrate at its cooling in the range of T_1 down to T_2 , modules of elasticity of substrate E_s and film E_f , geometry of substrates and films allows us to determine the difference $\Delta\alpha_{sf}$ in coefficients of linear expansion of a substrate α_s and film α_f from the point of view of the theory of elasticity [54].

$$\alpha_s - \alpha_f = \Delta\alpha_{sf} \quad (20)$$

$$\Delta\alpha_{sf} = \frac{2\delta}{l^2 \Delta T} \cdot \left[\frac{t}{2} + \frac{2(E_s I_s + E_f I_f)}{t} \cdot \left(\frac{1}{E_s t_s} + \frac{1}{E_f t_f} \right) \right] , \quad (21)$$

where I_s and I_f are the moments of inertia of a substrate and film, $\Delta T=T_1-T_2$.

The Ti-B film systems on a stainless steel substrate and mica (muscovite) substrate have been studied.

The modulus of elasticity for the substrate (mica -muscovite) and for the boride Ti-B films were determined experimentally by the substrate and film-coated substrate strains (see Fig.37). Figure 37 gives data for the Ti-B film-mica system. The values of the modulus of elasticity are equal to $E_{mica}=185 \text{ GPa}$, $E_f=590 \text{ GPa}$. The table values of the Young modulus from stainless steel ($E_s = 220 \text{ GPa}$) were used to calculation.

For the Ti-B film-stainless steel system the $\Delta\alpha_{sf}$ - value was determined from the experimental curve by deviation of the cantilever-fixed substrate. A substrate temperature varied in the range of 500°K to 300°K (see Fig.35). The difference in the linear expansion coefficients for the stainless steel and Ti-B film was equal to $\Delta\alpha_{sf}=7.9 \cdot 10^{-6} \text{ K}^{-1}$.

A linear expansion coefficient for the stainless X18H10T steel was determined experimentally using the X-ray method by a change of lattice spacing in the temperature range of 293 to 513°K. The lattice spacing for the stainless steel was 0.3590 nm at $T=293 \text{ K}$ and 0.3605 nm at $T=513 \text{ K}$. The temperature dependence of a lattice spacing was rather well-described by a straight line. The average linear expansion coefficient is equal to $19 \cdot 10^{-6} \text{ K}^{-1}$.

Thus, the studies of the stainless steel –Ti-B film system show that the linear expansion coefficient for Ti-B film is equal to $11 \cdot 10^{-6} \text{ K}^{-1}$.

Fig.36. gives the deviation of a console end for the mica (muscovite) - Ti-B film system at cooling in the range of 500°K down to the room temperature. Fig.36 shows that the cantilever end practically does not deviate during cooling, i.e. the difference in the linear expansion coefficients for the mica and Ti-B film is near zero. The calculation based on ratio (20, 21) gives the $\Delta\alpha_{sf}=1,1 \cdot 10^{-6} \text{ K}^{-1}$ value. Thus, the linear expansion coefficient of Ti-B films in the temperature range of 300 to 500 K is close to thermal expansion coefficient for mica (muscovite).

It is known that the linear expansion coefficient for mica (muscovite) depends on its composition. In this connection we carried out the individual X-ray experiments to study mica (muscovite) in the temperature range of 300 to 520 °K. A mica (muscovite) substrate packet served as an object of investigation and the packet ends were subjected to the X-ray exposure in the indicated temperature range. The diffraction lines (400), (060), (00.10), (312) were recorded in the Co- K_α radiation. The lattice period varied along the a-axis in the range of 0.5180 nm at 293 K to 0,5191 nm at 523 K and it varied along b-axis in the range of 0,9020 nm at 293 K to 0,9042 nm at 523 K. The dependence of a and b lattice periods on temperature was described by a squared relationship. The thermal expansion coefficients for mica were experimentally determined along the a - α_a axis and b - α_b axis. The α_a -values changed as follows: $6,7 \cdot 10^{-6} \text{ K}^{-1}$ at $T=300 \text{ K}$, $8,8 \cdot 10^{-6} \text{ K}^{-1}$ at $T=370 \text{ K}$ and $14,4 \cdot 10^{-6} \text{ K}^{-1}$ at $T=520 \text{ K}$. Thus, the linear expansion coefficient for mica (muscovite) in the basal plane is actually isotropic. In the range of experiment error the average value of a linear expansion coefficient for mica (muscovite) is equal to $9 \cdot 10^{-6} \text{ K}^{-1}$ and as it was noted above it corresponds to the value of linear expansion coefficient for Ti-B film.

It should be noted that the values of the linear expansion coefficients for Ti-B film that were measured in terms of deformation of the substrates made of stainless steel and mica coincide in the range of experiment error. The value of linear expansion coefficient for Ti-B film is equal to $\alpha_f=10 \pm 1 \cdot 10^{-6} \text{ K}^{-1}$.

In the temperature range of 300 to 500 K the value of linear expansion coefficient for the polycrystalline TiB_2 sample in a bulk state is equal to $7,0 \cdot 10^{-6} \text{ K}^{-1}$ [57, 64]. The obtained experimental values of the linear expansion coefficient of a film considerably exceed the value of TiB_2 along the a -axis but are very close to the linear expansion coefficients along the c -axis, which is equal to $9,5 \cdot 10^{-6} \text{ K}^{-1}$. We could assume that the studied Ti-B films are textured with the c -axis, which is parallel to a substrate plane. However, the diffraction high energy electrons for transparency survey from the thin Ti-B layers that were deposited at the given temperatures gives a halo-like pattern. Such a pattern is peculiar for the amorphous or nanodisperse state with the block size of $L \sim 1 \text{ nm}$. Therefore the obtained value of linear expansion coefficient refers to the Ti-B film in the amorphous state or ultimate nanodisperse state.

Conclusion

1. Targets and Coatings Production Conditions

1.1 Targets Production Conditions

The titanium boride TiB_2 powders and tungsten boride W_2B_5 powders were synthesized using the method of borothermal reduction of the oxides or titanium and tungsten oxycarbides. The tungsten carbide WC powders and titanium carbide TiC powders have been obtained. The targets with the diameter of 50 and 100 mm and 4 and 7 mm thick were prepared using the method of hot pressing at a temperature of 2000°C

The targets of quasibinary W_2B_5 - TiB_2 system with a volume content of W_2B_5 component 5, 10, 20, 50, 69, 80, 90 and diameter of 50 mm and TiC-WC system with percentage volume content of WC component 5, 10, 20, 50, 75, 80, 85 and 90 and diameter of 50 mm have been

fabricated. A target of 80 vol. % W_2B_5 + 20 vol% TiB_2 with diameter of 100mm was fabricated for the triode sputtering scheme.

The elemental and phase composition of the targets and their structural state were controlled using the X-ray methods. The single-phase TiB_2 , W_2B_5 and WC targets with the hexagonal crystal lattices and the TiC target with the cubic crystal lattice were synthesized by varying the reduction parameters and hot pressing parameters.

The synthesized targets were used for producing the coatings using the methods of ion-plasma sputtering according to the magnetron scheme and triode scheme.

1.2. Ion-Plasma Coatings Production Conditions

The vacuum ion-plasma condensates of metal-ceramic materials were obtained using the magnetron and triode schemes of ion sputtering.

In the case of magnetron method used for the production of the films and coatings the voltage of 350 to 420 V was applied to a target and the argon pressure (p_{Ar}) in the vacuum chamber during the target sputtering was equal to 0,1...0,2 Pa. At the magnetron power of $W = 42$ W (a voltage of 420 V and a current of 100 mA) and a target –to –substrate distance of 40 to 60 mm the deposition rate ω was equal to 0,05...0,10 nm/s.

In the case of triode scheme of sputtering (the arc mode was as follows: a voltage of 60 to 100 V and a current of 7 to 10 A) the voltage of 0.5 to 3.5 kV was applied to a target; it allowed for the generation of ion currents of 200 to 300 mA. A “target-substrate” distance was equal to 70...80 mm. A substrate temperature increased during deposition and did not exceed 500 to 600°C at the accelerating voltage of 3 kV. During the sputtering the argon pressure in the chamber was maintained at a level of 0.2 to 0.75 Pa.

Thus, the transition from magnetron scheme of sputtering to the triode scheme of sputtering allowed for the essential increase in the energy of dispersing particles and expanded the possibilities of the ion-plasma method.

During the deposition of coatings the substrates were the monocrystal silicon plates of 340 to 420 μm thick ($t_s = 340...420 \mu m$), aluminum foil of 15 μm thick ($t_s = 15 \mu m$), beryllium foil of 35 μm thick ($t_s = 35 \mu m$) as well as pyroceramics, tungsten, mica, stainless steel, tantalum and niobium.

The elemental and phase compositions of a target were controlled after deposition of the films. These corresponded to the original compositions.

2. Studying the Structure of the Ion-Plasma Films and Coatings

2.1 Thin Films

According to the data of the electron-optical studies the thin Ti-B and W-B films that were obtained using the method of magnetron sputtering of the W_2B_5 and TiB_2 targets have an amorphous-like structure with the volume-distributed nanodispersed inclusions (~5 nm).

According to the data of the electron-optical studies the titanium boride films of <100 nm thick that were obtained via the triode sputtering of TiB_2 target at a target potential of 1,5 kV were single-phase. The composition corresponded to that of TiB with the crystallites' size of ~10 nm. The thin films showed the light atoms depletion, which can be conditioned by the processes of the secondary ion sputtering of a growing film by Ar-atoms reflected from a target and dispersed by the heavy atoms.

A distinctive feature of the thin films of Ti-B system that were obtained using the triode method is the formation of nanocrystal structure straight in the initial layers of growth. In the case of W-B system the formation of the amorphous-like structural state occurs at the initial stages of growth.

2.2 Thick Films (Coatings)

2.2.1 Phase Composition

During sputtering of the pure TiB_2 and TiC targets the appropriate single-phase coatings are formed in the thick films of ~1 μm .

The formation of a single-phase solid (W, Ti) B_2 solution on the basis of TiB_2 lattice occurs in the ion-plasma condensates that were obtained using the method of magnetron

sputtering of TiB_2 - W_2B_5 targets consisting, according to the data of X-ray diffraction, of two phases (TiB_2 and W_2B_5) with the hexagonal crystal lattice.

By analogy, the formation of a single-phase solid (W, Ti)C solution on the basis of TiC cubic lattice occurs in the ion-plasma condensates while sputtering the TiC-WC targets that consist of the phases with the cubic (TiC) and hexagonal (WC) crystal lattices.

A phase composition of the coatings that were obtained using the ion –plasma methods of sputtering for the α -WC target is defined by the deposition parameters.

It has been established that the coatings with the phase composition corresponding to that of a sputtered target (hexagonal WC) can be obtained using the triode method with the dispersion potential of 1 to 1.5 kV, low deposition rates of 0.08 to 0.13 nm/s and a substrate temperature of 450 to 500°C.

At the magnetron sputtering and high deposition rates in the case of triode scheme of sputtering the formation of the metastable (high temperature) β -WC modification with the cubic crystal lattice occurs in the coatings.

The ion-plasma condensates of $\sim 1\mu\text{m}$ thick in their amorphous-crystal structural state were obtained while sputtering a W_2B_5 target. A phase composition of nanocrystallites formed during condensation corresponds to that of the tungsten boride, which is inferior in comparison with the phases of the sputtered material.

The annealing of the condensates (annealing temperature is 1100 to 1250°C) having the amorphous–crystal structure in their initial state that were obtained using the magnetron method results in the preferable formation of the γ - W_2B –phase crystallites with the boron atomic arrangement in the tetrahedral voids of a tetragonal lattice consisting of the tungsten atoms. Among the transient metals' borides such a structure accounts for the strongest Me-Me bond.

2.2.2 Structure and Substructure

With an increase in a substrate temperature the formation and perfection of a texture for all types of the ion-plasma condensates is observed. The borides with the hexagonal structure form a texture with a basal (00.1) plane parallel to the growth surface. The crystallites' (100) plane has a preferable orientation parallel to the growth plane in the tungsten carbides and quasibinary systems with the WC content more than 35%. In the TiC-based coatings the formation of a texture with the [111] axis perpendicular to the substrate plane occurs at a rather low deposition temperature of 300°C. The increase in a temperature above 700°C results in the texture formation [110].

Using the data of the “for reflection” and “for transparency” survey of the films on a beryllium substrate the anisotropy of crystal sizes was established. With an increase in a substrate temperature from 300 to 800°C the size of crystallites increases from 6nm to 17 nm in direction of film normal. The size of crystallites in a film plane slightly changes and it is within 5.7 to 6.7 nm.

2.2.3 Stressed State

During deposition the formation of elastic compressive strain occurs in the crystal lattice of a coating. Such a strain is determined using the X-ray “ $\sin^2\psi$ ” –method. The highest strain values (up to 2%, which correspond to the action of stresses of 6 to 7 GPa) were revealed in the coatings deposited on substrates at the relatively low (80...300°) temperatures. With an increase in a substrate temperature the value of lattice strain during growth decreases.

The stresses determined using a flexure value of the cantilever substrates (mica, permalloy, stainless steel) during deposition also show the presence of compressive strains of 2 to 4 GPa.

The presence of high compressive stresses in the condensates resulted in many cases in the separation of coatings from the substrates and in the generation of “hillock” formations that have the features peculiar for a fractal structure. A fractal dimension D_f of these formations that was determined using the method of surface secants made up 1.23 to 1.25 for the ion-plasma condensates.

3. Physical and Mechanical Characteristics

The modulus of elasticity of the coatings was determined by nanoindentation (substrate normal) and by flexure of cantilever substrate with a coating (parallel to the substrate).

The value of the modulus of elasticity, which was determined from a cantilever flexure, appeared to be higher in comparison with that of nanoindentation data (it is equal to 590 GPa and 386 GPa for the Ti-B system, accordingly and it is equal to 790 GPa and 395 GPa for the W-B system, accordingly).

The comparative studies of the mechanical properties of the “substrate” and “substrate – Ti-W-B condensate” system at uniaxial tension have been carried out. A tensile strain that leads to the initiation of a coating collapse reaches 0.9%. A maximum stress value at tension reaches 1.5 GPa for the WC system.

The research done using the method of nanoindentation showed that all types of the obtained coatings that were used in our work refer to the very hard coatings whose hardness exceeds 30 GPa. The maximum nanohardness of 42 GPa was reached for a TiB₂-phase based coating. The nanohardness-to-modulus of elasticity ratio reached 0.12.

The value of coating adhesion reached several GPa. Such an adhesion level is proven by a value of compressive stresses that arise in the coatings, which was measured using the X-ray “sin²ψ” method and in addition it was determined from a substrate flexure, separation of coatings with the substrate material, as well as using the model calculations. These calculations were done to determine a value of hydrostatic pressure, which was applied to a coating on a circular aperture to generate a hillock with a real geometry and prescribed physical-&-mechanical characteristics.

A difference in the coefficients of thermal expansion $\Delta =$ has been determined for a substrate and a film using the value of thermoelastic strains arising in the substrate- Ti-B film system after termination of condensation and cooling from 500 K to 300 K. For the mica and stainless steel substrates the Δ value is equal to 1,1 and 7.9, accordingly. The coefficients of thermal expansion for the stainless steel and the main coefficients of the tensor of thermal expansion for the mica (along a, b and c axis) α_b , α_a , α_c were determined using the X-ray method. These data were used to determine the coefficient of thermal expansion for Ti-B coating $\alpha_f = 10 \cdot 10^{-6} \text{ K}^{-1}$. This value exceeds the α -value of the polycrystalline TiB₂ by 30% and it is close to α_c -value of TiB₂-monocrystal. These boride coatings have an amorphous or ultimately nanodispersed structure.

4. Influence of Radiation Simulating the Near-Earth Space Factors

It has been established that the irradiation that simulates the open space factors in the course of year does not lead to the noticeable changes in the elemental and phase compositions, structure and coatings' substructure. A decrease in the value of compressive stresses has been revealed. For example, the relative decrease in deformation makes up 25% for the 90mole%TiC-10mole% WC composition at irradiation dose that corresponds to the open space exposure in the geostationary orbit (at a height of 36000 km) in the course of year. A maximum relative change in the initial elastic compressive strain is observed in the coatings highly enriched with a WC component ($\Delta\epsilon/\epsilon \sim 50\%$), in which the initial level of compressive strain was lower.

Thus, the open space factors contribute to the partial relaxation of compressive strains in a coating and to the transition of a material to a more equilibrium state.

References

1. Mayrhofer P.H., Mitterer C., Wen J.G., Greene J.E., Petrov I. Self-organized nanocolumnar structure in superhard TiB₂ thin films // Appl. Phys. Lett.-2005.- V. 86(12).- 131909-3.
2. Lee S.H., Nam K.H., Hong S.C., Lee J.J. Low temperature deposition of TiB₂ by inductively coupled plasma assisted CVD // Surface and Coatings Technology.- 2007.- V.201.- P. 5211-5215.

3. M.Mikula, B.Grancic, V.Bursikova, A.Csuba, M. Drzik, S. Kavecky, A.Plecenik, P.Kus. Mechanical properties of superhard TiB₂ coatings prepared by DC magnetron sputtering // Vacuum.-2007.- V.82.-N.2 SPEC.ISS.-P.278-281.
4. Wang Zhen-ting, Zhou Xiao-hui, Zhao Guo-gang. Microstructure and formation mechanism of in-situ TiC-TiB₂/Fe composite coating // Trans. Nonferrous Met. Soc. China.-2008.-V.18.-P.831-835.
5. Veprek S., Veprek-Heijman M.G.J., Karvankova P., Prochazka J. // Thin Solid Films.-2005.-V. 476.-P. 1-29.
6. Kiryukhantsev-Korneev Ph.V., Stansky D.V., Petrznik M.I., Levashov E.A., Mavrin B.N. // Surf. Coat. Tech. -2007.-V.201.-P. 6143-6147.
7. Kauffmann F., Dehm G., Schier V., Schattke A., Beck T., Lang S., Arzt E. // Thin Solid Films.-2005.-V. 473.-P. 114-122.
8. Zhang S., Sun D., Fu Y., Du H // Surf. Coat. Tech. 198 (2005).
9. А. Р. Андриевский, И. И. Спивак Прочность тугоплавких соединений и материалов на их основе – Челябинск : Металлургия. Челябинское отделение, 1989. – 368 с.
10. Г. В. Самсонов, Г. Ш. Упадхя, В. С. Нешпор. Физическое материаловедение карбидов – Киев : Наукова думка, 1974. – 456 с.
11. А. В. Гусев, А. А. Ремпель. Структурные фазовые переходы в нестехиометрических соединениях – М. : Наука, 1988. – 308 с.
12. Н. Romanus, V. Cimalla, J. A. Schaefer Preparation of single phase tungsten carbide by annealing of sputtered tungsten-carbon layers // Thin Solid Films. – 2000. – Vol. 359. – P. 146–149.
13. Г. В. Самсонов, Т. И. Серебрякова, В. А. Неронов. Бориды – М. : Атомиздат, 1975. – 376 с.
14. C. Schmalzried, R. Telle, B. Freitag. Solid State Reaction in Transition Metal Diboride-Based Materials // Z. Metallkd. 2001. – Vol. 92, № 11. – P. 1197–1202.
15. Л. И. Гладких, О. Н. Григорьев, О. В. Соболев, А.Т. Пугачев, Е.А. Соболев, С.А. Мартынюк. Структура и прочность композиционной керамики TiB₂-CrB₂ и TiB₂-W₂B₅, полученной методом горячего прессования // ВАНТ. Серия Физика радиационных повреждений и радиационное материаловедение. – 2002. – № 6. – С. 139–142.
16. M. Tajika, H. Mastubara, W. Rafaniello. Development of synergistic AlN ceramics by simultaneous addition of BN and TiN // J. Mater. Sci. Lett. – 2001. – Vol. 20. – P. 201–203.
17. K. S. Mazdiyasn, R. Ruh, E. E. Hermes. Phase characterization and properties of AlN-BN composites // Am. Ceram. Soc. Bull. – 1985. – Vol. 64. – P. 1149–1154.
18. J.-F. Li, R. Watanabe. Pressureless sintering and high-temperature strength of SiC-AlN ceramics // J. Ceram. Soc. Jpn. – 1994. – Vol. 102. – P. 727–731.
19. J.-L. Huang, J.-M. Jih. Investigation of SiC-AlN: Part II, Mechanical properties // J. Am. Ceram. Soc. – 1996. – Vol. 79. – P. 1262–1264.
20. R.-R. Lee, W.-C. Wei. Fabrication, microstructure and properties of SiC-AlN ceramic alloys // Ceram. Eng. Sci. Proc. – 1990. – № 11. – P. 1094–1121.
21. I.-L. Tangen, Y. D. Yu, T. Grande. Preparation and characterisation of aluminium nitride-silicon carbide composites // J. Europ. Cer. Soc. – 2004. – Vol. 24. – P. 2169–2179.
22. Yu. P. Udalov, E. E. Valova, S. S. Ordanian. Fabrication and abrasive properties of eutectic compositions in system B₄C-SiC-TiB₂// Ogneupory. – 1995. – № 10. – P. 12–19.
23. І. Ф. Михайлов, О. М. Григор'єв, Ю. Г. Гогоці, А.Т. Пугачов, О.В. Соболев, З.І. Колупаєва Розробка фізичних основ створення керамічних композитів із високою контактною міцністю // Фундаментальні орієнтири науки (ФОН): Хімія та наукові основи перспективних технологій. – Київ : Академперіодика, 2005. – С. 327–343.
24. Русаков А.А. Рентгенография металлов. –М.: Атомиздат, 1977.- 479 с.
25. Warren B.E. X-Ray Diffraction.- Dover Publications, INC, New York, 1990.

26. Vink T.J., Walrave W., Daams J.L.C., Dirks A.G. Stress, strain and microstructure in thin tungsten films deposited by dc magnetron sputtering // J. Appl. Phys. 1993. – Vol. 74, №2. – P. 988-995.
27. Лисойван В.И., Громилов С.А. Аспекты точности в дифрактометрии поликристаллов - Новосибирск: Наука. Сибирское отделение, 1989. - 243 с.
28. Васильев В.Н., Гуров И.П. Компьютерная обработка сигналов в приложении к интерферометрическим системам -СПб.: БХВ - Санкт-Петербург, 1998. -240 с.
29. Мэтьюз Джон Г., Финк Куртис Д. Численные методы. Использование MATLAB, 3-е издание.: Пер. с англ. –М.: Издательский дом “Вильямс”, 2001. –720 с.
30. Torrence C., Compo G. P. A Practical Guide to Wavelet Analysis // “Bulletin of the American Meteorological Society”, Vol. 79, №.1, 1998. -P.61-78, Дьяконов В.П. Вейвлеты. От теории к практике. – М.: СОЛОН-Р, - 2002. -448 с.
31. Реклейтис Г., Рейвиндран А., Регсдел К. Оптимизация в технике т.1–М: Мир, 1986. - 349 с.
32. Банди Б. Методы оптимизации: Вводный курс. М.: Радио и связь, 1988. – 64 с.
33. Бейко И.В., Бублик Б.Н., Зинько П.Н. Методы и алгоритмы решения задач оптимизации. Киев: Вища школа, 1983.- 512 с.
34. Powder Diffraction File of the International Centre for Diffraction Data, PDF , Philadelphia, 1996.
35. Bull S.J. Interface engineering and graded films: Structure and characterization J. Vac. Sci. Technol. A.- 2001.-V. 19(4).- P.1404-1414.
36. Абраимов В.В., Негода А.А., Завалишин А.П., Колыбаев Л.К. Комплексная имитация факторов космического пространства// Космічна наука і технологія. – 1995.– 1, №2-6.– С. 76–80.
37. Powder Diffraction File of the International Centre for Diffraction Data, PDF № 35-0741.
38. Powder Diffraction File of the International Centre for Diffraction Data, PDF №12-0337.
39. А.Ф. Скрышевский. Структурный анализ жидкостей и аморфных тел. – М.: Высшая школа, 1980. – 250 с.
40. Н.А. Ватолин, Э.А. Пастухов. Дифракционные исследования строения высокотемпературных расплавов. М.: Наука, 1980, 188 с.
41. JCPDS Powder Diffraction Cards, International Center for Diffraction Data, Swarthmore, PA, 1996, Card 06-0541, Card 25-0990, Card 35-0738.
42. Телле Р., Е. Фендлер, Г. Петцов. Квазитройная система $TiB_2-W_2B_5-CrB_2$ и её возможности в эволюции керамических твердых материалов // Порошковая металлургия. – 1993. – № 3. – С. 58–69.
43. Y. G. Wu, E. H. Cao, Z. S. Wang et al. Stress anisotropy in circular planar magnetron sputter deposited molybdenum films and its annealing effect // Appl. Phys. – 2003. – A 76. – P. 147–152.
44. Нанотехнологии в электронике / под ред. Ю. А. Чаплыгина. – М. : Техносфера, 2005. – 448 с.
45. Иванова В. С., Баланкин А. С., Бунин И. Ж., Оксагоев А. А. Синергетика и фракталы в материаловедении. –М.: Наука, 1994.– 383 с.
46. Krzanowski J. E., J. L. Endrino The effects of substrate bias on phase stability and properties of sputter-deposited tungsten carbide // Materials Letters. – 2004. – Vol. 58. – P. 3437–3440.
47. JCPDS Powder Diffraction Cards. International Center for Diffraction Data, Swarthmore, PA, 1998, β -WC_{1-x} : Card 20-1316, α -WC: Card 25-1047, α -W₂C: Card 35-776
48. Горбачева Т. Б. Рентгенография твердых сплавов / Т. Б. Горбачева. – М. : Металлургия, 1986. – 103 с.
49. Li-Ying Kuo and Pouyan Shen On the condensation and preferred orientation of TiC nanocrystals — effects of electric field, substrate temperature and second phase//Materials Science and Engineering A.- 2000.- Vol. 276, Issues 1-2, P. 99-107.

50. Модель космического пространства. Т.1 / Под ред. акад. С. Вернова. – М.: изд-во МГУ, НИИ ядерной физики, 1983. – 336 с.
51. Загребельный А.А., Незнамова Л.О., Никитский В.П. и др. Развитие техники нанесения тонкопленочных покрытий в космосе. Космос: технологии, материаловедение, конструкции: Сб. науч. тр. / Под. Ред. Б.Е. Патона.- Киев: ИЭС им. Е.О.Патона НАН Украины, 2000. – С. 298-301.
52. Бержатый В.И., Зворыкин Л.Л. и др. Перспективы реализации вакуумных технологий в условиях орбитального полёта. // Автоматическая сварка, 1993 - №10. – С. 108-116.
53. Handbook of Thin Film Technology edited by Leon I. Maissel and Reinhard Glang.- McGraw Hill Book Company, 1970.
54. С.П. Тимошенко. Устойчивость стержней, пластин и оболочек.- М.: Наука, 1971.
55. Ф. Кашпар. Термобиметаллы в электротехнике. -М.-Л.-Государственное энергетическое издательство, 1961, 448 с.
56. M. Berger, L. Karisson, M. Larsson and S. Hogmark. Low stress TiB_2 coatings with improved tribological properties // Thin Solid Films.- 2001.- V. 401.- P. 179-186.
57. R.G. Munro. Material Properties of Titanium Diboride // Journal of Research of the National Institute of Standards and Technology.-2000.- V.105.- P. 709-720.
58. Дж. Гилман – В кн.: Атомный механизм разрушения. Пер. с англ. М., Metallurgizdat, 1963, с. 220-253.
59. Крейдер К. Г. Введение в композиционные материалы с металлической матрицей /Под ред. Крейдер К..// В кн. Композиционные материалы с металлической матрицей.-М.: Машиностроение, 1978 с. 9-47.
60. Тимошенко С.П., Гудьер Дж Теория упругости. М.: Наука, 1979 -560 с.
61. Нотт Дж.Ф. Основы механики разрушения. М.: Metallurgia, 1978 -256 с.
62. Концевой Ю.А. и др. Пластичность и прочность полупроводниковых материалов и структур.-М: Радио и связь, 1982.
63. Прочность, устойчивость, колебания: Справочник. Том 1/Под редакцией И.А. Биргера, Я.Г. Пановко.- М.: Машиностроение, 1968.- 832 с.
64. Т.И.Серебрякова, В.А.Неронов, П.Д.Пешев. Высокотемпературные бориды.-1991.- М.: Metallurgia, Челябинское отделение, 368 с.

List of Symbols, Abbreviations, and Acronyms

T_s –substrate temperature

P - argon pressure in a vacuum chamber

U_s –potential in a condition sputtering

t_s, t_f – substrate thickness, film thickness

a, b, c - perodes of lattice

$\Delta\Psi$ - a degree of texture perfection

l - substrate length,

b - substrate width

δ - deflection of cantilever

σ -stress, ε - deformation

H- hardness

E_s, E_f - Young modules for a substrate and film, accordingly

E_0 - effective modulus of elasticity of a film-coated substrate

F - load

D_f - fractal dimensionality

α_s, α_f - thermal expansion coefficient of substrate and film, accordingly

I_s, I_f - moments of inertia of a substrate and film, accordingly